SEARCH FOR THE HIGGS BOSON IN THE $ZH \to \ell^+\ell^- b\bar{b}$ CHANNEL AT CDF RUN II

DISSERTATION

Presented in Partial Fulfillment of the Requirements for

the Degree Doctor of Philosophy in the

Graduate School of The Ohio State University

By

Jonathan Zvi Efron, B.S., M.S.

* * * * *

The Ohio State University

2007

Dissertation Committee:

Prof. Brian L. Winer, Adviser

Prof. Eric Braaten

Prof. Richard E. Hughes

Prof. Lou DiMauro

Approved by

Adviser

Graduate Program in Physics

ABSTRACT

The Standard Model of particle physics is in excellent agreement with the observed phenomena of particle physics. Within the Standard Model, the weak and electromagnetic forces are successfully combined. However, this combination is only valid if the masses of the force carriers of the weak force, the Z and W bosons, are massless. In fact, these two particles are the second and third most massive observed elementary particles. Within the minimal Standard Model, the Higgs mechanism is introduced to reconcile this contradiction. Conclusive proof of this theory would come with the discovery of the Higgs boson.

This dissertation presents a search for the Higgs boson produced in conjunction with a Z boson. This search is limited to a Higgs boson mass range between 100 GeV/c^2 and 150 GeV/c^2, for Higgs boson decays to a $b\bar{b}$ pair, and Z boson decays to $\ell^+\ell^-$, an oppositely-charged lepton pair. The data sample size is 1.0 fb^{-1} collected from the CDF detector using collisions from Fermi National Accelerator Laboratory's Tevatron. Two artificial neural networks improved the sensitivity of the search. One network improved the jet energy resolution from the b and $\bar{b}$ quarks. A second network distinguished the ZH signal from its major backgrounds. Fitting the data output of the latter neural network failed to show evidence for the Higgs boson. The search limited, at 95% confidence level, the $\sigma(ZH) \cdot BR(H \rightarrow b\bar{b})$ to 1.7 pb (1.1 pb) for a Higgs boson mass 100 GeV/c^2 (150 GeV/c^2). This limit is 13 (150) times larger than

the $\sigma(ZH) \cdot BR(H \rightarrow b\bar{b})$ derived from the Standard Model, for a Higgs boson mass of 100 GeV/c^2 (150 GeV/c^2).

To Ayala for better health

ACKNOWLEDGMENTS

I would like to thank Brian Winer for being patient enough to deal with every time I called him Richard, every nonsensical sentence that he corrected, and every presentation that I completed at 4 o'clock in the morning. I have gained from him incredible wisdom and knowledge both inside and outside physics.

Richard Hughes was a tremendous help during graduate school. He was always willing to help push this analysis forward and provide critical advice.

This analysis would not be possible without the tremendous hours of work put in by Benjamin Kilminster. We complimented each other well when constructing this analysis. I hope to be able to recreate such a close collaboration in the future. I would also like to thank Beate Heinemann, Andrew Mehta, and Brandon Parks for bringing thoughts, ideas, experience and innovation to the ZH search effort.

I apologize to Kevin Lannon for sitting in his office for the last three years. I partly stayed there out of inertia. Mostly though, I stayed there because I knew it was a great way to learn from him on an hourly basis.

And finally, I would like to thank my parents for raising me so I could venture out on my own.

VITA

April 2001	B.S. in Physics, University of Michigan, Ann Arbor, MI
September 2002 – August 2005	Fowler Fellowship The Ohio State University, Department of Physics, Columbus, OH
May 2005	M.S. in Physics The Ohio State University, Columbus, OH
August 2005 – August 2007	Graduate Research Associate The Ohio State University, Columbus, OH

PUBLICATIONS

"Measurement of the W^+W^- production cross section in $p\bar{p}$ collisions at $\sqrt{s} = 1.96$ TeV using dilepton events" D. Acosta *et al.* [CDF Collaboration] Phys. Rev. Lett. **94**, 211801 (2005)

"First evidence for $B_s^0 \to \phi\phi$ decay and measurements of branching ratio and A_{CP} for $B^+ \to \phi K^+$" D. Acosta *et al.* [CDF Collaboration] Phys. Rev. Lett. **95**, 031801 (2005)

"Search for long-lived doubly-charged Higgs bosons in $p\bar{p}$ collisions at $\sqrt{s} =$ 1.96 TeV" D. Acosta *et al.* [CDF Collaboration] Phys. Rev. Lett. **95**, 071801 (2005)

"Measurement of the cross section for $t\bar{t}$ production in $p\bar{p}$ collisions using the kinematics of lepton + jets events" D. Acosta *et al.* [CDF Collaboration] Phys. Rev. D **72**, 052003 (2005)

"Evidence for the exclusive decay $B_c^{\pm} \to J/\psi\pi^{\pm}$ and measurement of the mass of the B_c meson" A. Abulencia *et al.* [CDF Collaboration] Phys. Rev. Lett. **96**, 082002 (2006)

"Measurement of $B(t \to Wb)/B(t \to Wq)$ at the Collider Detector at Fermilab" D. Acosta *et al.* [CDF Collaboration] Phys. Rev. Lett. **95**, 102002 (2005)

"Measurement of the $t\bar{t}$ production cross section in $p\bar{p}$ collisions at $\sqrt{s} = 1.96$ TeV using lepton plus jets events with semileptonic B decays to muons" D. Acosta *et al.* [CDF Collaboration] Phys. Rev. D **72**, 032002 (2005)

"Search for first-generation scalar leptoquarks in $p\bar{p}$ collisions at $\sqrt{s} = 1.96$ TeV" D. Acosta *et al.* [CDF Collaboration] Phys. Rev. D **72**, 051107 (2005)

"Search for $\Lambda_b \to p\pi$ and $\Lambda_b \to pK$ decays in $p\bar{p}$ collisions at $\sqrt{s} = 1.96$ TeV" D. Acosta *et al.* [CDF Collaboration] Phys. Rev. D **72**, 051104 (2005)

"Search for new high mass particles decaying to lepton pairs in $p\bar{p}$ collisions at $\sqrt{s} = 1.96$ TeV" A. Abulencia *et al.* [CDF Collaboration] Phys. Rev. Lett. **95**, 252001 (2005)

"Measurement of the ratios of branching fractions $B(B_s^0 \to D_s^- \pi^+)/B(B^0 \to D^- \pi^+)$ and $B(B^+ \to \overline{D}^0 \pi^+)/B(B^0 \to D^- \pi^+)$" A. Abulencia *et al.* [CDF Collaboration] Phys. Rev. Lett. **96**, 191801 (2006)

"Measurement of b hadron masses in exclusive J/ψ decays with the CDF detector" D. Acosta *et al.* [CDF Collaboration] Phys. Rev. Lett. **96**, 202001 (2006)

"Search for $B_s \to \mu^+\mu^-$ and $B_d \to \mu^+\mu^-$ decays in $p\bar{p}$ collisions with CDF II" A. Abulencia *et al.* [CDF Collaboration] Phys. Rev. Lett. **95**, 221805 (2005) [Erratum-ibid. **95**, 249905 (2005)]

"Search for neutral MSSM Higgs bosons decaying to tau pairs in $p\bar{p}$ collisions at $\sqrt{s} = 1.96$ TeV" A. Abulencia *et al.* [CDF Collaboration] Phys. Rev. Lett. **96**, 011802 (2006)

"Direct search for Dirac magnetic monopoles in $p\bar{p}$ collisions at $\sqrt{s} = 1.96$ TeV" A. Abulencia *et al.* [CDF Collaboration] Phys. Rev. Lett. **96**, 201801 (2006)

"Top quark mass measurement using the template method in the lepton + jets channel at CDF II" A. Abulencia *et al.* [CDF Collaboration] Phys. Rev. D **73**, 032003 (2006)

"Precision top quark mass measurement in the lepton + jets topology in p anti-p collisions at $\sqrt{s} = 1.96$-TeV" A. Abulencia *et al.* [CDF Collaboration] Phys. Rev. Lett. **96**, 022004 (2006)

"A search for $t \to tau\nu q$ in $t\bar{t}$ production" A. Abulencia *et al.* [CDF Collaboration] Phys. Lett. B **639**, 172 (2006)

"Search for charged Higgs bosons from top quark decays in $p\bar{p}$ collisions at $\sqrt{s} = 1.96$-TeV" A. Abulencia *et al.* [CDF Collaboration] Phys. Rev. Lett. **96**, 042003 (2006)

"Measurement of the helicity of W bosons in top-quark decays" A. Abulencia *et al.* [CDF-Run II Collaboration] Phys. Rev. D **73**, 111103 (2006)

"Measurement of the top quark mass with the dynamical likelihood method using lepton plus jets events with b-tags in $p\bar{p}$ collisions at $\sqrt{s} = 1.96$-TeV" A. Abulencia *et al.* [CDF Collaboration] Phys. Rev. D **73**, 092002 (2006)

"Measurement of the inclusive jet cross section in $p\bar{p}$ interactions at $\sqrt{s}$ = 1.96-TeV using a cone-based jet algorithm" A. Abulencia *et al.* [CDF Run II Collaboration] Phys. Rev. D **74**, 071103 (2006)

"Search for second-generation scalar leptoquarks in $p\bar{p}$ collisions at $\sqrt{s}$ = 1.96-TeV" A. Abulencia *et al.* [CDF Collaboration] Phys. Rev. D **73**, 051102 (2006)

"Search for H to b anti-b produced in association with W bosons in $p\bar{p}$ collisions at $\sqrt{s}$ = 1.96-TeV" A. Abulencia *et al.* [CDF Collaboration] Phys. Rev. Lett. **96**, 081803 (2006)

"Measurement of the inclusive jet cross section using the k(t) algorithm in p anti-p collisions at $\sqrt{s}$ = 1.96-TeV" A. Abulencia *et al.* [CDF II Collaboration] Phys. Rev. Lett. **96**, 122001 (2006)

"Search for anomalous semileptonic decay of heavy flavor hadrons produced in association with a W boson at CDF II" A. Abulencia *et al.* [CDF Collaboration] Phys. Rev. D **73**, 051101 (2006)

"Measurement of mass and width of the excited charmed meson states D10 and D2*0" A. Abulencia *et al.* [CDF Collaboration] Phys. Rev. D **73**, 051104 (2006)

"Top quark mass measurement from dilepton events at CDF II" A. Abulencia *et al.* [CDF Collaboration] Phys. Rev. Lett. **96**, 152002 (2006)

"A search for scalar bottom quarks from gluino decays in $\bar{p}p$ collisions at $\sqrt{s}$ = 1.96-TeV" A. Abulencia *et al.* [CDF Collaboration] Phys. Rev. Lett. **96**, 171802 (2006)

"Measurement of the dipion mass spectrum in $X(3872) \to J/\psi\pi^+\pi^-$ decays" A. Abulencia *et al.* [CDF Collaboration] Phys. Rev. Lett. **96**, 102002 (2006)

"Observation of $B_s^0 \to \psi(2S)\phi$ and measurement of ratio of branching fractions $B(B_s^0 \to \psi(2S)\phi)/B(B_s^0 \to J/\psi\phi)$" A. Abulencia *et al.* [CDF Collaboration] Phys. Rev. Lett. **96**, 231801 (2006)

"Measurement of the top quark mass using template methods on dilepton events in proton antiproton collisions at $\sqrt{s}$ = 1.96-TeV" A. Abulencia *et al.* [CDF Collaboration] Phys. Rev. D **73**, 112006 (2006)

"Search for $Z' \to e^+e^-$ using dielectron mass and angular distribution" A. Abulencia *et al.* [CDF Collaboration] Phys. Rev. Lett. **96**, 211801 (2006)

"Search for high-mass resonances decaying to e mu in $p\bar{p}$ collisions at $\sqrt{s}$ = 1.96-TeV" A. Abulencia *et al.* [CDF Collaboration] Phys. Rev. Lett. **96**, 211802 (2006)

"Measurement of the B/c+ meson lifetime using B/c+ −¿ J/psi e+ nu/e" A. Abulencia *et al.* [CDF Collaboration] Phys. Rev. Lett. **97**, 012002 (2006)

"Measurement of the t anti-t production cross section in p anti-p collisions at s(1/2) = 1.96-TeV using missing E(t) + jets events with secondary vertex b-tagging"** A. Abulencia *et al.* [CDF Collaboration] Phys. Rev. Lett. **96**, 202002 (2006)

"Search for large extra dimensions in the production of jets and missing transverse energy in p anti-p collisions at s(1/2) = 1.96-TeV"** A. Abulencia *et al.* [CDF Collaboration] Phys. Rev. Lett. **97**, 171802 (2006)

"Measurement of the ratio of branching fractions B(D0 $\to K^+\pi^-$) / B(D0 $\to K^-\pi^+$) using the CDF II Detector" A. Abulencia *et al.* [CDF Collaboration] Phys. Rev. D **74**, 031109 (2006)

"Search for new physics in lepton + photon + X events with 305 pb^{-1} of $p\bar{p}$ collisions at $\sqrt{s}$ = 1.96-TeV" A. Abulencia *et al.* [CDF Collaboration] Phys. Rev. Lett. **97**, 031801 (2006)

"Measurement of the b jet cross-section in events with a Z boson in $p\bar{p}$ collisions at $\sqrt{s}$ = 1.96-TeV" A. Abulencia *et al.* [CDF Collaboration] Phys. Rev. D **74**, 032008 (2006)

"Top quark mass measurement from dilepton events at CDF II with the matrix-element method" A. Abulencia *et al.* [CDF Collaboration] Phys. Rev. D **74**, 032009 (2006)

"Search for a neutral Higgs boson decaying to a W boson pair in p antip collisions at $\sqrt{s}$ = 1.96-TeV" A. Abulencia *et al.* [CDF Collaboration] Phys. Rev. Lett. **97**, 081802 (2006)

"Measurement of the tanti-t Production Cross Section in p anti-ptnipbar Collisions at $\sqrt{s}$ = 1.96-TeV" A. Abulencia *et al.* [CDF Collaboration] Phys. Rev. Lett. **97**, 082004 (2006)

"Measurement of the B_s^0 - $\bar{B}^0$(s) Oscillation Frequency" A. Abulencia *et al.* [CDF - Run II Collaboration] Phys. Rev. Lett. **97**, 062003 (2006) [AIP Conf. Proc. **870**, 116 (2006)]

"Search for excited and exotic muons in the $\mu\gamma$ decay channel in $p\bar{p}$ collisions at $\sqrt{s}$ = 1.96-TeV" A. Abulencia *et al.* [CDF Collaboration] Phys. Rev. Lett. **97**, 191802 (2006)

"Observation of B^0 (s) $\rightarrow K^+K^-$ and Measurements of Branching Fractions of Charmless Two-body Decays of B^0 and B_s^0 Mesons in $\bar{p}p$ Collisions at $\sqrt{s}$ = 1.96-TeV" A. Abulencia *et al.* [CDF Collaboration] Phys. Rev. Lett. **97**, 211802 (2006)

"Measurement of the $t\bar{t}$ Production Cross Section in $p\bar{p}$ collisions at $\sqrt{s}$ = 1.96-TeV using Lepton + Jets Events with Jet Probability b^- tagging" A. Abulencia *et al.* [CDF Collaboration] Phys. Rev. D **74**, 072006 (2006)

"Measurement of the $t\bar{t}$ Production Cross Section in $p\bar{p}$ collisions at $\sqrt{s}$ = 1.96-TeV in the All Hadronic Decay Mode" A. Abulencia *et al.* [CDF - Run II Collaboration] Phys. Rev. D **74**, 072005 (2006)

"Search for V + A current in top quark decay in p anti-p collisions at s(1/2) = 1.96-TeV"** A. Abulencia *et al.* [CDF Collaboration] Phys. Rev. Lett. **98**, 072001 (2007)

"Measurement of the Lambda/b0 lifetime in Lambda/b0 –¿ J/psi Lambda0 in p anti-p collisions at s(1/2) = 1.96-TeV"** A. Abulencia *et al.* [CDF Collaboration] Phys. Rev. Lett. **98**, 122001 (2007)

"The CDF II extremely fast tracker upgrade" A. Abulencia *et al.* [CDF Collaboration] Nucl. Instrum. Meth. A **572**, 358 (2007)

"Observation of B_s^0 - $\bar{B}^0$(s) Oscillations" A. Abulencia *et al.* [CDF Collaboration] Phys. Rev. Lett. **97**, 242003 (2006)

"Observation of Exclusive Electron-Positron Production in Hadron-Hadron Collisions" A. Abulencia *et al.* [CDF Collaboration] Phys. Rev. Lett. **98**, 112001 (2007)

"Measurement of the B^+ production cross-section in $p\bar{p}$ collisions at $\sqrt{s}$ = 1960-GeV" A. Abulencia *et al.* [CDF Collaboration] Phys. Rev. D **75**, 012010 (2007)

"Search for Exotic S=-2 Baryons in proton-antiproton Collisions at sqrt(s) = 1.96 TeV" A. Abulencia *et al.* [CDF Collaboration] Phys. Rev. D **75**, 032003 (2007)

"Search for anomalous production of multi-lepton events in $p\bar{p}$ collisions at $\sqrt{s}$ = 1.96-TeV" A. Abulencia *et al.* [CDF Collaboration] Phys. Rev. Lett. **98**, 131804 (2007)

"Measurement of the Inclusive Jet Cross Section using the k_T algorithm in $p\bar{p}$ collisions at $\sqrt{s}$ = 1.96-TeV with the CDF II Detector" A. Abulencia *et al.* [CDF - Run II Collaboration] Phys. Rev. D **75**, 092006 (2007) [Erratum-ibid. D **75**, 119901 (2007)]

"Observation of WZ Production" A. Abulencia *et al.* [CDF Collaboration] Phys. Rev. Lett. **98**, 161801 (2007)

"Search for New Physics in Lepton + Photon + X Events with 929 pb-1 of ppbar Collisions at roots = 1.96 TeV" A. Abulencia *et al.* Phys. Rev. D **75**, 112001 (2007)

"First Measurement of the Ratio of Central-Electron to Forward-Electron W Partial Cross Sections in p^- pbar Collisions at sqrt s = 1.96 TeV" A. Abulencia *et al.* [CDF Collaboration] Phys. Rev. Lett. **98**, 251801 (2007)

"Inclusive Search for New Physics with Like-Sign Dilepton Events in ppbar Collisions at sqrts = 1.96 TeV" A. Abulencia *et al.* [CDF Collaboration] Phys. Rev. Lett. **98**, 221803 (2007)

"Measurement of $\sigma_{\chi c2}\mathcal{B}(\chi_{c2} \to J/\psi\gamma)/\sigma_{\chi c1}\mathcal{B}(\chi_{c1} \to J/\psi\gamma)$ in $p\bar{p}$ Collisions at $\sqrt{s}$ = 1.96 TeV" A. Abulencia *et al.* Phys. Rev. Lett. **98**, 232001 (2007)

"Measurement of the top-quark mass using missing E_T+jets events with secondary vertex b-tagging at CDF II" T. Aaltonen *et al.* [CDF Collaboration] Phys. Rev. D **75**, 111103 (2007)

FIELDS OF STUDY

Major Field: Physics

TABLE OF CONTENTS

Page

Abstract ii

Dedication iv

Acknowledgments v

Vita vi

List of Tables xvii

List of Figures xix

Chapters:

1. Introduction 1

2. Motivations for a Higgs Boson Search 5

    2.1 The Standard Model 5
        2.1.1 Electroweak Symmetry 7
        2.1.2 The Z Boson 10
        2.1.3 Goldstone's Theorem 11
        2.1.4 Standard Model Higgs Mechanism 12
    2.2 Limits on the Higgs Boson Mass 14
        2.2.1 Theoretical Limits 15
        2.2.2 Limits from Experimental Searches 15
    2.3 Tevatron Experimental Searches 19
    2.4 Other Higgs Models 24
    2.5 Summary 25

3. Experimental Apparatus 27

3.1 Tevatron 27
3.2 Detector Overview 30
3.2.1 Cerenkov Luminosity Counter (CLC) 33
3.2.2 Silicon Tracking Systems 33
3.2.3 Central Outer Tracker (COT) 35
3.2.4 Solenoid 37
3.2.5 Calorimeters 37
3.2.6 Muon Detectors 38
3.3 Usage of the CDF Detector 40
3.3.1 Event Triggers 40
3.3.2 Lepton Identification 42
3.3.3 Jet Modeling 45
3.3.4 Missing Transverse Energy Measurement 46
3.3.5 SecVtx Algorithm 47

4. Event Selection 50

4.1 Event Criteria 50
4.1.1 Event Triggering 51
4.1.2 Lepton Selection 53
4.1.3 Jet Selection 54
4.1.4 "*b*-tagging" 57
4.2 Signal Acceptance 59
4.3 Backgrounds 59
4.3.1 Monte Carlo Modeled Backgrounds 61
4.3.2 "Mistags" 64
4.3.3 "Fake Leptons" 66
4.4 Expected Number of Events 68

5. Advanced Event Selection 72

5.1 Introduction to Neural Networks 72
5.2 Jet Energy Neural Network Correction 75
5.3 Classification Artificial Neural Network 79
5.3.1 Training and Structure of the Neural Network 79
5.3.2 Validation of Kinematic Input Variables 82
5.3.3 Test of Neural Network output 83
5.4 Summary 83

6. Systematic Errors 98

6.1 Normalization Uncertainties 98
6.1.1 Correlated Uncertainties 99
6.1.2 Z + heavy flavor Normalization 100
6.1.3 Other Monte Carlo Normalizations 100
6.1.4 Mistag background 101
6.1.5 Fake Lepton background 102
6.2 Shape Systematics 102
6.3 Summary 104

7. Results 106

7.1 CANN Output 106
7.2 Shape Fitting 108
7.3 Limit on Higgs Production 112
7.4 Description of the most Higgs-like Event 114

8. Conclusions 116

8.1 Combination with Other Tevatron Higgs Searches 116
8.2 Outlook for Full Tevatron Run 117

Appendices:

A. Classification Artificial Neural Network Correlations 121

Bibliography 126

LIST OF TABLES

Table		Page
2.1	The generations of fermions in the Standard Model.	6
2.2	The force-carrying bosons of the Standard Model.	7
4.1	Summary of event selection and subsections where details are covered.	51
4.2	Central electron trigger path.	52
4.3	Central muon trigger paths.	52
4.4	Tight electron requirements	55
4.5	Loose electron requirements	55
4.6	Tight muon requirements	56
4.7	Loose muon requirements	56
4.8	Acceptance of $ZH \rightarrow \ell^+\ell^- b\overline{b}$ after event selection cuts	60
4.9	Expected $ZH \rightarrow l^+l^- b\bar{b}$ events after double tag selections for a range of Higgs masses.	60
4.10	Expected $ZH \rightarrow l^+l^- b\bar{b}$ events after single tag (not including double tag) selection for a range of Higgs masses.	61
4.11	Muon events background expected and data found table	70
4.12	Electron events background expected and data found table	71

6.1 Systematic uncertainties for single tag channel 104

6.2 Systematic uncertainties for double tag channel 105

7.1 Expected and observed limits for $\sigma(ZH) \cdot BR(H \rightarrow bb)$(95% CL). Single-tag and double-tag samples are shown separate and combined. 112

8.1 Expected luminosity with more data 119

A.1 Correlation of CANN input variables 123

A.2 Correlations of CANN input variables and Z+jet ZH discriminant . . 124

A.3 Correlations of CANN inputs and ZH , $t\bar{t}$ discriminate 125

LIST OF FIGURES

Figure **Page**

2.1 Example of electroweak forces 10

2.2 Example of symmetry breaking 11

2.3 SM Higgs boson tree decays 14

2.4 Theoretical limits on the SM Higgs boson mass 16

2.5 Radiative loops of electroweak objects 16

2.6 Current limits of Standard Model Higgs boson 18

2.7 Parton collider Higgs boson production mechanisms 19

2.8 Production of Standard Model Higgs boson at the Tevatron ($\sqrt{s}$ = 1.96 TeV) 20

2.9 Decays of Standard Model Higgs boson for a given mass 21

2.10 The $\sigma \times BR(V)$ of the main Higgs boson searches per 1 fb^{-1} of Tevatron data. 23

2.11 Tevatron working group estimates for Higgs discovery 25

2.12 The constrained MSSM effects on a Standard Model like Higgs boson 26

3.1 Tevatron accelerator chain 28

3.2 A side view of the CDF Run II detector. 31

3.3 A simplistic portrayal of how particles behave within the CDF detector. 32

3.4 The CDF Run II silicon detectors 34

3.5 Side view of the COT detector 36

3.6 Details of the CDF muon detectors 39

3.7 CDF jet energy uncertainties 46

3.8 SecVtx efficiency 48

4.1 Higgs boson generator b quark kinematics 58

4.2 Feynman diagram of Z + $b\bar{b}$ or $c\bar{c}$ 62

4.3 Feynman diagram of $t\bar{t}$ in a dilepton decay 63

4.4 Feynman diagrams of ZZ and ZW in a dilepton decay 64

4.5 SecVtx mistag rate 65

4.6 Determination of electron fake rates 67

5.1 Feed-forward network architecture 74

5.2 Thought experiment of NN jet energy correction 77

5.3 Effect of the jet energy correction neural network 78

5.4 CANN output of training sample 85

5.5 Optimization of the classification artificial neural network 86

5.6 First set of CANN shapes 87

5.7 Second set of CANN shapes 88

5.8 Pretag kinematic distributions 1 89

5.9 Pretag kinematic distributions 2 90

5.10 Single tagged kinematic distributions 1 91

5.11 Single tagged kinematic distributions 2 92

5.12 Double tagged kinematic distributions 1 93

5.13 Double tagged kinematic distributions 2 94

5.14 CANN pretagged in Data 95

5.15 Pretagged CANN data compared to Monte Carlo expectations. 96

5.16 Pretagged CANN discriminate projected slices 97

6.1 Jet energy scale systematics 103

7.1 NN data output distributions 107

7.2 Single tagged NN projection 109

7.3 Double tagged NN projects 110

7.4 95% confidence level upper limits 113

7.5 Various event displays of event in the 115

8.1 CDF combination of Higgs searches 118

8.2 Tevatron combined Higgs search limits 119

A.1 Distribution of correlation coefficients 122

CHAPTER 1

INTRODUCTION

Issac Newton's theory of gravitation [1] is one of the cornerstones of physics. A basic concept that is taught in high school and freshman college physics is that the gravitational force is proportional to the product of the masses of the two objects divided by the square of the distance between them.

$$F_{12} \propto \frac{m_1 \cdot m_2}{r_{12}^2} \tag{1.1}$$

The first time that I came across this equation as a high school student, I asked "What is the source of mass?" The teacher's response was unsatisfactory. In an ideal classroom setting, he would have been able to give either a brief explanation or help me conduct my own research into the matter. However, given the expectations of high school, with standardized tests to teach towards, he skipped this opportunity to go deeper.

As a graduate student today, I now sympathize with the difficulty that my question posed for the teacher. Unlike other topics taught at that level, the explanation for the origin of mass is unresolved. In fact, theories that attempt to answer my question come from a separate field. At the time, we were studying classical gravitational physics which relates to objects the size of moons, planets and stars. However, the

common explanation of the source of mass lies within a field that deals with objects smaller than the atom.

The field of sub-atomic physics is very successful in explaining the experimental data. The name for the encompassing theory is the Standard Model (SM). Within the SM, it is theorized that the source of mass comes from a particle's interaction with a component of the vacuum that permeates everywhere called the Higgs field. While there is indirect evidence for the Higgs field, a linchpin for confirming this theory is to discover the manifestation of the field, the Higgs boson. Some features of the Higgs are known, such as how it should decay. Its mass is not known, but it can be inferred from other measurements of SM objects. Greater details of the basics of the Standard Model of particle physics and the Higgs mechanism is presented in Chapter 2.

Higgs bosons are produced in high energy collisions of elementary particles. Currently, the highest energy collisions take place at the Tevatron accelerator, located in suburban Chicago. The collisions of the Tevatron occur at twin, dueling experiments, DØ and the Collider Detector at Fermilab (CDF). This analysis uses 1 fb^{-1} data collected with the CDF detector. The Tevatron and CDF are described in Chapter 3.

This dissertation presents an analysis that searched for the Higgs boson when it is produced in conjunction with a Z boson. The search for the Higgs boson was for the mass range 100 $GeV/c^2 \leq m_H \leq 150\ GeV/c^2$. For most of this range, H decays primarily to $b\bar{b}$, a quark-antiquark pair. A b quark is similar to the components of the proton, but four times more massive than a proton. The antiparticle of the b quark, $\bar{b}$, is exactly like the b quark but with an opposite charge. Both b and $\bar{b}$ quarks produce a jet of particles that combined to have an invariant mass of the Higgs boson.

A feature of the b quark that separates it from other quarks is that it has a longer lifetime. This fact is exploited for "tagging" jets from b quarks. The Z boson is a neutral particle with a mass 91 times that of a proton. In the search, two oppositely charged leptons ($\ell^+\ell^-$), either electrons or muons, were used to identify the Z boson. This channel occurs the least often at the Tevatron compared to other SM Higgs boson searches by a factor of three to five.

Chapter 4 further details how to identify candidates for $ZH \rightarrow \ell^+\ell^- b\overline{b}$ in CDF data. There are physical processes that can mimic this signature and these represent backgrounds for this Higgs search. The method for modeling these backgrounds is provided. For the 1.0 fb^{-1} of data, 0.7 signal events and 111 backgrounds events were expected.

To refine the search, two neural networks were utilized. One network improved the measurement of jet energies from the b-quark daughters of the Higgs boson. The second, a classification artificial neural network (C.A.N.N.), separated backgrounds from the ZH signal. Chapter 5 provides a theoretical explanation of neural networks and how they were implemented for this analysis.

Chapter 6 is a description of the systematic errors that were considered for the $ZH \rightarrow \ell^+\ell^- b\overline{b}$ search. The two most significant were the uncertainty in the efficiency for "tagging" b jets and the amount of data collected. Other important systematic errors were the jet energy scale (JES) and background cross section uncertainties.

Chapter 7 shows the results of this analysis when applied to data. The CANN output did not show sufficient evidence for the Higgs boson and a limit was placed on the production of ZH. The upper limit on the $\sigma(ZH) \cdot BR(H \rightarrow b\bar{b})$ is set with 95% confidence, to 1.7 pb (1.1 pb) for a Higgs boson mass of 100 GeV/c^2 (150 GeV/c^2).

In the concluding section, Chapter 8, this search is put into context with other Tevatron analyses. Despite having the lowest cross section and branching ratio of all the low mass SM Higgs searches, the search for $ZH \rightarrow \ell^+\ell^- b\overline{b}$ is one of the most sensitive searches.

CHAPTER 2

MOTIVATIONS FOR A HIGGS BOSON SEARCH

This chapter is intended as an introduction to the Standard Model (SM) of particle physics. A feature of the SM is that each particle is predicted to be massless, a false conclusion. The Higgs mechanism was proposed in the 1960s to correct this flaw. As a consequence of this theory, a new physical particle, the Higgs boson, must exist. Section 2.2 discusses previous searches for this particle and theoretical constraints on the possible Higgs boson mass (m_H). The chapter ends with a description of current searches for this particle.

2.1 The Standard Model

The Standard Model of particle physics is a very successful physics theory. It is a combination of both the electroweak theory and quantum chromodynamics (QCD). The combined model is in very good agreement with experimental data [2]. It has successfully predicted the existence of the top quark [3, 4], and recently the mixing angle of B_s [5, 6, 7]. In the SM, there are two types of fundamental particles, fermions with spin 1/2 and bosons with integral spin. Fermions are normally thought to be matter while gauge bosons are thought to be force carriers.

Quarks			Charge
$\begin{pmatrix} up \\ down \end{pmatrix}$	$\begin{pmatrix} charm \\ strange \end{pmatrix}$	$\begin{pmatrix} top \\ bottom \end{pmatrix}$	$+2/3$ $-1/3$
Leptons			Charge
$\begin{pmatrix} e\ (electron) \\ \nu_e\ (electron\ neutrino) \end{pmatrix}$	$\begin{pmatrix} \mu \\ \nu_\mu \end{pmatrix}$	$\begin{pmatrix} \tau \\ \nu_\tau \end{pmatrix}$	-1 0

Table 2.1: The generations of fermions in the Standard Model.

The fermions are further divided into two groups, leptons and quarks. The most famous example of a lepton is the electron. Other leptons are either more massive particles similar to the electron or nearly massless neutrinos. Quarks are always found to be bound together into groups called hadrons. The most common example of hadrons are the protons (2 up quarks and a down quark, uud) and neutrons (udd) that make up the nucleus in an atom. There are six quarks and six leptons, arranged in three pairs each, called generations (Table 2.1). Each successive generation has properties similar to the previous generation except for the mass of the objects.

In the Standard Model, there are four forces that govern interactions. They are, in order of strength: the strong force, the electromagnetic force, the weak force, and gravitational force. These forces are propagated by bosons (see Table 2.2). The Standard Model describes interactions of the three strongest forces; gravity is not detectable in current particle physics experiments.

The strong force is responsible for binding quarks into hadrons and protons and neutrons in nuclei. The strength of the strong force is necessary to overcome the repulsion of like-charged particles and creates tightly bound states. It also should be noted that the strength of the force grows as distance between particles increases. If particles are separated too far, the increasing energy in the field will create new

quarks. The force-carrying boson is the gluon which comes in eight different varieties. Each one of these gluons is responsible for attracting a different type of "color" combination. Color, in this case, is a charge analogous to charge in electromagnetism and comes in three varieties: red, green, and blue. The color charge is only carried by quarks and gluons. In nature, all quark combinations are required to be "colorless," meaning a combination of all three colors or a color anti-color pair. The theory that explains the interaction of quarks and gluons is quantum chromodynamics (QCD).

The weak force was combined with with electromagnetic force by Glashow, Salam, and Weinberg [8, 9, 10]. I will discuss the electroweak force in more detail in Section 2.1.1.

Force	Particle	Mass
Strong	gluon	0
Electromagnetic	photon	0
Weak	$W^{\pm}$	80 GeV/c^2
	Z^0	91 GeV/c^2
Gravitation	graviton	0

Table 2.2: The force-carrying bosons of the Standard Model.

2.1.1 Electroweak Symmetry

The easiest way to enter electroweak theory is to investigate the leptons. (Quarks are complicated by strong force interactions.) Most quantum field theories are based on groups. Particles are placed in groups and the generators of a group determine the dynamics of the particles. The electroweak theory rests on a $SU(2)_L$ (T^a = isospin) x $U(1)_Y$ (Y= hypercharge) symmetry. The mediators of the interactions of the groups

are gauge fields, corresponding to spin one bosons. These gauge bosons will later become combinations of the physical bosons seen in Table 2.2. The $U(1)_Y$ group is mediated by the B_μ field and the $SU(2)_L$ group is mediated by the three fields $W_\mu^{1,2,3}$, whose generators correspond to the 2 x 2 Pauli matrices T^a. The electric charge used in quantum electrodynamics (QED) is $Q = T_3 + Y/2$. We can group the left-handed leptons in a isodoublet and a isosinglet for the right-handed charged lepton:

$$\ell_1 = \begin{pmatrix} \nu_e \\ e^- \end{pmatrix}_L \quad (T = 2, Y = -1) \tag{2.1}$$

$$e^-_{R_1} = e^-_R \quad (T = 1, Y = 2) \tag{2.2}$$

The commutators of the fields are given by

$$[T^a, T^b] = i\epsilon^{abc} T_c, \ [Y, Y] = 0 \tag{2.3}$$

which leads to the strength of each field being

$$W^a_{\mu\nu} = \partial_\mu W^a_\nu - \partial_\nu W^a_\mu + g\epsilon^{abc} W^b_\mu W^c_\nu \tag{2.4}$$

$$B_{\mu\nu} = \partial_\mu B_\nu - \partial_\nu B_\mu \tag{2.5}$$

We can create a covariant derivative to use in the Lagrangian from the field strengths:

$$D^\mu \equiv \partial^\mu + igW^\mu T_\mu + i\frac{g'}{2} B^\mu Y \tag{2.6}$$

where g, g' are independent couplings of the $SU(2)_L$ and $U(1)_Y$ groups, respectively. Applying the isodoublet and isosinglet to this derivative yields this Lagrangian:

$$\mathcal{L} = \ell^* i\gamma_\mu D^\mu \ell + \overline{e}^* i\gamma_\mu D^\mu \overline{e} - \frac{1}{4} W_{\mu\nu a} W^{\mu\nu}_a - \frac{1}{4} B_{\mu\nu} B^{\mu\nu}. \tag{2.7}$$

Investigating just the interaction terms

$$\mathcal{L}_{int} = -gW^\mu_a l^* \gamma_\mu T_a l - \frac{g\prime}{2} B^\mu l^* \gamma_\mu Y \ell - gW^\mu_a \overline{e}^* \gamma_\mu T_a \overline{e} - \frac{g\prime}{2} B^\mu \overline{e}^* \gamma_\mu Y \overline{e} \tag{2.8}$$

With some mathematical manipulation this Lagrangian can be rewritten as

$$\begin{aligned}\mathcal{L} = \quad & \ell^* \imath\gamma^\mu \partial_\mu \ell + \bar{e}\imath\gamma^\mu \partial_\mu e - \tfrac{g}{\sqrt{2}}[W_-^\mu \ell^* \gamma_\mu T_- \ell + W_+^\mu \ell^* \gamma_\mu T_+ \ell] \\ & -\ell^* \gamma_\mu [A^\mu Q + Z^\mu Q_Z]\ell - \bar{e}^* \gamma_\mu [A^\mu Q + Z^\mu Q_Z]\bar{e}\end{aligned} \tag{2.9}$$

where $\tan\theta_W \equiv \frac{g'}{g}, Q \equiv g\sin\theta_W$, and $Q_Z \equiv \frac{g}{\cos\theta_W} = (T_3 - \sin^2\theta_W Q)$. In addition the fields have been grouped as

$$W_\mp^\mu \equiv \quad \tfrac{W_1^\mu \pm \imath W_2^\mu}{\sqrt{2}} \tag{2.10}$$

$$T^\pm \equiv \quad \tfrac{T_1 \pm \imath T_2}{2} \tag{2.11}$$

$$A^\mu \equiv \quad \sin\theta_W W_3^\mu + \cos\theta_W B^\mu, \ \textit{and} \tag{2.12}$$

$$Z^\mu \equiv \quad \cos\theta_W W_3^\mu - \sin\theta_W B^\mu. \tag{2.13}$$

The above Lagrangian combines the electromagnetic force with the weak force, completing the electroweak symmetry. The $W^\pm$ and Z^0 bosons are represented through their respective gauge bosons and the photon is represented by the A^μ term. There is a charge carrying current that mediates the interaction between the electron and the neutrino. The neutral currents, Z and A, mediate interactions between leptons and anti-leptons. The electromagnetic force is proportional to electrical charge (Q) and is greater than the electroweak forces because of dependencies on the values of g and g'. The interactions of SM particles can be demonstrated using Feynman diagrams. Examples of these diagrams involving the electroweak force are demonstrated in Figure 2.1:

The first problem that should be apparent for this Lagrangian is the lack of a mass term for the leptons. The problem is that $\ell\ell$, ℓe and ee terms are not U(1) invariant and break the symmetry. Similarly, there are no mass terms for the W and

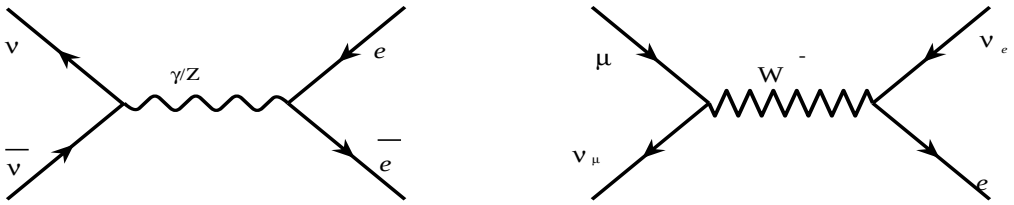

Figure 2.1: Example of electroweak forces: At left is shown electromagnetic or weak neutral currents going through either a photon or a Z. At right is an example of the weak charged current, a muon decaying through the W boson.

Z bosons. However, experimentally the W and Z bosons are observed to have mass, thus indicating that the electroweak symmetry is broken [11].

2.1.2 The Z Boson

The Z boson is of note in this dissertation since it plays a prominent role in the analysis. It is the neutral current component of the weak force. It was first discovered in 1983 at CERN's UA1 and UA2 experiments [12, 13]. The latest value for the Z boson mass is $91.1875 \pm 0.0021\ GeV/c^2$ [14]. It decays into charged lepton pairs about equally, with an average rate of $3.3658 \pm 0.0023\%$ [2]. As a comparison, the Z branching ratio to invisible particles (neutrinos) is $20.00 \pm 0.06\%$, and to hadrons, $69.91 \pm 0.06\%$.

At the Tevatron, the theoretical $\sigma(Z) \times BR(Z \to \ell^+\ell^-)$ is $251.3 \pm 5.0pb$ [15, 16, 17, 18, 19, 2]. The most recent measurement of $Z \to e^+e^-$ at CDF was with 1.1 fb^{-1} of data and is $263.34 \pm 0.93_{stat} \pm 3.79_{syst.} \pm 15.2_{lumi.}pb$[20].

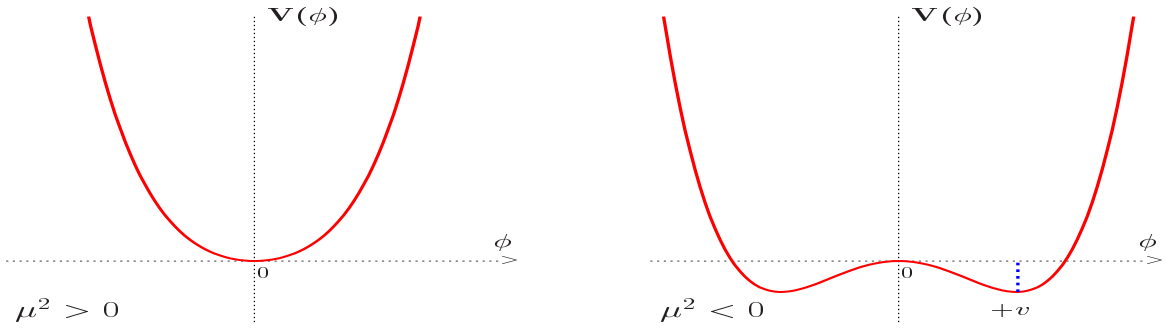

Figure 2.2: Example of symmetry breaking. The potential V of the scalar field ϕ in the case $\mu^2 > 0$ (left) and $\mu^2 < 0(right)$ [11].

2.1.3 Goldstone's Theorem

The basics of symmetry breaking is best demonstrated through Goldstone's theorem [21]. It starts with a simple Lagrangian that is drawn in Figure 2.2

$$\mathcal{L} = \frac{1}{2}\partial_\mu\phi\partial^\mu\phi - V(\phi) \tag{2.14}$$

$$V(\phi) = \frac{1}{2}\mu^2\phi^2 + \frac{1}{2}\lambda\phi^4 \tag{2.15}$$

Since there are no cubic terms, this Lagrangian is symmetric across the $V(\phi)$ axis. If $\mu^2 \geq 0$ then the minimum of the system is located at the origin. $\mathcal{L}$ is the Lagrangian of a spin-zero particle with mass μ and λ is the self-coupling term. On the other hand, if $\mu^2 < 0$ the potential $V(\phi)$ has a minimum at $-\frac{\mu^2}{\lambda} \equiv v^2$ and not at $< \phi^2 >= 0$ as in the previous case. The value v is called the vacuum expectation value (vev) of the scalar field ϕ. In this case, $\mathcal{L}$ is no longer the Lagrangian of the particle. Instead, it is necessary to expand equations 2.14 and 2.15 around either v or $-v$ by defining

$\phi = v + \sigma$. The new equation will have a σ^3 term breaking the symmetry.

$$\mathcal{L} = \frac{1}{2}\partial_\mu\sigma\partial^\mu\sigma - (-\mu^2)\sigma^2 - \sqrt{-\mu^2\lambda}\sigma^3 - \frac{\lambda}{4}\sigma^4 + const. \tag{2.16}$$

This is the simplest example of spontaneous symmetry breaking.

For a potential with more dimensions, consider four scalar fields ϕ_i with $i = 0, 1, 2, 3$. The Lagrangian for the system is:

$$\mathcal{L} = \frac{1}{2}\partial_\mu\phi_i\partial^\mu\phi_i - \frac{1}{2}\mu^2(\phi_i\phi_i) - \frac{1}{4}\lambda(\phi_i\phi_i)^2 \tag{2.17}$$

Similar to the last case, if $\mu^2 < 0$ a vev at $\phi_i^2 = v^2$ is created and we can expand around one of the minima, so that $\phi_0 = v + \sigma$. We expand around this new position and can rewrite the other fields $\phi_i = \pi_i$ with i = 1,2,3. The new Lagrangian of the fields σ and π_i is:

$$\mathcal{L} = \frac{1}{2}\partial_\mu\sigma\partial^\mu\sigma - \frac{1}{2}(-2\mu^2)\sigma^2 - \lambda v\sigma^3 - \frac{\lambda}{4}\sigma^4 + \frac{1}{2}\partial_\mu\pi_i\partial^\mu\pi_i - \frac{\lambda}{4}(\pi_i\pi_i)^2 - \lambda v\pi_i\pi_i\sigma - \frac{1}{2}\pi_i\pi_i\sigma^2 \tag{2.18}$$

Again the symmetry for ϕ_0 is broken but now there are also no mass terms for the π_i terms. This leads to Goldstone's theorem: for every spontaneously broken continuous symmetry, there exists a massless scalar particle called a Nambu-Goldstone boson. The number of Goldstone bosons is equivalent to the number of broken generators. For Electroweak symmetry, these Goldstone bosons will become the longitudinal parts of the $W^\pm$ and Z bosons.

2.1.4 Standard Model Higgs Mechanism

The manner in which the minimal Standard Model generates masses for gauge boson and fermions without violating the SU(2) x U(1) gauge invariance was theorized

by Higgs, Brout, Englert, Guralnik, Hagen, and Kibble [22, 23, 24, 25]. For the sake of brevity, their solution is referred to as the Higgs mechanism. To break electroweak symmetry, a mechanism must force the three gauge bosons $W^{\pm}$ and Z to have a mass while keeping photons massless. Also, Quantum Electrodynamics (QED) must contain an exact symmetry for the electrical charge. Therefore we need 3 degrees of freedom for the scalar fields. The simplest choice is a complex SU(2) doublet of scalar fields ϕ

$$\phi = \begin{pmatrix} \phi^+ \\ \phi^0 \end{pmatrix} \equiv \begin{pmatrix} \phi_1 + \imath\phi_2 \\ (v+h) + \imath\phi_4 \end{pmatrix}, \ (T = 2, \ Y = +1) \tag{2.19}$$

where ϕ^+ and ϕ^0 are complex. To equation (2.9) we need to add an invariant scalar field Lagrangian,

$$\mathcal{L}_S = (D^\mu\phi)^\dagger(D_\mu\phi) - \mu^2\phi^\dagger\phi - \lambda(\phi^\dagger\phi)^2 \tag{2.20}$$

The ϕ field can undergo SU(2) x U(1) transformations to

$$\phi = \frac{1}{\sqrt{2}} \begin{pmatrix} 0 \\ v + H \end{pmatrix} \text{ with } v = \sqrt{-\frac{\mu^2}{\lambda}} \tag{2.21}$$

This form is important because it is $U(1)_{QED}$ invariant, and is called the unitary gauge. This will match the changes we made in the electroweak section. If we expand the $(D^\mu\phi)^\dagger(D_\mu\phi)$ term we will find the mass terms of the gauge bosons.

$$M_W = \frac{1}{2}vg \tag{2.22}$$

$$M_Z = \frac{1}{2}v\sqrt{g^2 + g'^2} = \frac{M_W}{\cos\theta} \tag{2.23}$$

$$M_A = 0 \tag{2.24}$$

Taking the other part of the scalar Lagrangian we find $M_H = \lambda v^2$ where λ is a self interaction coupling. Because we can accurately measure g, M_Z, and M_W, we can find that the vacuum expectation value is approximately 246 GeV. We have now applied Goldstone's theorem to the broken electroweak symmetry using the Higgs mechanism.

Figure 2.3: SM Higgs boson tree decays. Tree level decay constants for Standard Model Higgs into gauge bosons (V=W/Z) and fermions

We can now investigate the cross terms of the ℓ and e from equation (2.2) to form a fermion part of the invariant Lagrangian using

$$\mathcal{L} = -g_e \bar{e} \phi^\dagger \ell + h.c. \tag{2.25}$$

where g_e is the coupling constant of electrons to the Higgs field. From the last Lagrangian we find: $m_e = g_e v/2, m_\nu = 0$. The couplings of the Higgs are shown in Figure 2.3. We now have a mechanism for producing fermion mass (the neutrinos are assumed to be massless to good approximation.)

2.2 Limits on the Higgs Boson Mass

We can limit the scope of our searches for the SM Higgs boson by considering its constraints from both theory and from experimental data. The experimental limits come from both direct searches and from constraints on the SM from other measurements.

2.2.1 Theoretical Limits

Before investigating the search for the Higgs boson, the theoretical limits on the Higgs mass should be considered. An upper limit is set by the so called unitary bound. If the Higgs mass is greater than this bound, then either new physics exists beyond the Standard Model at the TeV scale or the probability of some events to occur is greater than 1, a physical impossibility. The limit for this scale is on the order of 1 TeV.

For a lower limit, there is a requirement that the vacuum maintain stability. If the Higgs scalar is too low, then couplings of the top mass dominate leaving the vacuum unstable and couplings to the vacuum less than zero. In Figure 2.4, the value of these limits are displayed versus the scale Λ that the Standard Model breaks down. If the Standard Model breaks down at the Grand Unification Theory (GUT) scale (the energy where all forces have the same strength) $\Lambda \approx 10^{16}\ GeV/c^2$ then the Higgs Mass range is $130\ GeV/c^2 \leq M_h \leq 180\ GeV/c^2$ [26].

2.2.2 Limits from Experimental Searches

In addition to theoretical limits, we can indirectly measure the Higgs mass by measuring the Standard Model's other parameters. This procedure assumes the Higgs mechanism is correct and is therefore model dependent. Accurately measured masses of the $W^{\pm}$ and Z bosons and the top quark are some of the most important measurements necessary to obtain a limit. The mass of these particles is increased mostly through the loop diagrams as shown in Figure 2.5.

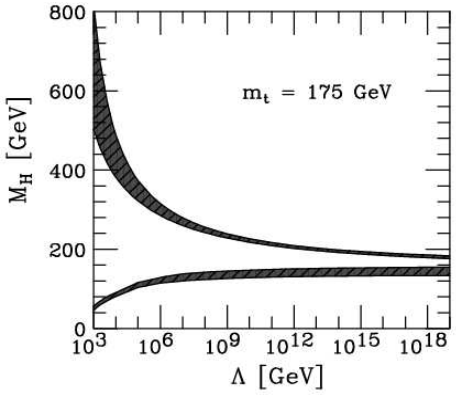

Figure 2.4: Theoretical limits on the Standard Model Higgs boson mass. The Higgs boson mass depends on what energy Λ the Standard Model breaks down. The upper band is the unitary constraint. The lower band is from the vacuum stability requirement [27]

.

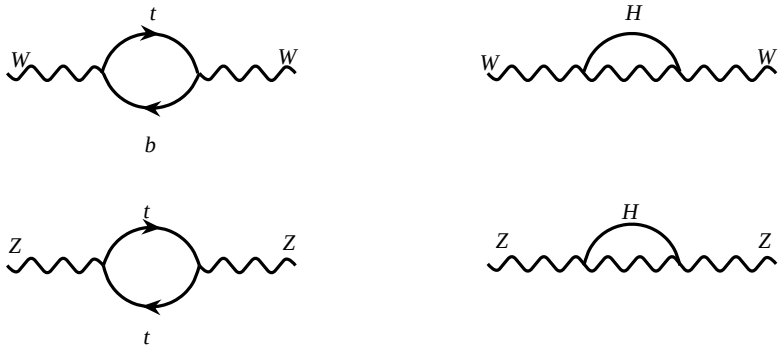

Figure 2.5: Radiative loops of electroweak objects. Precision measurement of the gauge bosons and the top bosons can provide a limit to the measurement of the Standard Model Higgs boson

The first order loops give us the following equations to calculate the effect of the Higgs mass on the gauge boson masses.

$$\rho = \frac{M_W^2}{M_Z^2(1-\sin^2\theta_W)} = 1 + \Delta\rho \tag{2.26}$$

$$\Delta\rho \equiv \frac{3G_F}{8\pi^2\sqrt{2}} m_t^2 + \frac{\sqrt{2}G_F 16\pi^2}{M_W^2}\{\frac{11}{3}\ln(M_H^2/M_W^2) + \ldots\} \tag{2.27}$$

where G_F is the Feynman coupling constant. The higher order loops have contributions mostly from the top and the Higgs boson. The top quark mass is the most accurately measured mass of the quarks. Because of the logarithmic nature of the Higgs contribution, the window for the Higgs mass is quite large. The CERN electron positron collider, LEP, carefully measured the gauge boson masses as well as $\sin\theta_W$. In Run II, of the Tevatron, the accurate measurements of the top mass and W boson have lowered the M_H range even further. The most recent world wide indirect measure is $M_H = 76^{+33}_{-24}\ GeV/c^2$. That sets an upper limit of the Higgs at 95% CL < 144 GeV/c^2. Figure 2.6 shows the region where the Higgs might reside [28, 14].

Towards the end of LEP operation, the collider center-of-mass energy was increased to directly search for the Higgs boson. The main search channels were through the production of the Higgs coupled with a Z boson. They set the lower limit of the Higgs mass to be 114.4 GeV/c^2 as can be seen in the shaded region in Figure 2.6 (right). It was expected that the lower limit at LEP would be near 115.3 GeV, but there was an approximately 3 σ excess in one experiment's search. This excess is below what is necessary to declare proof of a new particle, but is significant [29]. When adding this search into the limit of the Higgs boson, the upper limit of the Higgs boson mass increases to 182 GeV/c^2.

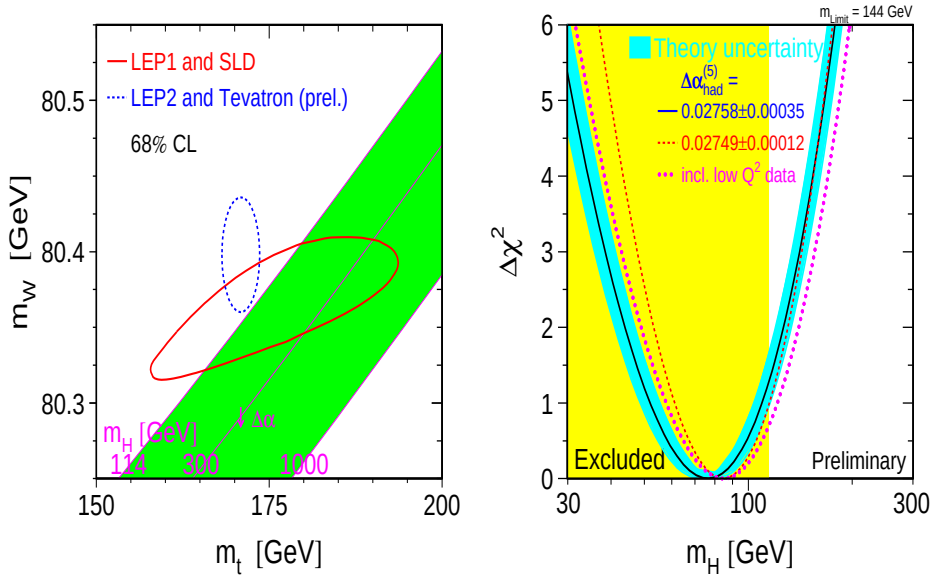

Figure 2.6: Current limits of Standard Model Higgs boson. Experimental limits on the Standard Model Higgs from precise measurements of W boson mass and the top quark mass (right) and all precision measurements (left)[14].

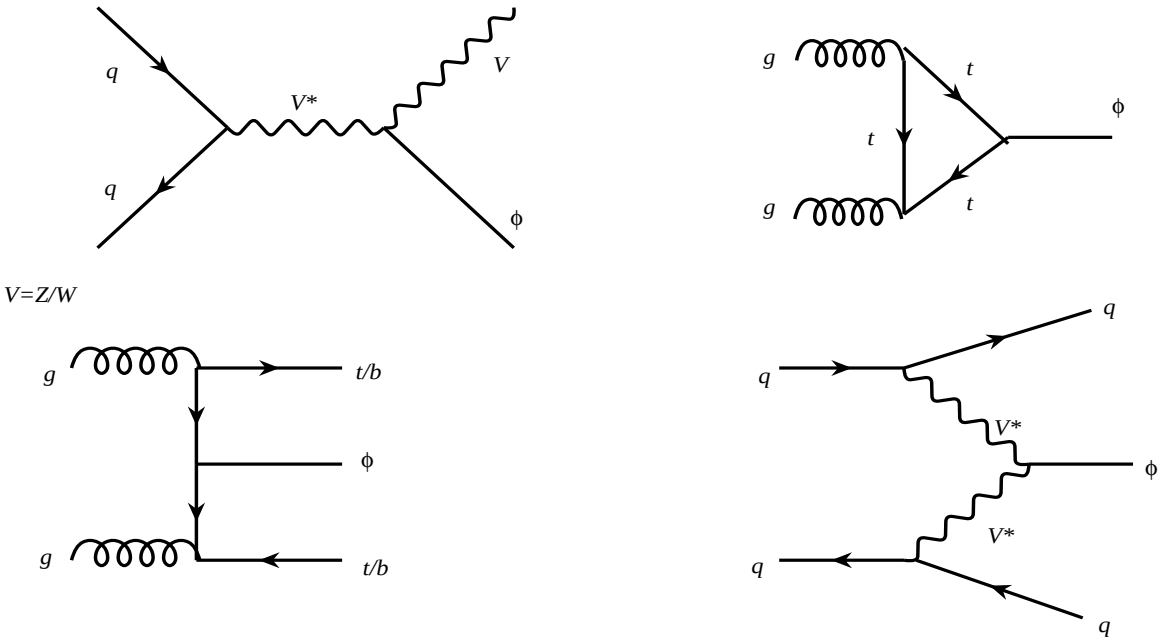

Figure 2.7: Parton collider Higgs boson production mechanisms. Main Production mechanism for Standard Model Higgs and neutral MSSM Higgs = h, H, ϕ.

2.3 Tevatron Experimental Searches

Various Higgs boson production mechanisms exist at the Tevatron and are shown in Figure 2.7. The estimated Tevatron production cross section of the SM Higgs is shown in Figure 2.8. The Higgs Working Group at Fermilab studied the sensitivity for discovery of Higgs bosons at the Tevatron. The study divided the search for the Higgs into two categories, $M_h < 135\ GeV/c^2$, and $135\ GeV/c^2 < M_h < 190\ GeV/c^2$. These two regions have different important decay modes for the Higgs boson (see Figure 2.9). The lower region decays mostly into a $b\bar{b}$ pair, while the higher masses decay mostly into two gauge bosons.

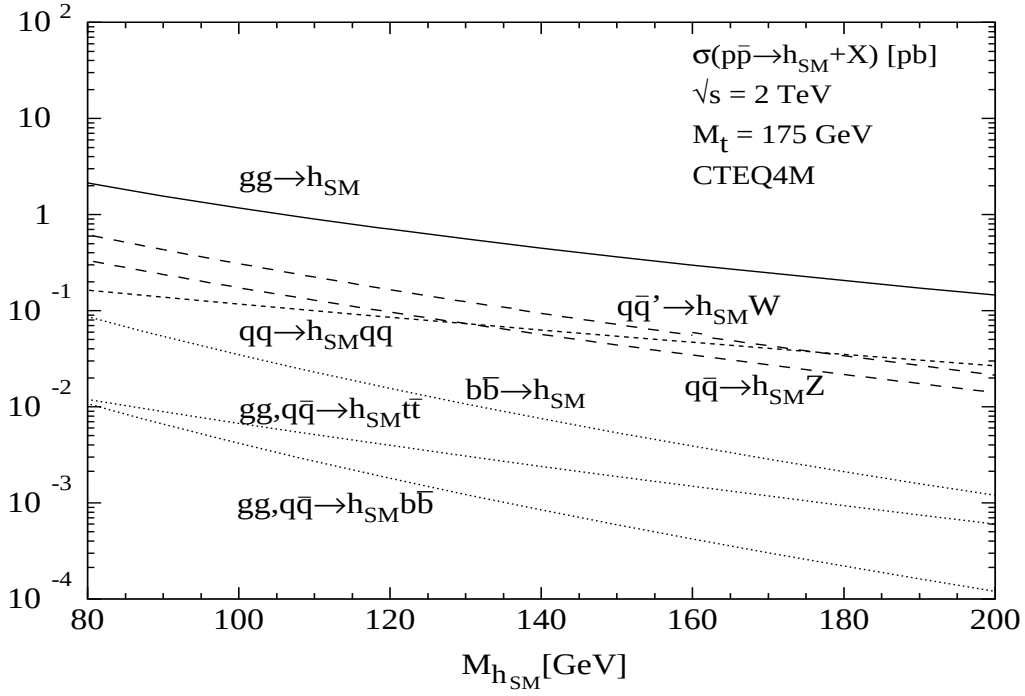

Figure 2.8: Production of Standard Model Higgs boson at the Tevatron ($\sqrt{s} = 1.96$ TeV)

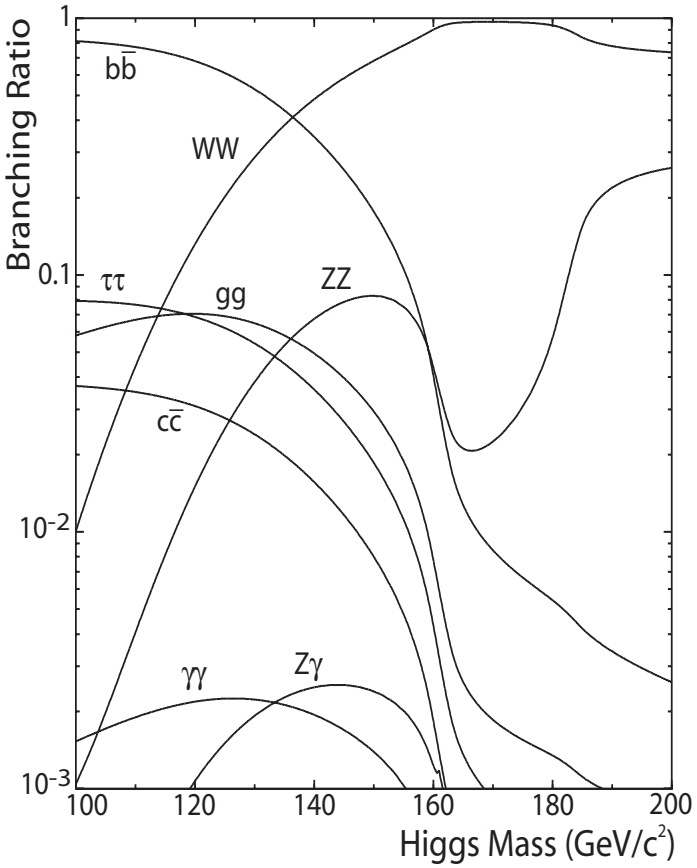

Figure 2.9: Decays of Standard Model Higgs boson for a given mass. Since the Higgs boson interacts in relation to the mass of the object, it decays to higher mass objects [26].

In the low mass region, the search is focused on VH production, where V is either a Z or a W boson. Even though these are not the primary production modes, they are the easiest to detect. The main production mode is gluon fusion into a Higgs by itself (see Figures 2.8 and 2.7). At low mass, this channel has a large background from QCD two jet processes that makes finding a Higgs signal impossible. More promising channels are the production of the Higgs boson associated with a gauge boson, because of its smaller background. However, in order to limit the confusion of distinguishing which jets came from which final state parton, VH searches are limited to instances the vector boson decays into leptons. For the $W^{\pm}$ and Z this is a small fraction of all the decays. Complicating matters even further, τ leptons are difficult to detect since they can decay hadronically. As a result, the dominant channels are:

$$p\bar{p} \rightarrow \quad ZH \rightarrow \quad \ell^+\ell^- b\bar{b} \tag{2.28}$$

$$p\bar{p} \rightarrow \quad WH \rightarrow \quad \ell\nu b\bar{b} \tag{2.29}$$

$$p\bar{p} \rightarrow \quad ZH \rightarrow \quad \nu\bar{\nu} b\bar{b} \tag{2.30}$$

where ℓ represents a charged lepton (either an electron or muon), ν represents a neutrino, and b represents a bottom quark, which decays into a b jet. These three channels break into orthogonal searches. The $ZH \rightarrow \ell^+\ell^- b\bar{b}$ channel has two charged leptons in the final state, $WH \rightarrow \ell\nu b\bar{b}$ has one charge lepton, and $ZH \rightarrow \nu\nu b\bar{b}$ has no charged lepton. The relative production of these channels is shown in Figure 2.10. All of these modes depend on identifying the b jets and measuring the invariant mass of the $b\bar{b}$ pair.

At a higher mass Higgs, it becomes easier to find Higgs events because the $H \rightarrow VV^*$ decay becomes dominant. When the WW decays into leptons, there is no large

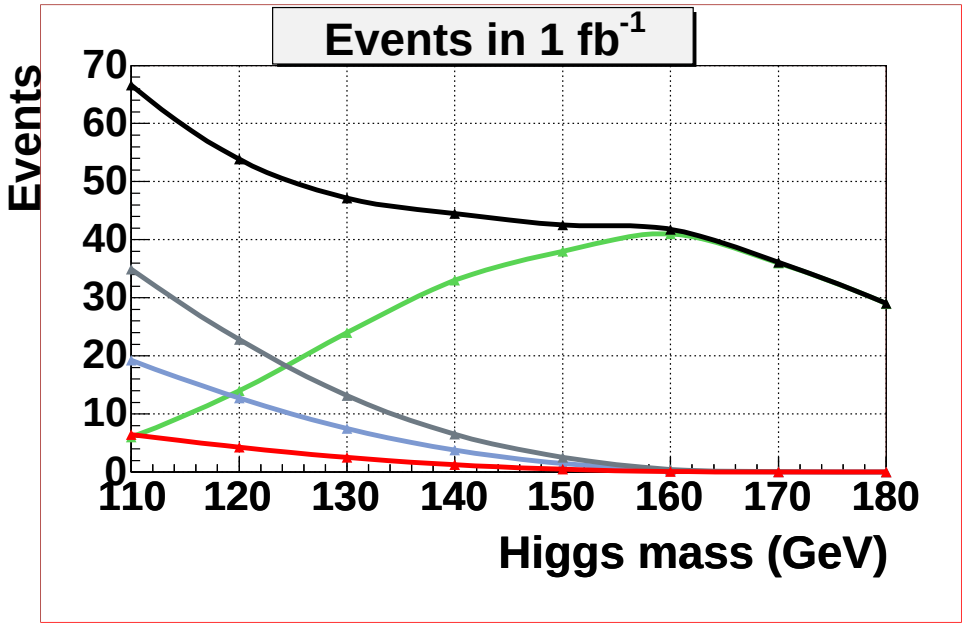

Figure 2.10: The $\sigma \times BR(V)$ of the main Higgs boson searches per 1 fb^{-1} of Tevatron data. The red line shows the $ZH \rightarrow \ell^+\ell^- b\bar{b}$ channel. The light blue line represents the $ZH \rightarrow \nu\nu b\bar{b}$ channel. The dark blue line represents $WH \rightarrow \ell\nu b\bar{b}$ channel. For these low mass analysis, $\ell = e$ *or* μ. The green line represents the amount $H \rightarrow WW^* \rightarrow \ell^+\nu\ell^-\nu$, where $\ell = e,\ \mu,$ *or* τ. The black line represents the combination of these four channels. This plot does not include the efficiency of selecting these events.

QCD background to disguise the signal. One can investigate the following processes

$$h \to \quad WW^* \quad \to \ell\nu jj \text{ and } \ell\bar{\nu}\bar{\ell}\nu \tag{2.31}$$

$$h \to \quad ZZ^* \quad \to \ell\ell jj \text{ and } \ell\bar{\ell}\nu\bar{\nu} \tag{2.32}$$

$$W^{\pm}h \to \quad \ell^{\pm}\nu WW^* \quad \to \ell\nu\ell\nu\ell\nu \tag{2.33}$$

$$W^{\pm}h \to \quad \ell^{\pm}\nu WW^* \quad \to \ell^{\pm}\nu\ell^{\pm}\nu jj \tag{2.34}$$

One of the problems with these decays is that it is less than ideal to have so many sources of missing energy in an event. It is a challenge to combine all of the information.

The Higgs Working Group[26], in a 1999 Snowmass meeting, estimated the possibility of discovering or ruling out the Standard Model Higgs. They estimated how much data would need to be collected for a 5 σ discovery, 3 σ evidence, or to rule out a Higgs of a certain mass with 95% confidence. In 2003, another group [30] estimated the sensitivity using data that was collected between 2001 and 2003. This group found a similar sensitivity for the low mass Higgs (see Figure 2.11).

The $ZH \to \ell^+\ell^- b\overline{b}$ channel has some advantages over other SM Higgs searches. Though it has the lowest cross section and branching ratio, it also has the lowest backgrounds of the low mass Higgs searches. In addition, unlike other SM Higgs searches, all the final decay products are measurable, i.e. no neutrinos.

2.4 Other Higgs Models

There are many other explanations for the electroweak symmetry breaking. A very popular one is the Super-Symmetric (SUSY) model [31, 32]. Unlike the Standard Model, it predicts five different Higgs bosons. It should be noted that the lowest mass

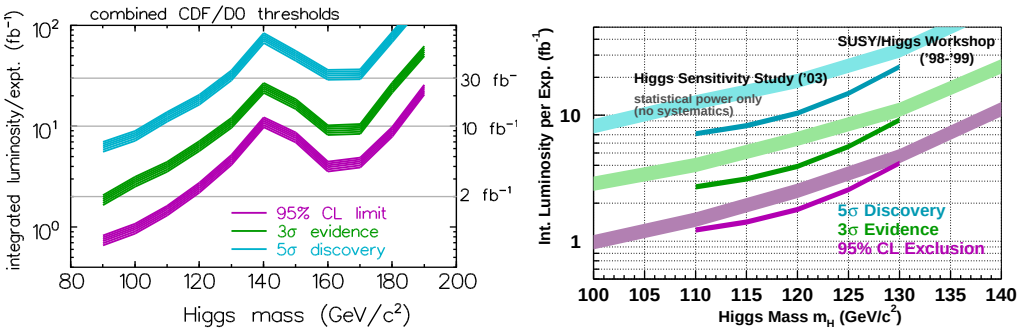

Figure 2.11: Tevatron working group estimates for Higgs discovery: how much data needs to be collected per experiment at the Tevatron to either find the Standard Model Higgs for a certain mass or exclude it [26]. The graph on the right reflects an improvement of resolution in measuring jets[30].

boson is expected to behave in a very SM like fashion, with some adjustments to the cross section and branching ratio.

Recent physical measurements have placed constraints on SUSY theory. The so-called constrained Minimal Super Symmetric Model (cMSSM) predicts a low mass Higgs boson, h, with a mass of 120 GeV/c^2, as shown in Figure 2.12. The cross section times branching ratio is slightly higher than the Standard Model in $ZH \rightarrow \ell^+\ell^- b\bar{b}$ [33, 34].

2.5 Summary

To explain the nature of elementary particles and their interactions, the Standard Model was created. It is a very healthy theory with much experimental evidence. A weakness of the model arises in the electroweak sector, where a symmetry is broken. To reconcile the problem, the Higgs mechanism was introduced. Two features of this model are that it is a possible mechanism to explain the origin of mass of elementary

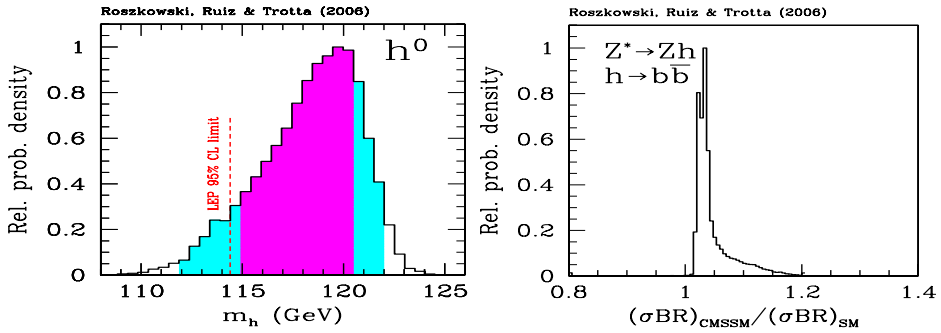

Figure 2.12: The constrained MSSM effects on a Standard Model like Higgs boson. The model favors a low mass Higgs boson (left) within the search capability of this analysis, with a slight increase of cross section times branching ratio(right)

particles and there exists a Higgs boson. To verify the Higgs Mechanism, the Higgs boson needs to be discovered.

Through previous searches, most recently at the LEP experiments, a SM Higgs boson mass below 114.4 GeV/c^2 has been excluded at a 95 % confidence level. Precision electroweak and top quark measurements have set an upper limit of the Higgs mass of 144 GeV/c^2.

Currently, the only place to conduct searches for the Higgs boson is at the Tevatron. Because of the nature of the decay rates of the Higgs boson, two search regions are in place for the SM Higgs. For higher masses, direct production of the Higgs which then subsequently decays through the gauge bosons is the best avenue for detection. For Higgs mass between 115 GeV/c^2 and 135 GeV/c^2, the best searches use associated production with either the Z or W bosons. This dissertation focuses on an associated production search where a Z boson decays into two charge leptons.

CHAPTER 3

EXPERIMENTAL APPARATUS

Experimental particle physics investigates collisions of high energy particles. A large segment of the experiments are man-made collisions of two elementary particles with velocities close to the speed of light. As of the time of this dissertation's submission (2007), the highest energy collisions take place at the Tevatron collider located in the far western Chicago suburbs. There are two collision points at the Tevatron, each with its own associated experiment. They are named the Collider Detector at Fermilab (CDF) and DØ. These experiments gather information about the byproducts of these collisions and study physics at the smallest scale. In Section 3.1, I discuss how the Tevatron works. Section 3.2 focuses on CDF and how it is used for a low-mass Higgs search. I conclude with a description of key concepts and algorithms used for the $ZH \rightarrow \ell^+\ell^- b\overline{b}$ analysis in Section 3.3.

3.1 Tevatron

One of the world's largest machines, the Tevatron is a 3.9 mile circular circumference accelerator at the Fermi National Accelerator Laboratory (FNAL). It collides a 0.98 TeV beam of protons with a 0.98 TeV beam of anti-protons, for a center-of-mass energy of 1.96 TeV [35]. During Run II of the Tevatron, the center-of-mass energy

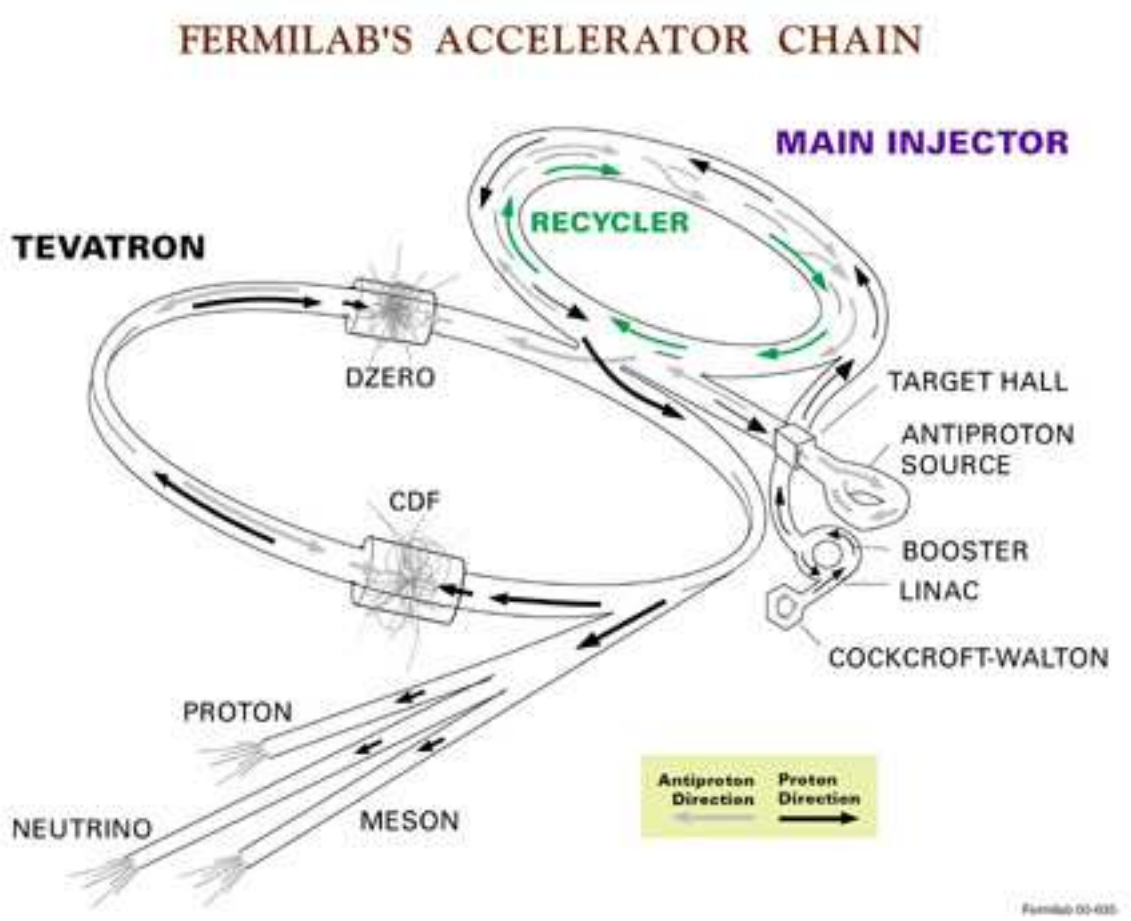

Figure 3.1: Tevatron accelerator chain. A sketch of the accelerator chain used at the Fermi National Accelerator Laboratory. Contained is the chain that leads to collisions at CDF.

increased modestly from the earlier Run I energy of 1.8 TeV, but the upgrade resulted in a greatly increased instantaneous luminosity. Without both the great center-of-mass energy and the high luminosity, the results of this analysis would be impossible to obtain.

To achieve the energies of the Tevatron, protons undergo a journey that starts from a bottle of hydrogen gas (H_2). A small electric field attracts the hydrogen nucleus,

a single proton, towards a metal surface. A large number of the protons become H^- ions and are repelled by the metal surface. A Crockroft-Walton pre-accelerator is the next step in the proton's journey. This field increases the proton's energy to 750 keV. The protons then enter the Linac, a 150 m linear accelerator. This accelerator uses an electromagnetic field generated by a radio frequency (RF) cavity. The Linac uses a time-varying magnetic field to maintain stable beam bunches as the particles accelerate. The negative Hydrogen ions pass through a carbon foil which removes the electrons. The resulting protons then move into the Booster, a circular (r = 474 m) accelerator. Again RF cavities are utilized to increase the energy of the protons to 8 GeV. In the Booster phase, the protons undergo 20,000 rotations. The beam is then transfered into the Main Injector, a circular synchrotron. The Main Injector is used to accelerate both proton and anti-proton beams for injection into the Tevatron. This accelerator component either increases the particles energy to 150 GeV for those bunches that directly enter the Tevatron or to 120 GeV for those that are used for the creation of anti-protons.

To make anti-protons, a 120 GeV proton beam from the Main Injector is directed at a nickel target. Many different by-products arise from the collision of the beam and the target, including antiprotons through the $p+p \rightarrow p+\bar{p}+p+p$ process. To separate out the anti-protons, magnetic spectroscopy is used. One anti-proton is collected per 62,500 initial protons. The anti-protons are then sent to the Debuncher to form a continuous beam. This continuous beam is then sent to the Accumulator for storing anti-protons until they are sent to the Main Injector in preparation for collisions. Anti-protons are also collected and stored in the Recycler, a system that runs along

the Main Injecter. It collects antiprotons that have been previously injected into the Tevatron but were "discarded." It stores the antiprotons using permanent magnets.

The final stage is the Tevatron, which is the main 3.9 mile long circular track. The Tevatron uses Nb-Sn superconducting magnets, with fields up to 4.2 T, to control both proton and anti-proton beams as the energy is raised to 980 GeV with additional RF cavities. Some magnets are used to bend the beam while others are used to make sure the beam stays focused. An unfocused beam may cause great damage to the two experiment's detectors or to the accelerator itself. Focusing the beam also ensures a higher instantaneous luminosity for collisions. For colliding physics runs, 36 bunches each of protons and antiprotons are injected into the Tevatron. The bunches are spaced such that they cross every 396 ns.

The current integrated luminosity that the Tevatron has delivered to CDF is 3.0 fb^{-1}. CDF has recorded 2.5 fb^{-1} on tape. Inefficiencies occur because of problems with electronics and inefficiencies in data triggering. The current peak instantaneous luminosity has been $2.86 \times 10^{30} cm^{-2}/s$. This dissertation uses 0.97 fb^{-1} of muon data and 1.02 fb^{-1} of electron data.

3.2 Detector Overview

At the collision point designated B0 in the nomenclature of the Tevatron, sits the CDF detector[36, 37]. The Run II version of the detector is shown in Figure 3.2. It is a complex device that consists of many subdetectors that together help analyze the products of the colliding beams. From the interaction point outwards it has:

- a Cerenkov Luminosity Counter (CLC) to measure the instantaneous luminosity of the collisions.

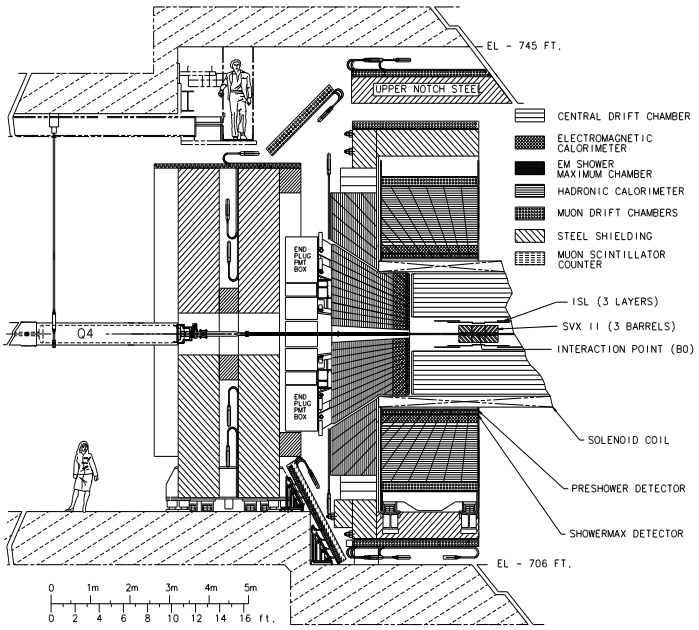

Figure 3.2: A side view of the CDF Run II detector.

- a central silicon vertex detector to provide high precision tracking of charged particles near the interaction point;
- an outer tracking chamber consisting of drift wires that is located in a 1.4 Tesla magnetic field so that the momentum and charge of tracks can be measured;
- a calorimeter to detect electromagnetic objects such as electrons and photons;
- a calorimeter to detect hadronic showers;
- muon detectors consisting of drift tubes. Muons are assumed to be the only particles which pass through the previous detectors but are visible.

Figure 3.3 is a pedagogical view of how elementary particles behave inside the detector. It serves as a guide for identifying particles. Notably, electrons have a track

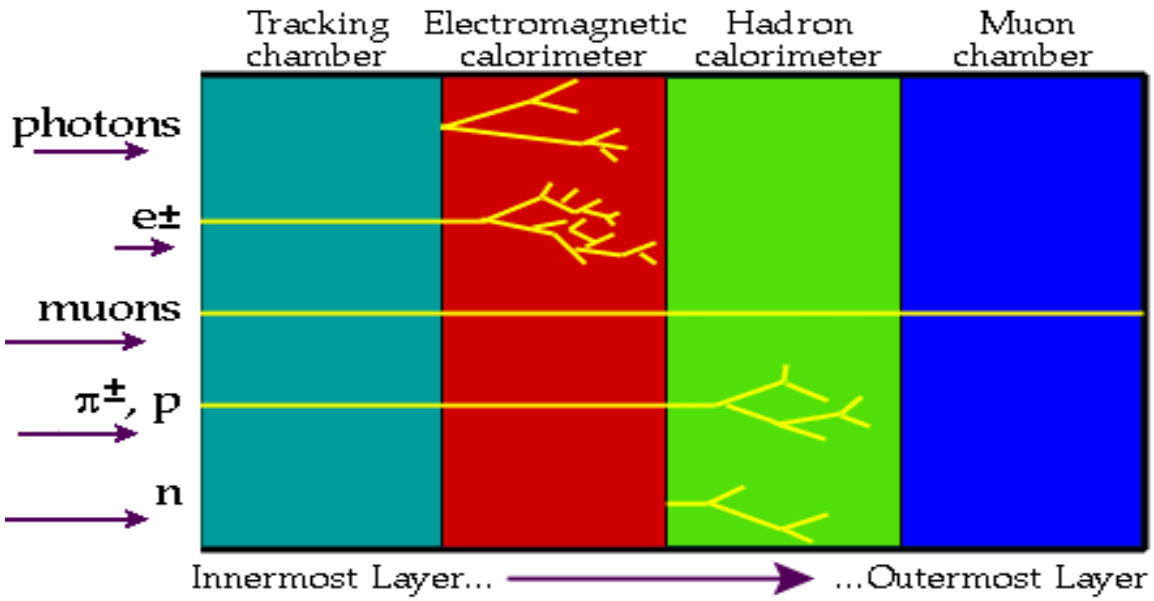

Figure 3.3: A simplistic portrayal of how particles behave within the CDF detector.

in the tracking chamber and energy deposited in the EM calorimeter, jets have energy deposited in many places but mostly in the HAD calorimeter and muons have a single track that passes through everything. The specific requirements for this analysis are given in Chapter 4.

Before proceeding, there are some key definitions relating to the CDF detector.

- θ is the polar angle relative to the proton beam direction.
- ϕ is the azimuthal angle
- $E_T \equiv E \cdot \sin\theta$ is transverse energy (i.e. perpendicular to the beam) Energy is measured in the calorimeters.
- $P_T \equiv P \cdot \sin\theta$ is transverse momentum. Momentum is measured in the tracking chambers.

- $M_{12} \equiv \boldsymbol{P_1} \cdot \boldsymbol{P_2} \equiv E_1 * E_2 - \vec{P}_1 \cdot \vec{P}_2$ - Relativistic definition of Mass
- $\eta \equiv -\ln(\tan\theta/2)$
- $\Delta R \equiv \sqrt{(\Delta\phi)^2 + (\Delta\eta)^2}$ is a measurement of the separation between two different objects.

3.2.1 Cerenkov Luminosity Counter (CLC)

The luminosity is measured by the Cerenkov Luminosity Counter (CLC). These detectors are placed in the forward and backward regions very close to the beam-line ($3.7 < |\eta| < 4.7$) and are long, conical gaseous Cerenkov counters. The counters monitor the average number of inelastic $p\bar{p}$ collisions by measuring the number of particles in each bunch crossing. Luminosity is related to the number of inelastic collisions as follows:

$$\mu \cdot f_{BC} = \sigma_{in} \cdot \mathcal{L} \tag{3.1}$$

where $\mathcal{L}$ is the instantaneous luminosity, f_{BC} is the rate of bunch crossings in the Tevatron, σ_{in} is the inelastic cross section of the beam and μ is the average number of $p\bar{p}$ interactions per bunch crossing. By measuring μ in the CLC and having a precise knowledge of f_{BC} and σ_{in}, the instantaneous luminosity is measured.

3.2.2 Silicon Tracking Systems

A precise measurement of particle momentum and location close to the collision point is essential to many analyses. This precision provides a localization of the collision as well as identification of long-lived byproducts of the collision. For a low mass Higgs analysis, precision tracking is important for the identification of the B hadron decay products from the Higgs boson.

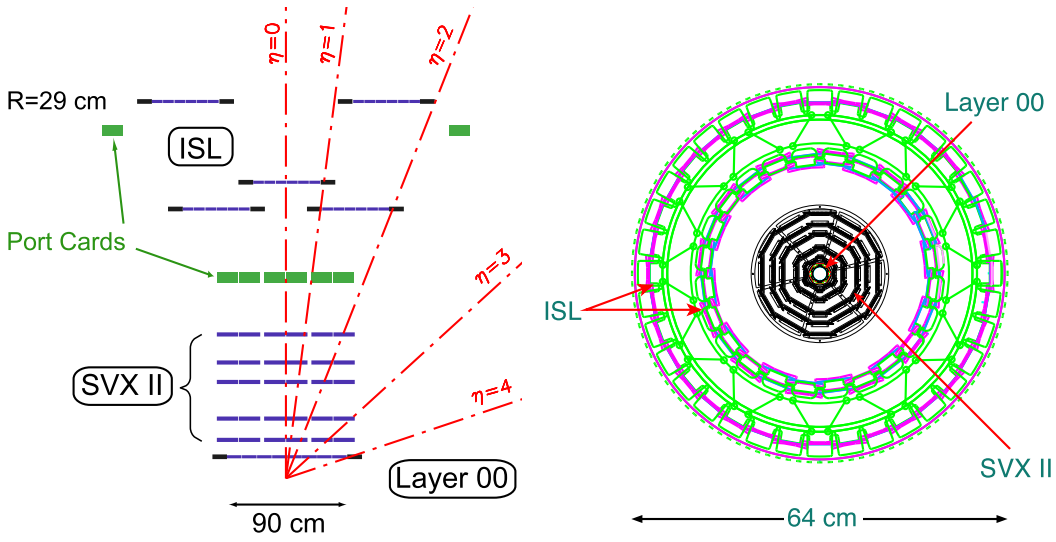

Figure 3.4: The CDF Run II silicon detectors. On the left is a side view of half of the CDF Run II silicon detectors on a scale in which the z coordinate is highly compressed. On the right is an end view.

Semiconductor detectors are commonly used close to the beam-line because they are the most precise detectors. They often work with a junction between two types of silicon material that are 'doped," by adding atoms of another element into the silicon lattice. If the doping atoms have more electrons than the silicon atoms, the silicon is called "n-doped" because there are now more electrons than holes. If the doping atoms have fewer electrons than silicon, the silicon is "p-doped." When p-doped and n-doped silicon are brought into contact, what forms is known as a pn junction. Silicon detectors consist primarily of one type of silicon (such as "p" type) with alternating strips of the oppositely doped silicon (such "n" type) applied on top of the bulk silicon.

To measure the ionized electrons from a charged particle, the entire silicon sensor must be depleted by applying a voltage across the sensor. Ionized electrons from charged particles drift through the bulk towards the strip on top, where the charge is collected. The CDF II silicon system consists of three subsystems: the Layer 00 (L00), Silicon Vertex (SVX II), and Intermediate Silicon Layers (ISL) detectors [38, 39]. Figure 3.4 shows side and end views of the silicon tracking systems.

The L00 detectors consist of a single layer of single-sided silicon wafers directly mounted on the beam pipe. The inner side of these wafers are at a radius of 1.35 cm from the nominal beam pipe and is 90 cm long. This corresponds to $|\eta| < 4$.

The SVX II detector has five layers with the innermost layer at 2.44 cm and the outer most layer at 10.6 cm. On one side of the wafers, the strips are placed in the axial direction. The other side of the wafer has the strips placed at 90° to the axial direction (for layers 1,2, and 4) or at a small stereo angle (layer 3 and 5). The length of the SVX II system is 87.0 cm. This corresponds to $|\eta| < 2.4$ for the fifth layer of the SVX II.

The final layers of the silicon system are the Intermediate Silicon Layers. It consists of either of one or two layers of silicon layers, depending on the location in the detector. This system is also double sided with one side being axial to the beam and the second being at a slight stereo angle. The complete ISL has a length of 87.5 cm. This corresponds to $|\eta| < 2$.

3.2.3 Central Outer Tracker (COT)

Outside of the silicon system is a much larger tracking chamber consisting of drift wires [40]. As charged particles travel through the gaseous environment of the drift

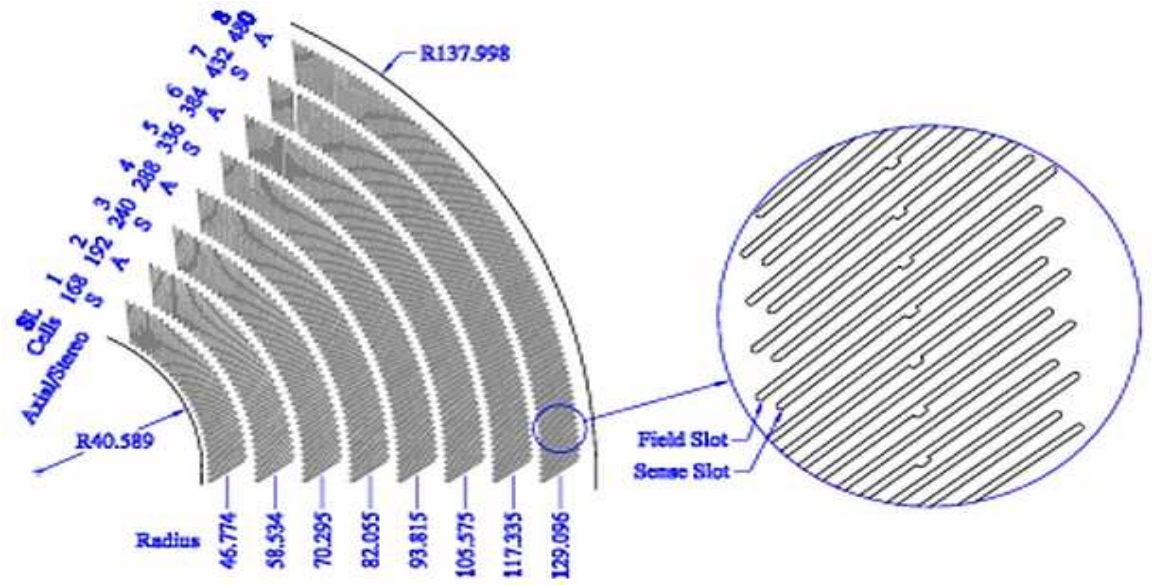

Figure 3.5: Side view of the COT detector. The COT is made of alternating super-layers of axial and stereo wires.

chamber, a path of ions and electrons are left behind. These ionization electrons are attracted to the voltage on the sense wire and drift towards them causing a pulse of current. As a result, a series of hits are generated with each hit corresponding to a specific r and ϕ position in the chamber. By measuring and fitting the tracks to a helix, an accurate measurement is made of the momentum of the charged particle.

The drift wire chamber is filled with a gas approximately 50% Argon and 50% ethane. The drift wires are organized into 8 super-layers, each layer consisting of 12 sense wires and 13 potential wires that alternate. This pattern can be seen in Figure 3.5. A track that passes all eight layers has 96 hits as it passes through the chamber. The even numbered layers (assuming the first layer is layer 1) are axial to the beam line and the odd numbered layers are at a stereo angle of $\pm 2^\circ$ from the axial direction.

The innermost layer is 43 cm from the beam line and the outermost layer is 133 cm. The chamber is 310 cm long. Tracks with $|\eta| < 1$ pass through all eight super layers. Tracks with $|\eta| < 1.3$ pass through at least 4 super layers. The resolution, δP_T, of tracks as low as 400 MeV/c in the COT is designed to be $\delta P_T / P_T^2 \leq 0.1\%\ GeV/c$.

3.2.4 Solenoid

The tracking system, the silicon detectors and the COT, sit within a 1.4 T magnetic field. The field is produced by a superconducting solenoid made of an aluminum-stabilized Nb-Ti conductor. The field is in the direction of the beam-line, bending charged particle as they travel through the tracking system. From the direction of the curve, it is possible to measure the momentum and charge of the particle.

3.2.5 Calorimeters

Outside the solenoidal magnet sit the calorimeter detectors. These detectors are used to measure the energies of electrons, photons, and hadronic jets. Physically, the system is divided into a central region ($|\eta| < 1.1$) [41] and the plug region ($|\eta| < 3.6$) [42, 43]. The calorimeters are subdivided into electromagnetic calorimeters and hadronic calorimeters. The former absorbs most of the energy from electrons and photons while the latter detect parts of hadronic jets that are not fully absorbed in the EM calorimeter.

The calorimeters contain alternating layers of absorbing materials and scintillators. Particles passing through the detectors interact with the absorber and create a "shower" of particles. The particles illuminate the material in the scintillating layers and are collected in photomultiplier tubes. The electromagnetic and hadronic calorimeters are lead-scintillator and iron-scintillator sampling devices, respectively.

in the central region, the towers are segmented 15° in azimuth and 0.1 in η. In the plug (or forward) region ($1.1 < |\eta| < 3.6$), the segmentation is towers of 7.5° for $\eta < 2.11$ and 15° for $|\eta| > 2.11$. The electromagnetic calorimeters are instrumented with proportional (CES/PES) and scintillating strip detectors that measure the transverse profile of electromagnetic showers at a depth of six radiation lengths, corresponding to the expected shower maximum. The CES has a resolution of roughly 0.2 cm. The measured energy resolution for electrons in the electromagnetic calorimeters is $14\%/\sqrt{E_T} \oplus 2\%$ in the central and $16\%\sqrt{E_T} \oplus 1\%$ in the forward. The measured single-particle (pion) energy resolution in the hadronic calorimeters is $75\%/\sqrt{E_T}$ for the central and $80\%/\sqrt{E_T} \oplus 5\%$ for the forward detector.

3.2.6 Muon Detectors

The muon detectors are made by single wire drift chambers four cells deep. They are located on the very outside of the detector because muons ($P_T \gtrsim 1.5\ GeV/c$) should pass through the calorimeters. Figure 3.6 shows an overview of the muon coverage. The coverage of the muon chambers extends to $|\eta| < 1.5$, with triggers that perform at efficiency > 90% for the region $|\eta| < 1$. There are four different muon detectors. The central muon detector (CMU) lies just outside the hadronic calorimeter. The central muon upgrade (CMP) adds an additional layer of coverage for the CMU detectors. The central muon extension (CMX) covers the region $0.6 < |\eta| < 1.1$, and contains eight layers of drift tubes, with the average muon passing through six. A fourth system is the Intermediate Muon chambers (IMU), which sit outside the plug calorimeters.

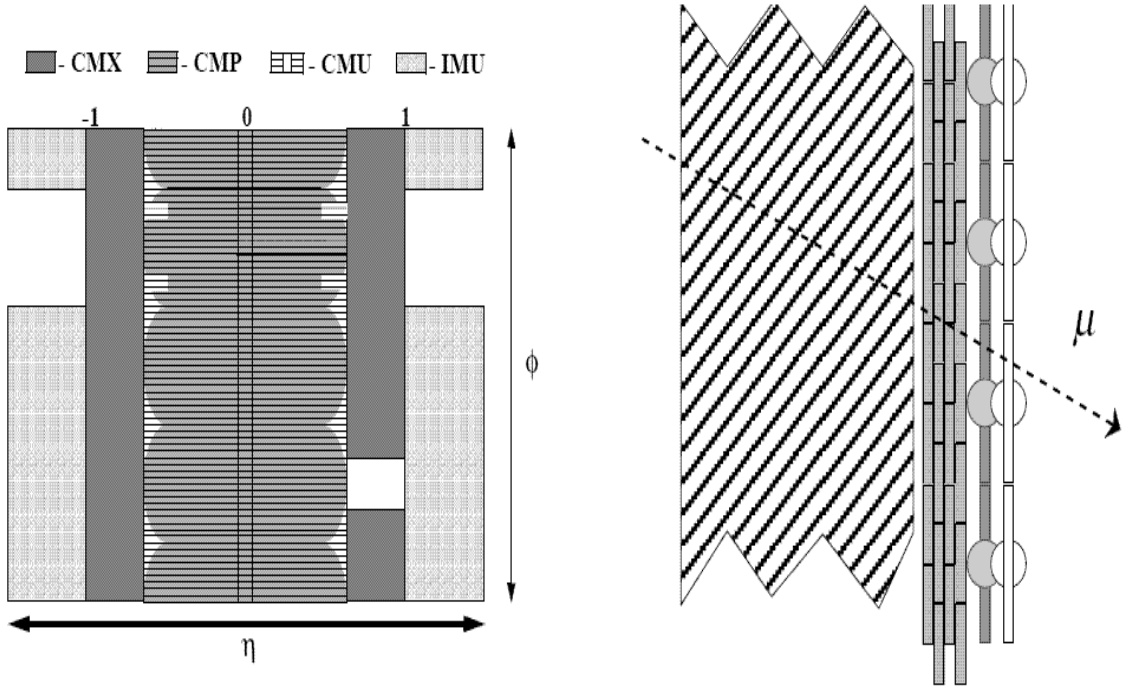

Figure 3.6: Details of the CDF muon detectors. Coverage of the muon detectors (right). The CMU and CMP detectors cover areas to $|\eta| < 0.7$, CMX covers $0.7 < |\eta| < 1.1$ and the IMU covers $1.1 < |\eta| < 1.5$. There are gaps in the detectors as shown by empty space. (left) The muon travels through the calorimeter with depositing a minimal amount of energy. Most other particles are absorbed in the calorimeter.

3.3 Usage of the CDF Detector

While each part of the CDF detector is unique and can be used individually, its true strength comes when all the components are used together. Perhaps the most important task a detector needs to accomplish is to store interesting events so that they are available for analysis. However, given the rate of proton-antiproton crossings, this is not a simple task. Section 3.3.1 explains the need for a trigger system at a high-energy detector. Leptons are identified using the tracking chamber along with either the EM calorimeters for electrons or the muon chambers for muons. This is discussed in Section 3.3.2. The modeling of jets is discussed in Section 3.3.3. To identify b quarks, this analysis searches for displaced vertices. The b-tagging algorithm used in this analysis is described in Section 3.3.5. In Section 3.3.4, I explain how CDF tries to estimate the neutrino content of an event.

3.3.1 Event Triggers

Higher luminosity creates challenges for collecting data. There is a finite rate of data that can be collected and recorded to disk to be analyzed later, meaning that at a high rates some data must be discarded. The detector must have a trigger system to ensure that "interesting" events get recorded for later analysis. CDF uses a three level "triggering" system. Each layer searches for interesting properties in a collision based on stricter and stricter criteria. If a set of criteria is met, the event is then processed by the next level. This trigger culls collisions that can occur at an input rate 2.5 MHz down to a recording rate of $\leq$ 50 Hz. If the stream of data is not reduced, the computing power that records data to tape would be overtaxed. This results in new events being missed while earlier events are still being processed. These

events are lost forever, an undesirable occurrence especially for rare events such as those containing a Higgs boson.

An example and a vital cog of the triggering system is the creation of "XFT tracks," by the eXtremely Fast Tracker system[44]. Since the trigger must make a decision to keep an event in a short time span, tracks must be reconstructed quickly for use in the trigger decision.

The XFT system starts by converting the COT axial wire hit data into two timing windows, prompt and delay. This information is then sent to Finder Boards, which try to collect these wire hit data into patterns of hits in a given axial super-layer. Valid patterns are characterized by position and slope called pixels. These "pixels" are then transmitted to the Linker system, which tries to reconstruct the four axial layers' data into a single track. These tracks are made by comparing the pixels to a predefined list of track pattens. The tracks at this point are only two dimensional. A recent upgrade created a parallel path for the stereo layers of the COT. With the upgrade, the stereo information is used to confirm the axial tracks and reduces the chance of making false tracks at high luminosity. For low instantaneous luminosity data taking, using only the four axial layers, the XFT has an efficiency of $96.7 \pm 0.1\%$ for charge tracks of momenta greater than 1.5 GeV/c. At higher luminosity, requiring the stereo confirmation reduces the efficiency by 4%.

The XFT tracks are matched with other detector systems, such as muon chambers and EM calorimeters to assist with the trigger decision at the first level of the trigger. Track reconstruction with the XFT is a critical part of the trigger system. Identifying these tracks is essential to collecting leptons in the trigger. Without it very little high P_T physics would be accomplished, including the Higgs boson search.

3.3.2 Lepton Identification

For the purposes of this analysis we focused on Z decays to electrons and muons decay products only. Charged leptons are fairly clean objects in high energy physics. They are observable unlike neutrinos, and they do not produce a large shower of particles like gluons and quarks. Muons and electrons must be identified as part of the online trigger and in the final offline analysis. Below is a summary of the quantities used to select pure samples of leptons.

Electron Quantities

- E_T - The amount of energy deposited in the calorimeters. Electron objects are formed from energy clusters of neighboring calorimeter towers. An electron cluster is made from an EM seed tower and at most one additional tower that is adjacent to it in η_{det} and with the same ϕ wedge. The seed tower must have $E_T > 2\ GeV$ and a reconstructed COT track which extrapolates to that tower.

- P_T - The momentum of the electron is measured in the COT tracking detector.

- **Had/EM** - This ratio is the ratio of energy deposited into the hadronic calorimeters divided by the energy in the electromagnetic calorimeters. Electrons deposit most of their energy into the EM calorimeters, therefore an electron should have a low Had/EM.

- L_{shr} - This quantifies the agreement between the lateral shower profile of the electron candidate to what is expected from test beam data.

- $|\Delta x|$ and $|\Delta z|$ - These measure the separation between the extrapolated COT track position and the shower position in the CES in the $r - \phi$ and $r - z$

planes, respectively. True electrons should have good agreement between the extrapolated track position and the CES shower.

- **E/P** - This measures the ratio of the energy deposited in the calorimeter to the measured momentum. Ideally, this number should be near unity. However, electrons, especially high energy ones, may emit bremsstrahlung photon energy.

- **Isolation** - Defined as the ratio of energy deposited outside the center of a electron cluster to the total energy within a cone of $\Delta R = 0.4$. Electrons from a Z boson are isolated from jets and other leptons, so this quantity should be small.

- χ^2_{strip} - This is a comparison of the CES shower profile in the $r - z$ view to the profile extracted from electron test-beam data.

In addition, there are also quality requirements. A fiducial cut is used to restrict electrons to well instrumented regions of the calorimeter. This excludes sections that are left uninstrumented for mechanical reasons. We require that the primary vertex is within 60 cm of the center of the detector. Another common requirement is that multiple leptons come from the same collision point. A requirement is made that there are multiple hits in the COT super layers in order for a track to be considered. In addition, there is a minimum requirement on the number of COT super layers with used to measure the track.

Muon Quantities

Muons behave differently in the detector. A muon will have a single track in the COT. The muons that pass through the calorimeter deposit energy as a minimum ionizing particle. Finally, a muon will leave hits in the muon chambers.

- P_T - The momentum is measured in the COT tracking detector.
- $|\Delta x|$ and $|\Delta z|$ - These quantities measure the separation between the extrapolated COT track position to the appropriate muon chambers in the $r - \phi$ and $r - z$ plane respectively.
- **EM Energy** and **HAD Energy** - A requirement that the energy deposited in the calorimeters is consistent with a minimal ionizing object.
- **Isolation** - The main COT track from a muon is required to be relatively isolated from other tracks within a cone of $\Delta R < 0.4$. Muons from a Z boson are isolated from jets and other leptons.

The same quality cuts that are applied to electron tracks are also applied to muon tracks. The quantity ρ is the radius at which a track exits the COT. A cut of $\rho > 140$ cm is made to ensure that the track passed through four axial layers, and therefore can create a XFT track. In order to remove possible cosmic rays, muons track are required to have small impact parameters, d_0.

These quantities are used to select samples of electrons and muons. The specific cuts are given in Chapter 4.

3.3.3 Jet Modeling

Quarks and gluons emerging from a collision normally manifest themselves as a spray, or a jet, of particles. As mentioned earlier, quarks are always found bound into hadrons. When a quark is created by itself, the strength of the QCD interaction pulls a quark from the vacuum. However, a new quark is created and the the process repeats. Therefore, a quark creates a shower of particles in its wake. This spread of energy makes the precise measurement of the initial quark's (or gluon's) energy difficult. In general, the measurement of objects such as photons and charged leptons is more precise because they do not appear as a large shower of hadronic objects.

To identify high energy jets, an iterative algorithm called JetClu is used [45]. First a seed tower with an E_T of at least 3 GeV in the calorimeter is identified. Adjacent towers with an $E_T > 1$ GeV are added to the seed tower. After this is done, the center of the jet is calculated, and the process is restarted until a stable collection of calorimeter towers is found. Overlapping jets are merged if they share more than 50% of their energy. There are several different versions of this algorithm that depend on the width of the towers that are clustered together.

The jet's raw energy is corrected for a variety of effects [46]. These correction are based on test beam data and $in-situ$ data. The jets are corrected to take into account:

- Absolute Jet Energy Scale: This correction maps the total calorimeter jet E_T to the total E_T of the hadron-level jet. The hadron-level jet consists of the particles within the jet cone. The key is to accurately describe the calorimeter response to single particles (pions, protons, neutrons, etc.)

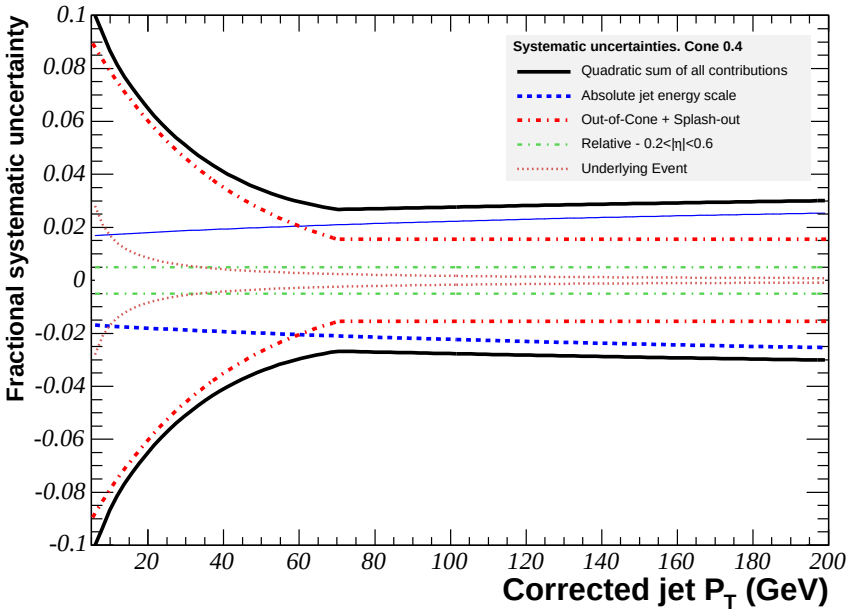

Figure 3.7: CDF jet energy uncertainties

- η dependent correction: This arises because of different physical features of the CDF detector (i.e. separation of central and plug calorimeters and a gap at $\eta = 0$.)

- Multiple $p\bar{p}$ interactions - at higher luminosities: At higher luminosities more than one collision can occur per bunch crossing, which affects the measurement of jet energies.

The relative jet energy uncertainty is shown in Figure 3.7.

3.3.4 Missing Transverse Energy Measurement

Many analyses in high energy physics depend on the neutrino content in each event. Since neutrinos do not have any charge they only interact via the weak force

and therefore are very unlikely to leave any signal in the CDF detector. Indirect measurements are necessary to find the neutrino momenta. Because the transverse momentum of the initial $p\overline{p}$ collision is zero, the final transverse momentum after the collision should also be equal to zero by conservation laws. Therefore, any transverse momentum imbalance in the CDF detector is attributed to neutrinos. The missing E_T, shortened to $\not\!\!E_T$ or MET, is defined:

$$\not\!\!E_T \equiv -(\sum_{i=calorimeters} E_T^i \hat{n}_i + \sum_{i=muons} \vec{P_T}^{\,i}) \tag{3.2}$$

where $\hat{n}_i$ is the radial unit vector pointing from the interaction point to the energy deposition in the calorimeter tower.

Although the $\ell^+\ell^- b\overline{b}$ channel does not have any neutrinos in the final state, the $\not\!\!E_T$ is significant in this analysis. First, some backgrounds, notably $t\bar{t}$, have a large neutrino content in their final state. Also, b jets may contain decays that have neutrinos. In Section 5.2, I show how the $\not\!\!E_T$ is used to help correct jet energies.

3.3.5 SecVtx Algorithm

It is possible to separate jets caused by b quarks from those caused by other quarks and gluons. The b quark decays through the weak force, therefore its lifetime is long enough for it to travel a few millimeters from the primary vertex. Most b-tagging algorithms take advantage of this decay length and the precise measuring capabilities of the SVX detector (Section 3.2.2). With the precise tracking at the center of the detector, tracks are found to point towards this secondary vertex.

To find a secondary vertex in an event, one must first find the primary vertex of the event. The primary vertex is determined by measuring the intersection of tracks in the beam line. Only tracks that are within 1 cm of the initial vertex calculation

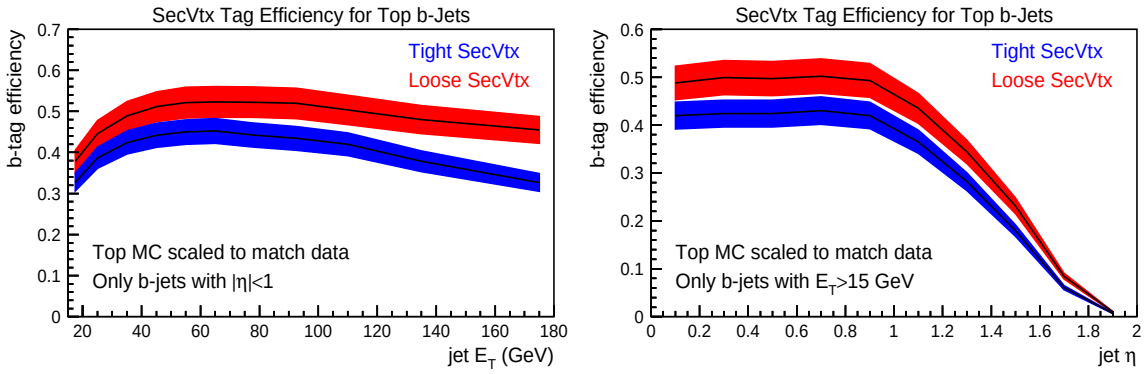

Figure 3.8: SecVtx efficiency. The efficiency of the SecVtx algorithm per b jet as function of E_T (left) and η (right).

are used to calculate the precise position. If more than one vertex in the event is found (which is possible especially in high instantaneous luminosity environments), the convergence of leptons is used for the primary vertex. The precision for the fitted transverse vertex position ranges from 10-32 μm depending upon the number of reconstructed tracks and the topology of the event.

Next, for each calorimeter jet. tracks within a cone of 0.4 are used. The tracks must pass criteria based on their p_T, the quality and quantity of hits in the SVX that make the tack, and the overall fit quality of the final track. A jet can only be tagged if it has at least two tracks which pass these criteria. The efficiency of SecVtx per b jet is shown in Figure 3.8.

Using the tracks associated with a jet, the algorithm attempts to find a vertex separated from the primary. If a secondary vertex that is significantly displaced from the primary vertex is found, the jet is tagged. Secondary vertices that are in the direction of the jet are said to be positively tagged. Those vertices that are displaced away from the jet direction are negatively tagged. Negatively tagged jets are used

to estimate the amount of light flavor quark jets (u, d, s) that are "mistagged" as being b-quark jets. This "mistagging" occurs in about 1% of jets and is due mostly to mismeasurement of tracks in the SVX. This estimation is described in Chapter 4.

CHAPTER 4

EVENT SELECTION

While the $ZH \rightarrow \ell^+\ell^- b\overline{b}$ channel might have the lowest cross section and branching ratio of any of the SM Higgs searches, it has an advantage in that it has a relatively small background. The small background is caused primarily because $p\overline{p}$ collisions have a much smaller rate of producing two leptons. Also, unlike the $\ell\nu b\overline{b}$ or the $\nu\nu b\overline{b}$ channels, all the final products are directly measurable. To select events in the $\ell^+\ell^- b\overline{b}$ channel, one needs to find two leptons that can be reconstructed as a Z boson and at least two jets that can be the products of a Higgs boson decay. In addition, at least one of these jets must be identified as being from a B-hadron. The details of selecting events are given in Section 4.1. The number of ZH signal events expected is described in Section 4.2. Section 4.3 describes the background events that mimic the $ZH \rightarrow \ell^+\ell^- b\overline{b}$ channel. Tables 4.11 and 4.12 enumerate the total expected event counts in 1 fb^{-1} of data.

4.1 Event Criteria

An overview of the event selection requirements is found in Table 4.1, including a reference to where those cuts are discussed. The identification of events is dependent on the individual detectors described in Chapter 3.

Selection	Section
A central lepton trigger	4.1.1
One high E_T central lepton with "tight" requirements	4.1.2
A second high E_T lepton of the same flavor	4.1.2
Δz_0 of leptons < 4 cm (muon events only)	4.1.2
Opposite charge muons or central-central electrons	4.1.2
Z boson mass window 76 GeV/c^2 - 106 GeV/c^2	4.1.2
2 or more jets with $E_T > 15$ GeV and $\|\eta\| < 2$	4.1.3
1 or more jets with $E_T > 25$ GeV	4.1.3
Either 2 "loose" b-tags or 1 "tight" b-tag	4.1.4

Table 4.1: Summary of event selection and subsections where details are covered.

4.1.1 Event Triggering

During $p\bar{p}$ collisions, the colliding partons usually interact through the strong force. To produce leptons, partons must interact through the electroweak force and therefore the process will have a much smaller cross section. Therefore, it is beneficial to look for leptons as a trigger object. For this analysis, the standard CDF central high P_T lepton triggers are used [47]. These are summarized in Tables 4.2 and 4.3.

The central electron triggers first look for energy mostly deposited in an EM tower, and with an XFT track present in the event. At Level 2, an algorithm takes an EM tower with $E_T > 8\ GeV$ and adds nearby EM towers. To satisfy the trigger, the combined towers must have $E_T > 16\ GeV$. At Level 3, a track with $P_T > 9\ GeV/c$ is required to point at the EM cluster with a requirement of $\Delta z \leq 2$ cm. The minimum E_T requirement is 18 GeV. The electron trigger efficiency was measured using $W^{\pm} \rightarrow e\nu$ data using an event trigger that does not require a track. It has

Trigger	CEN. Elec
Level 1	Cen. Cal. $E_T \geq 8\ GeV$ XFT $P_T \geq 8.34\ GeV/c$ Had/EM < 0.125
Level 2	L2 $E_T \geq 16\ GeV$ L2 Had/EM ≤ 0.125 $\eta < 1.317$
Level 3	Cen. $E_T > 18\ GeV$ Cen. Had/EM < 0.125 $L_{shr} \leq 0.4$ Cen $\Delta Z \leq 2$ Track $P_T > 9\ GeV/c$
Efficiency	95.8%

Table 4.2: Central electron trigger path.

Trigger	CMUP	CMX
Level 1	CMU stub $P_T \geq 6\ GeV/c$ XFT $P_T \geq 4.09\ GeV/c$ CMP Stub	CMX stub $P_T \geq 6\ GeV/c$ XFT $P_T \geq 8.34\ GeV/c$
Level 2	XFT $P_T \geq 14.77\ GeV/c$	XFT $P_T \geq 14.77\ GeV/c$
Level 3	Track $P_T \geq 18.0\ GeV/c$ CMP $\Delta X < 20$ CMU $\Delta X < 10$	Track $P_T \geq 18.0\ GeV/c$ CMX $\Delta X < 10$
Efficiency	92%	89%

Table 4.3: Central muon trigger paths.

been measured to be 95.8% efficient for central electrons above 20 GeV that meet the triggering criteria. Between 18 GeV and 20 GeV, the trigger efficiency is not constant and experiences a turn-on effect.

For muons, there are two types of triggers, CMUP and CMX, named after sections of the muon detector. A CMUP trigger requires aligned muon hits in the CMU and CMP chambers while the CMX trigger only requires hits in the CMX trigger. At Level 1, a XFT track is required to project towards the CMU or the CMX muon detectors. The muon trigger efficiency was measured with $Z \rightarrow \mu^+\mu^-$ data. To determine the efficiency, the rate in which both muon legs triggered the event is measured. The CMUP trigger is 92% efficent. The CMX trigger is 89% efficient for most of the system. These efficiency numbers are for muons fiducial to the trigger detectors.

For $ZH \rightarrow \ell^+\ell^- b\bar{b}$ events, not all the leptons are triggerable, depending E_T, η, and ϕ of the lepton. As Figure 3.6 shows, there are regions that are uninstrumented and are unable to trigger the event. When the Z decays to electrons, 60% of ZH events are triggered by the CEM trigger. The two muon triggers, CMUP and CMX, combine to trigger 50% of all $ZH \rightarrow \mu^+\mu^- b\bar{b}$ events. After the quick decision-making process of the trigger is completed, the passing data is written to tape for analysis.

4.1.2 Lepton Selection

The offline lepton selection we use is looser than the standard CDF selection [47, 48] to gain as much signal acceptance as possible. The non-Z backgrounds are very small and maximizing the acceptance is one of the most critical issues for the Higgs search. The lepton selection cuts are given in Tables 4.4 and 4.5 for electrons and in Tables 4.6 and 4.7 for muons[47]. The cuts here refer back to the definitions in

Section 3.3.2. One "tight" lepton is required, which should pass the high P_T lepton triggers, and a separate same-flavor lepton is required with "loose" lepton cuts.

To increase the purity of real Z bosons that pass the lepton selection, a few general cuts are made. The dilepton mass is required to be 76 $GeV/c^2 \leq M_{\ell\ell} \leq 106$ GeV/c^2. This requirement is 90% efficient for $ZH \rightarrow \ell^+\ell^- b\overline{b}$ events. Where two COT tracks are available, we require that the two leptons have opposite charge. Also, leptons are required to be from the same primary vertex. These last two requirements are nearly 100% efficient for real Z bosons but reduce the background for non-Z events.

As a cross check of the lepton selection, we calculate a few well known properties of the Z boson. The $\sigma(Z) \cdot BR(Z \rightarrow e^+e^-)$ we measure is $265 \pm 1(stat.) \pm 18(sys.)$. For muons, we measure $\sigma(Z) \cdot BR(Z \rightarrow \mu^+\mu^-) = 265 \pm 1(stat.) \pm 18(sys.)$. These measurements are consistent with other CDF measurements and theoretical predictions. The Z boson mass we obtain is 90.8 GeV/c^2 for electrons and 90.7 GeV/c^2 for muons. These measurements are consistent with current measurements. After identifying an event with a Z boson that decays leptonically, the search is then focused on the other objects in the event.

4.1.3 Jet Selection

In Section 2.3, it was shown that a low-mass Higgs boson decays to a $b\bar{b}$ pair the majority of the time. The b quarks hadronize into jets and are measured in the calorimeter (Section 3.2.5). Also, since the Higgs boson should have a relatively large mass, the jets produced by its b-quark daughters have high E_T. Figure 4.1 (top) shows the E_T distibution for the higher-energy and lower-energy b quarks. One quark nearly always has an $E_T > 25$ GeV. We also see that the 15 GeV cut on E_T will also

Tight Electron Selection
$E_T > 18$ GeV
$P_T > 9\ GeV/c$
Had/Em $< 0.055 + 0.00045 \cdot$E
$E/P < 2.5 + 0.015 \cdot E_T$
$\lvert Z_{vertex} \rvert < 60$ cm
In central region ($\lvert\eta\rvert < 1$)
Isolation $\cdot E_T^{raw}/E_T^{corr} < 0.1$
$L_{shr} < 0.2$
-3.0 $<$ Q $\cdot \lvert\Delta x\rvert < 1.5$
$\chi^2_{strip} < 25.0$
$\lvert Z_{electron} - Z_{vertex} \rvert < 3$ cm
2 stereo and 2 axial super-layer segments

Table 4.4: Tight electron requirements. At least one electron in e-e events must satisfy these requirements.

Loose Electron Selection
$E_T > 10$ GeV Central or $E_T > 18$ GeV Plug
Had/Em $< 0.055 + 0.00045 \cdot$E
Isolation $\cdot E_T^{raw}/E_T^{corr} < 0.1$
$P_T > 5\ GeV/c$ (for Central region)
$\lvert Z_{vertex} \rvert < 60$ cm
Is Fiducial

Table 4.5: Loose electron requirements. The second electron in e-e events is subject to looser requirements. Note that the second electron may be in the plug calorimeter ($1.1 < \lvert\eta\rvert < 2.2$).

Tight Muon Selection
$P_T > 20\ GeV/c$
Had Energy < 6 GeV
Em Energy < 2 GeV
≥ 3 axial and ≥ 3 stereo segments
Isolation < 0.1
Impact parameter $d_0 < 0.2$ w/Silicon hits (0.02 w/out)
Tight CMUP requirements
$\lvert\Delta x\rvert_{CMU} < 3.0$ cm
$\lvert\Delta x\rvert_{CMP} < 5.0$ cm
Tight CMX requirements
CMX $\rho > 140$ cm (Tracks must pass through all COT layers)
$\lvert\Delta x\rvert_{CMX} < 6.0$ cm

Table 4.6: Tight muon requirements. At least one muon must meet these requirements for dimuon events.

Loose Muon Selection Paths	
$10\ GeV/c < P_T \leq 20\ GeV/c$	$P_T > 20\ GeV/c$
Had Energy < 6 GeV	Had Energy < 12 GeV
Em Energy < 2 GeV	Em Energy < 4 GeV
Isolation < 0.1	Isolation < 0.4
Impact parameter $d_0 < 0.2$ w/Silicon hits (0.02 w/out)	
≥ 1 COT segments	≥ 1 COT segments

Table 4.7: Loose muon requirements. The second muon may pass these looser requirements. There are two available paths for the "loose" muon. If the $P_T > 20\ GeV/c$, then other selection cuts are relaxed. Otherwise, the $10\ GeV/c\ < P_T \leq 20\ GeV/c$ faces similar requirements to the "tight" muon. However, these muons are not required to have any muon detector stubs.

accept most Higgs pairs. The Higgs is also produced in the central region of the CDF calorimeter. The η distribution for the b quarks is shown in Figure 4.1 (bottom). Both b quarks are shown to be mostly within the region $|\eta| < 2$.

Using a requirement for the highest energy jet to have an $E_T > 25\ GeV$ and all other jets to have $E_T > 15\ GeV$ was shown to reduce the background while maintaining signal. A minimum of two measured jets is necessary in order to find a mass. However, no maximum number is required. Higgs events may have more jets because of either initial/final state radiation or multiple interactions in an event. Jets are required to have an $|\eta_{detector}| < 2$. In this range the silicon detector can be used to identify b-quark jets.

4.1.4 "b-tagging"

Topologically speaking, the Higgs boson is hard to separate from other physical processes. However, one thing that is unique to the Higgs boson is its decay rate to b quarks. Therefore, our final examination of the dataset uses b-tagging to best separate the Higgs from other objects. The "SecVtx" algorithm was used [49]. The b-tagged events are placed into two categories. The first has two "loose" b-tagged jets in the event. If two b-tagged jets are not found in the event, the remainder are required to have one "tight" b-tagged jet. These two tagging categories are analyzed separately since the signal to background ratio is different.

b-tags are found in approximately 60% of ZH events with 2 or more jets. One third of these events are within the two tag channel and two thirds in the one tag only region. The backgrounds are reduced by factor of 250 and 25 in the two tag and

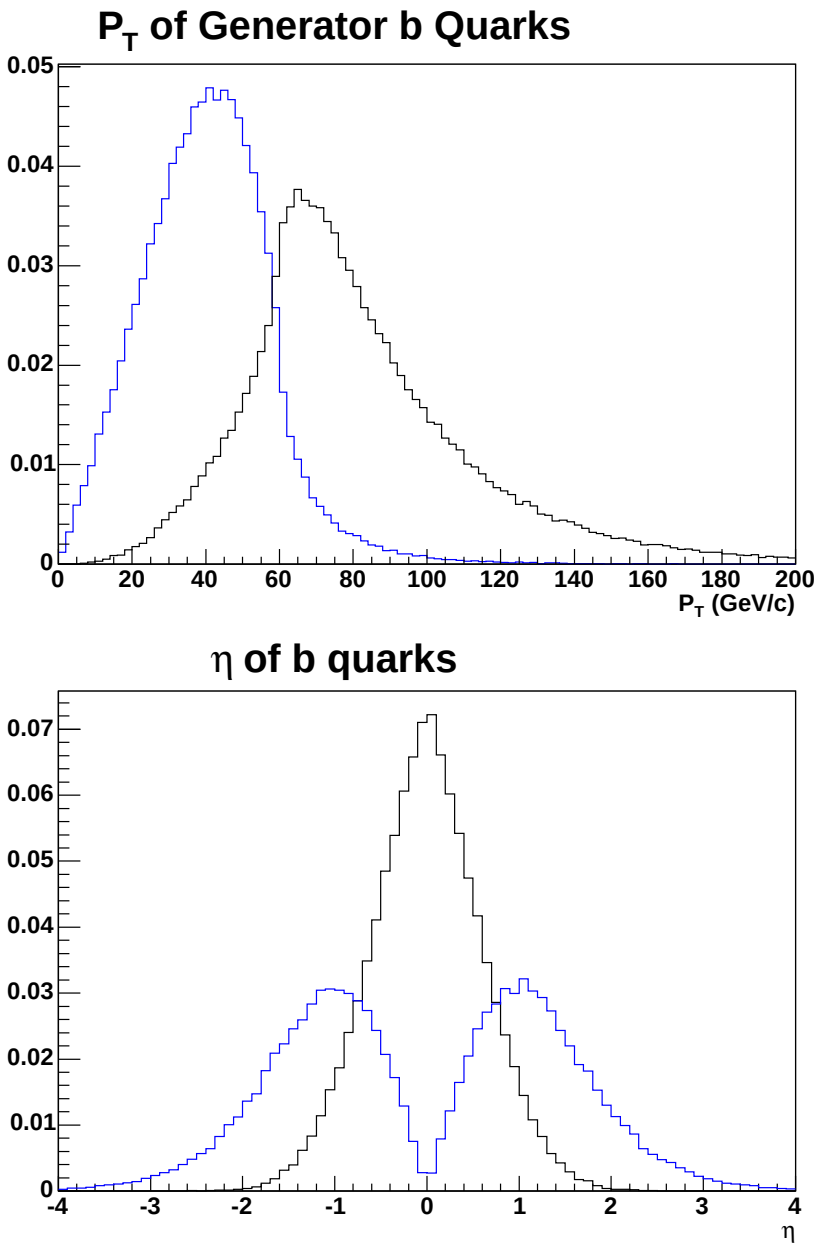

Figure 4.1: Higgs boson generator b quark kinematics. On top is shown the P_T of the b quarks from Higgs boson decay. On bottom is shown the η distributions for the b quarks.

one tag region, respectively. A great deal of the reduction in the two tags comes from reducing the number of misidentified b jets, as is explained in Section 4.3.2.

4.2 Signal Acceptance

The efficiency of the selection cuts are modeled in Pythia [50] generated Monte Carlo. The decays are simulated through the CDF detector environment using a GEANT-based simulation [51]. Table 4.8 shows the efficiencies of the event cuts for a Higgs mass of 120 GeV/c^2 for electrons and muons separately at different stages of the selection. The cross section and branching ratios have been calculated elsewhere [52, 53]. Tables 4.9 and 4.10 shows the expected events for various Higgs masses. The ratios shown are measured relative to all $ZH \rightarrow \ell^+\ell^- b\overline{b}$ events, including $Z \rightarrow \tau^+\tau^-$, that can contribute to our signal.

To account for any differences in the efficiencies between the Monte Carlo and measured data, we use scale factors determined from larger datasets [54]. This includes scale factors for the electron and muon identification, the b-tagging efficiency, the trigger efficiencies and the z-vertex requirement.

4.3 Backgrounds

The Higgs signature of two leptons forming a Z boson and two or more jets tagged as b jets is not unique. Other physics processes share this pattern, and are produced at a greater rate. These are called backgrounds. The backgrounds consists of three major components, given in relative size:

1. Backgrounds with two genuine leptons and a genuine b or c-jet are estimated using Monte Carlo samples.

Acceptance of $ZH \to l^+l^-b\bar{b}$ events	e^+e^-	$\mu^+\mu^-$	Total
Tight Lepton found	21%	15%	37%
Second Lepton found	13%	11%	23%
Z cut	11%	9.8%	21%
$\geq$2 Jets	9.4%	8.0%	17%
+ B-tagged	5.3%	4.5%	9.7%
2 loose B tags	1.9%	1.7%	3.6%
1 tight B-tagged	3.3%	2.8%	6.1%
With branching ratios for $Z \to l^+l^-$ and $H \to b\bar{b}$			
A_{ZH}	0.37%	0.32%	0.69%

Table 4.8: Acceptance of $ZH \to \ell^+\ell^-b\bar{b}$ after event selection cuts. Acceptance of $M_H = 120\ GeV/c^2$ and Z is forced to decay to charged leptons (including τs) after the selection cuts. The last line shows the acceptance of all ZH events assuming a branching ratio of $Z \to l^+l^-$=10.1% and a $BR(H \to b\bar{b}) = 67\%$ for m_H=120 GeV/c^2

Higgs Mass (GeV/c^2)	σ_{ZH} (pb)	Branching Ratio ($H \to b\bar{b}$)	$\mu^+\mu^-$ events	e^+e^- events	Total events
100	0.17	0.81	0.19	0.23	0.41
110	0.12	0.77	0.14	0.18	0.32
115	0.11	0.73	0.13	0.15	0.28
120	0.09	0.68	0.10	0.13	0.23
130	0.07	0.53	0.066	0.083	0.15
140	0.05	0.34	0.037	0.046	0.085
150	0.04	0.18	0.015	0.017	0.032

Table 4.9: Expected $ZH \to l^+l^-b\bar{b}$ events after double tag selections for a range of Higgs masses.

Higgs Mass (GeV/c^2)	σ_{ZH} (pb)	Branching Ratio ($H \to b\bar{b}$)	$\mu^+\mu^-$ events	e^+e^- events	Total events
100	0.17	0.81	0.39	0.49	0.87
110	0.12	0.77	0.29	0.36	0.65
115	0.11	0.73	0.25	0.31	0.56
120	0.09	0.68	0.20	0.25	0.45
130	0.07	0.53	0.13	0.16	0.27
140	0.05	0.34	0.066	0.084	0.15
150	0.04	0.18	0.026	0.032	0.058

Table 4.10: Expected $ZH \to l^+l^-b\bar{b}$ events after single tag (not including double tag) selection for a range of Higgs masses.

2. Backgrounds with only light flavor jets which were tagged as b jets. We estimate this contribution by a function of the pretagged data. Details are given in Section 4.3.2.

3. Backgrounds with fake electrons are estimated using lepton fake rates described in Section 4.3.3.

4.3.1 Monte Carlo Modeled Backgrounds

Most of our background can be simulated using Monte Carlo generators. These backgrounds which consist of two real leptons and either b or c-jets are further divided into:

1. A real Z boson produced with either b or c quarks.

2. $t\bar{t}$ events with two same-flavor leptons where the dilepton mass falls within the Z mass window.

3. Diboson events mostly consisting of either $ZZ \to \ell^+\ell^-b\overline{b}$ or $ZW \to \ell^+\ell^-cs$.

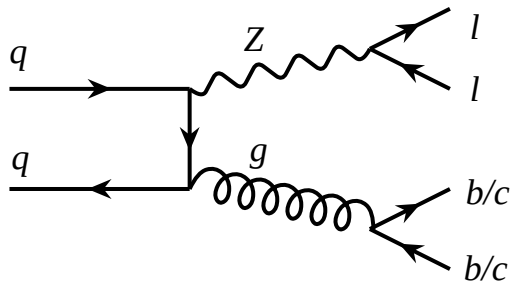

Figure 4.2: Sample Feynman diagram of Z + $b\bar{b}$ or $c\bar{c}$. Many other diagrams at higher orders contribute to $Z + b\bar{b}$ and $Z + c\bar{c}$. Z+$b\bar{b}$ and Z+$c\bar{c}$ is the largest background of $ZH \rightarrow \ell^+\ell^- b\bar{b}$.

Z + jets

To model Z + heavy flavor background, we used both Pythia [50] and Alpgen+Herwig [55, 56] generators. The primary Feynman diagram for Z + heavy flavor jets is shown in Figure 4.2. To set the number of predicted events, we used the expected number of events derived from the Pythia generator where the total $\sigma_Z \cdot BR(Z \rightarrow \ell^+\ell^-)$ is 252.5 pb. Based on a recent study conducted at the Tevatron, a 40% uncertanity was set on this expectation [57].

Both Monte Carlo generators are used to simulate the Z + jets pretagged. This region is a control region because it has little signal. This region is mostly Z + light flavored jets but has a similar tree diagram as the Z + heavy flavor. After a comparison between the data and the two Monte Carlo outputs, the Alpgen+Herwig generator was selected as the nominal sample with the Pythia generator used as a systematic for the analysis.

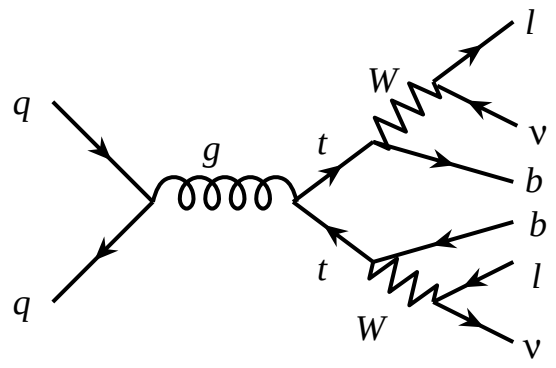

Figure 4.3: Feynman diagram of $t\bar{t}$ in a dilepton decay. This diagram accounts for 85% of all $t\bar{t}$ events. Most of the rest comes from gluon collisions.

Top Dilepton

As previously mentioned, the top quark was first discovered at the Tevatron by the CDF and DØ experiments in 1995 [3, 4]. The top quark decays nearly 100% of the time into $W + b$. An e^+e^- or $\mu^+\mu^-$ pair occurs in 3.3% (6.6% total) of all $t\bar{t}$ events. This decay is shown in Figure 4.3. For this analysis a Pythia $t\bar{t}$ sample was used with a top mass of 175 GeV/c^2 and an assumed cross section of 6.7 pb, which is appropriate for that mass.

Top dileptons are one of the few backgrounds that does not include a real Z. The Z mass window requirement dramatically reduces the amount of $t\bar{t}$ events. Also, these events have a much higher $\not\!\!E_T$ because of the neutrino content of the final state. Finally, $t\bar{t}$ events tend to be some of the most energetic events in the data sample because of the high mass of the top quark.

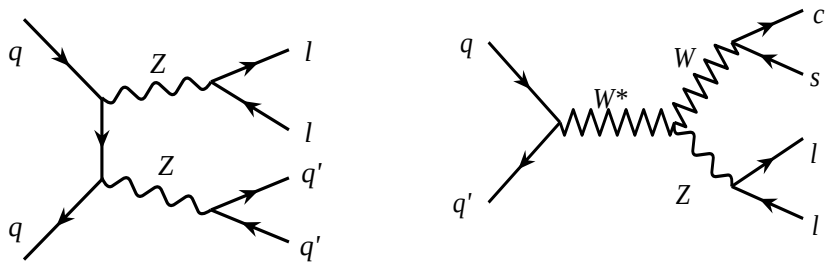

Figure 4.4: Feynman diagram of ZZ (top) and ZW (bottom) in a dilepton decay.

Diboson

Diboson events are very similar to the ZH in that they all have a large massive boson produced with a real Z boson. Figure 4.4 shows the primary diboson backgrounds for this search, ZZ and ZW. Fortunately, their cross section is not much larger than that of ZH. Another diboson process, WW + two partons, is of less significance in this analysis because it is unlikely for a WW event to fake a Z.

For this analysis, the diboson processes are modeled with Pythia Monte Carlo and filtered for high-P_T leptons. The ZZ cross section is 1.36 pb. For a ZZ/γ^* sample, the high-P_T lepton selection is 6.7% efficient. The ZW cross section is 3.2 pb. We selected the samples so that they would contain two high-P_T leptons. The high-P_T selection is 6.35% efficient for this sample.

4.3.2 "Mistags"

A large portion of the background comes from events that do not come from b hadrons or c hadrons, but are still tagged by the SecVtx algorithm. These events are colloquially known as "mistags." In Section 3.3.5, a rate of 1% was quoted as the

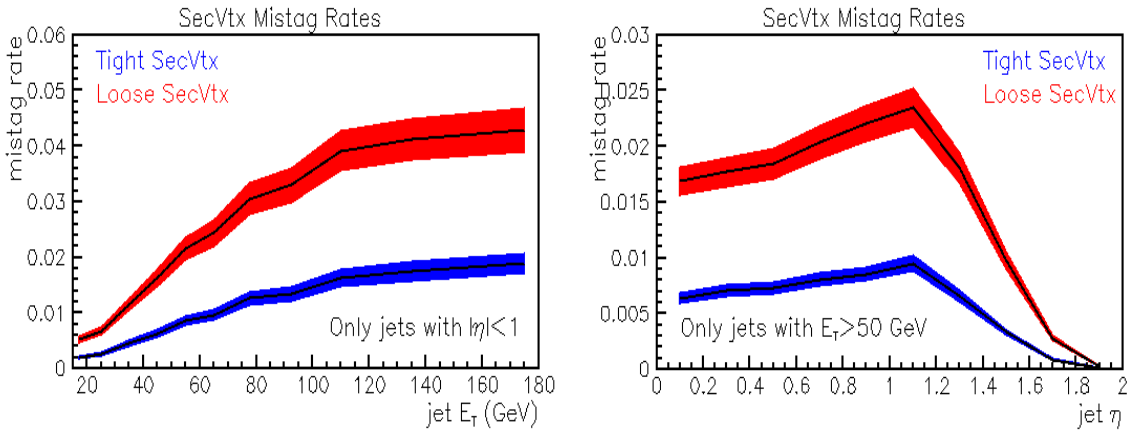

Figure 4.5: SecVtx mistag rate. The mistag rate of the SecVtx algorithm per b jet as function of E_T (left) and η (right).

mistag rate. However, since the Z + light-flavored jets cross section is much larger than Z+$b\bar{b}$, there is a significant amount of these jets that pass this cut. Most of these events are caused by mismeasurement of tracks in the events. There is another subset of mistags caused by long-lived K_S and Λ decays. There are also nuclear interactions with the detector material (the beam-pipe or the inner silicon layers) as well.

To estimate the number of events and their kinematics, we use the pretagged data and CDF's "mistag matrix." The mistag matrix is a five variable parameterization that estimates negative tags.It was measured using the inclusive jet data. The five variables used in the mistag matrix are: Jet E_T, number of tracks in a jet, primary vertex z, number of vertices in the event, and jet η. Figure 4.5 show the mistag matrix as a function of E_T and η. An important feature of the mistag matrix is that as jets become more energetic, they are more likely to be "mistagged." Since the Higgs boson is relatively massive, this background is very significant.

The mistag matrix is applied to the pretagged data sample and is used to estimate the number of negative SecVtx tags in the sample. For the double tagged sample, we apply the mistag matrix over pairs of two taggable jets in the pretag sample to find the predicted number of double loose negative tag events. Since the mistag matrix by itself only provides the estimated number of negative SecVtx tags, an asymmetry factor must be applied on a jet-by-jet basis to find the number of mistags.

The pretag sample contains approximately 15% real b and c-jets. It is necessary to remove this content from the positive "mistagged" estimate. To do so, we use the Monte Carlo samples of the Z+$b\bar{b}$, Z+$c\bar{c}$, and $t\bar{t}$ and apply the mistag matrix and asymmetry factors to the expected pretag yield. We then subtract these quantities from the data based "mistag" estimate.

A good test to see how well the "mistags" are modeled is to see how the negative tags are modeled by the matrix. The number of negative tags is in good agreement with the prediction for both electrons and muons.

4.3.3 "Fake Leptons"

The final background to consider are jets that fake a lepton. In most cases, this occurs when a real lepton is coupled with a jet that passes the "loose" cuts. The electron fake rate was estimated from jet data.

To find the rate and kinematic distributions of these events a electron fake rate was measured. Electron fake rates are determined from CDF data that come in Jet triggers (JET20, JET50, JET70, JET100). The rate a jet passed "loose" electron cuts from Table 4.5 was measured, and a function was developed based on the energy of the jet, as shown in Figure 4.6. Different rates were determined for the central

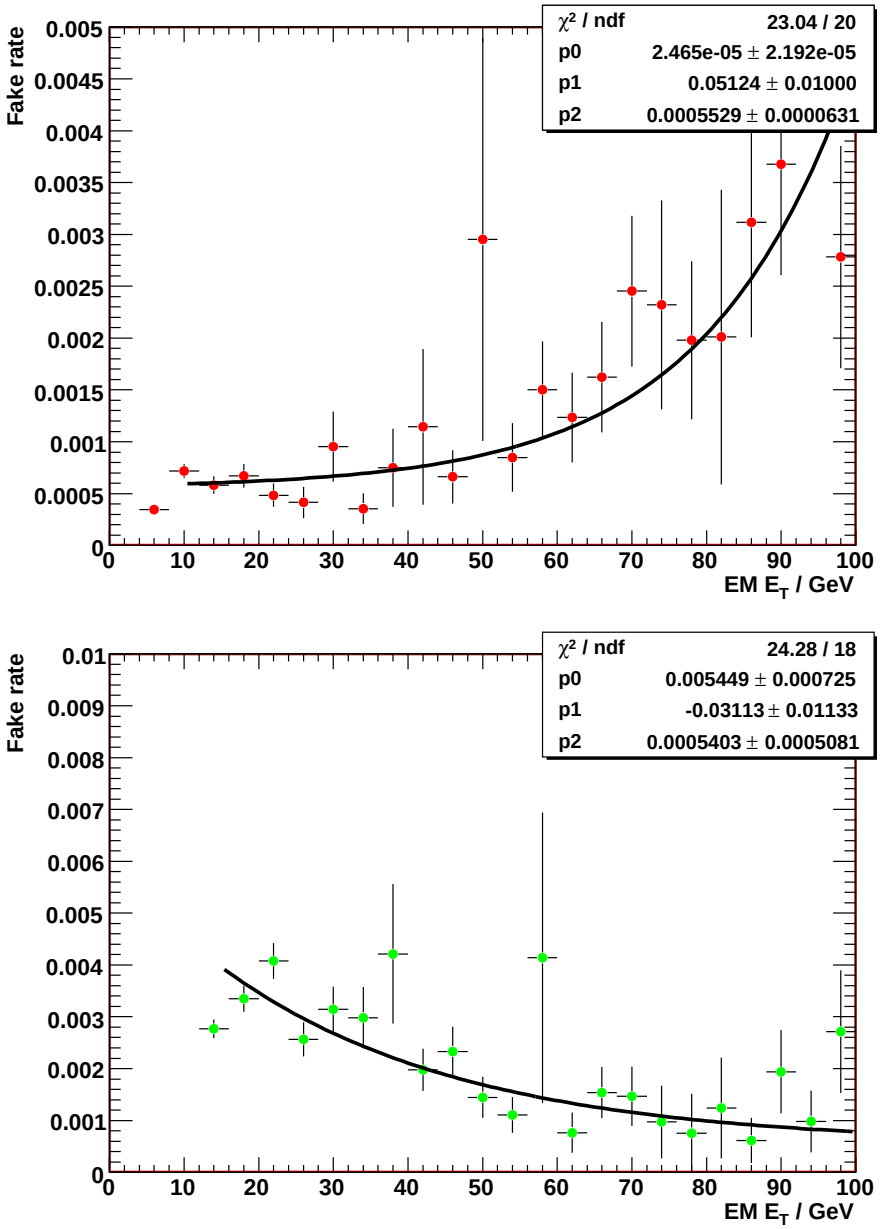

Figure 4.6: Determination of electron fake rates. Plotted are the rates for a jet in the central region (top) and plug region (bottom) to fake an electron as a function of E_T. Overlayed is the fake rate function determined from the data.

electron sample and the plug electron sample. The combined jet data were fit using a function with a constant and an exponential:

$$f(x) = a + e^{bx+c} \tag{4.1}$$

where x is the raw jet E_T and a, b, and c are fitted constants. The overlay of this equation on the combined data is seen in Figure 4.6. For jets with $E_T > 100\ GeV$, a fake rate of 0.05 was assigned for these jets, due to limited statistics. The "trigger jet," which is biased with real electrons, was removed. A requirement of $\not\!\!E_T < 15$ GeV removes W events and the Z contribution is tiny. Rates are consistent across different jet samples with different trigger level cuts.

For muon fake events, it is assumed that the fake rate is approximately the same as the same-charge muon data. The same-charged dimuon pretag shape is use to model the kinematic shape of fake muon events. In the single tagged sample, there was 1 event with same-charged muons. For the double tagged sample, the expected number of fake muon events are scaled down by 10%, which is consistent with the observed amount by which the electron sample is scaled down.

4.4 Expected Number of Events

The number of events in data is consistent with amount expected from the background models, as seen in Tables 4.11 and 4.12. In the Z + 2 jets category the absolute Monte Carlo prediction has a 20% uncertainty. Most importantly, the single and double tag expectations closely match what was found in the data. The final selection expected 102 events in the single tag channels and found 100 events in the data. In the double tag channel, 13 events were expected and 11 were found in the data.

The largest background after the full selection is Z + jets production followed by $t\bar{t}$ production. Combining both electrons and muons, 0.64 $ZH(M_H = 120\ GeV/c^2)$ events are anticipated assuming the Standard Model cross section value. The signal to background ratios of the selections are small, therefore an advanced selection criteria becomes necessary.

Sample	2 Leptons	Z Selected	$\geq$1 Jet	$\geq$ 2 Jets	2 loose	1 tight ($\neq$2 loose)
ZH_{120GeV/c^2}	0.62	0.58	0.56	0.49	0.10	0.19
$t\bar{t}$	29	7.0	6.9	6.0	1.3 ± 0.3	2.3 ± 0.5
ZW	30	27	18	12	0.017 ± 0.003	0.51 ± 0.10
ZZ	44	39	23	17	0.58 ± 0.11	1.8 ± 0.4
$WW2p$	24	5.9	3.3	1.5	0.008 ± 0.002	0.020 ± 0.004
$Z \rightarrow \tau\tau$	320	11	1.0	0.42	0.00	0.00
fakes	1700	340	53	20	0.1 ± 0.1	1 ± 1
$Z \rightarrow \mu^+\mu^-$	53,000	46,000	4200	1000	3.3 ± 1.0	35 ± 7
(b events)	650	580	140	50	2.5 ± 1.0	15 ± 6
(c events)				110	0.43 ± 0.17	8.2 ± 3.3
(mistags)	Predicted mistags from data:				$0.36 \pm .09$	12 ± 2
Total	55,000	46,000	4300	1100	5.0 ± 1.1	41 ± 7
Data (972 pb^{-1})	56,740	47,982	4128	1240	5	46
Negative Tags	Predicted:				0.27	11 ± 1
	Found				1	12

Table 4.11: Muon events background expected and data found table. Amount of expected and observed events in $\int Ldt = 0.97 fb^{-1}$ of muon data at various cuts in the event selection. The Higgs signal assumes a $\sigma(ZH) = .093$ pb and $BR(H \rightarrow b\bar{b}) = 0.68$. Errors shown are from systematics.

Sample	2 Leptons	Z Selected	$\geq$1 Jet	$\geq$ 2 Jets	2 loose	1 tight($\neq$2 loose)
ZH_{120GeV/c^2}	0.83	0.76	0.73	0.63	0.13	0.25
$t\bar{t}$	37.0	9.0	8.8	7.7	$1.5 \pm .3$	2.9 ± 0.6
ZW	46	41	26	18	0.024 ± 0.005	0.72 ± 0.14
ZZ	61	54	30	22	0.76 ± 0.15	2.16 ± 0.43
$WW2p$	34	7.9	4.4	2.1	0.006 ± 0.001	0.040 ± 0.008
$Z \rightarrow \tau\tau$	540	27	2.8	0.84	0.00	0.00
fakes	1200	320	42	16	0.13 ± 0.07	0.89 ± 0.44
$Z \rightarrow e^+e^-$	96,000	85,000	6900	1600	5.0 ± 1.5	54 ± 11
(b events)	1019	910	210	70	3.8 ± 1.5	21 ± 8.8
(c events)				160	0.58 ± 0.22	14 ± 5
(mistags)	Predicted mistags from data:				0.63 ± 0.15	20 ± 3
Total	98,000	85,000	7100	1700	7.4 ± 1.6	61 ± 11
Data (1019 pb^{-1})	102,820	88242	6423	1794	6	54
Negative Tags	Predicted:				0.44 ± 0.04	17 ± 1.4
	Found				0	11

Table 4.12: Electron events background expected and data found table. Amount of expected and found events in $\int Ldt = 1.02 fb^{-1}$ of electron data at various cuts in the event selection. The ZH event expectations are based on $\sigma(ZH) = .093$ pb and $BR(H \rightarrow b\bar{b}) = 0.68$. Errors are from systematics.

CHAPTER 5

ADVANCED EVENT SELECTION

As pointed out in Chapter 2, the production cross section for the Higgs Boson is very small. The previous chapter quantified an order of magnitude difference in the size of backgrounds and the signal. In order to increase the strength of this search, two advanced techniques were used to separate the signal from the backgrounds.

This chapter begins with a brief introduction to artificial neural networks (NN) which includes a discussion of the theory and the training process behind this tool. This introduction is followed by a description of the implementation of two neural networks in this analysis. This first NN, described in Section 5.2, takes advantage of our signal's lack of final state neutrinos. This technique uses the missing transverse energy of the event to correct the jet energies to match to the parton energies. The second artificial neural network is used as a classification discriminant to distinguish between ZH signal events and the backgrounds. (Section 5.3).

5.1 Introduction to Neural Networks

The brain is a complex object. From the beginning of its development, its neurons form interconnections based on stimuli [58]. It constantly adjusts and builds new bridges while others are weakened. The brain takes inputs from its surroundings,

comes to a conclusion based on what it has learned, and reacts. At the core of the brain is the neuron. The neuron absorbs signals from stimuli, such as light, or a signal from other neurons and, if a threshold is met, it fires an electrical signal to other neurons. McCulloch and Pitts [59] developed a mathematical model for neural communication.

An artificial neural network tries to mimic the brain in order to solve problems. It is first trained on input variables with a known, desired outcome. It then builds connections between these input variables to get the desired output. This process is done repeatedly, learning from each iteration. During this process, it learns to understand relationships of the inputs in order to make better decisions. Just as actual brains are flexible, an artificial neural network is also flexible. It has been shown that a neural network is capable of reproducing any nonlinear mathematical formula [60]. Artificial neural networks have been used successfully for other analyses, including a CDF measurement the cross section of the top quark [61] .

The type of artificial neural network used for this analysis is a feed-forward network. Figure 5.1 shows the feed-forward network's architecture. There are a limited number of inputs fed into the neural network. Then a neuron-like function sends information to a hidden layer of nodes. These hidden layers make a new computation of the incoming data and sends information to an output layer of information, which again makes a decision.

Each individual node j is governed by the equation:

$$Output_j = g\left(\sum_i W_{ji} \cdot Input_i - \theta_j\right) \tag{5.1}$$

where $Input_i$ is an input from an incoming node, W_{ji} is the weight accorded to that information from i, and θ_j is the threshold needed to fire the node. The function $g(s)$

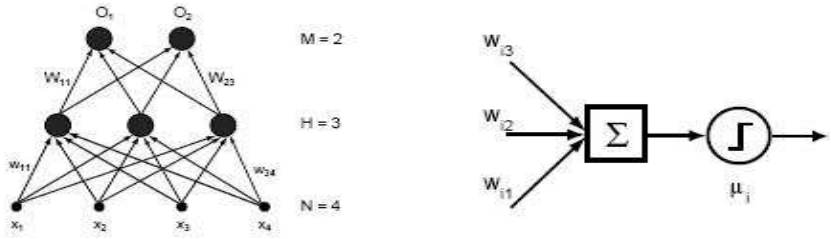

Figure 5.1: Feed-forward network architecture. On the left is a schematic of a feed-forward network. Inputs are connected to nodes in a hidden layers which in turn connect to an output layer. The drawing on the right explains the process behind every single node The inputs to a node are first added together then a possible transmission can occur.

is a smootehed step function:

$$g(x) = \frac{1}{1 + e^{-x}} \tag{5.2}$$

A value of x significantly lower than 0 does not fire the node, while a value of x significantly higher than 0 does fire the node. θ_j and W_{ij} are adjustable parameters and are changed during the training process of a NN.

The training of the neural network uses several input samples and their targeted NN outputs, $\vec{T}$. The thresholds and weights of the neural networks are initially randomized. The samples are then passed in this neural network to obtain an output $\vec{O}$. The quality of a given neural network is given by the error defined as:

$$error = \frac{1}{N_t}|\vec{T} - \vec{O}| \tag{5.3}$$

where N_t is the size of training samples used. The samples are subdivided into two subsamples; a training sample and testing sample. During the training, the weights and thresholds are adjusted in order to reduce the error of the neural network. After

a training iteration is complete, a testing sample measures the quality of the neural network. The neural network learns from past iterations of training.

A risk during training a neural network is that it may "over-train." If the number of parameters is too large or the training samples are too small, the neural network can soon identify exact events from the sample. To test if this is occurring, the errors of the testing and training samples are compared. If the training sample constantly improves while the testing sample is stable or becomes worse, then over-training has occurred.

5.2 Jet Energy Neural Network Correction

Chapter 4 showed that the signal and most of the backgrounds do not contain neutrinos. Chapter 3 stated that the measurement of lepton energy is much more precise at CDF than the measurement of jet energies. This implies that the largest source of missing transverse energy in the data sample comes from the mismeasurement of hadronic jets. This analysis employs a correction function that uses missing energy to improve the jet energy resolution. The correction is essentially a parton-jet transfer function which makes use of the correlations between the jet energies and the $\not\!\!E_T$. The function takes as inputs the $\not\!\!E_T$, $\phi_{\not\!\!E_T}$, first and second jet E_T, their η's and ϕ's, and the transverse projections of the jets onto the $\not\!\!E_T$ direction. The function produces two outputs which are scale factors to correct the E_T of each of the two jets. The directions of the jets are not changed.

A neural network produces this function by training on the inputs mentioned above and attempting to reproduce the Monte Carlo generated parton energies. The training sample consisted of ZH Monte Carlo events with Higgs masses ranging from

60 to 180 GeV/c^2 and $t\bar{t}$ events. The wide mass range prevented the neural network from over-training on a particular mass which would cause the function to produce corrections that are biased towards that mass. The NN was developed using a program called MLPfit: a tool for Multi-Layer Perceptrons [62]. These improved jet energies are used to calculate the input kinematics for our signal-to-background discriminant including, most importantly, the dijet mass, the direct measure of the Higgs mass.

Let us conduct a thought experiment to demonstrate the dynamics of the jet energy NN correction. We start with a situation where the two jets are at a 45^o degree angle from one another in ϕ. As $\not\!\!E_T$ sweeps in ϕ, the correction factor for both jets is shown in Figure 5.2. The two situations in Figure 5.2 are the same except for the amount of $\not\!\!E_T$. The figures show that the correction factor is largest when the $\not\!\!E_T$ is in the direction of a particular jet. Also, the amount of $\not\!\!E_T$ is correlated to the size of the corrections.

The neural network improved the ZH dijet mass resolution from 18% to 11% for our double tagged sample. In addition, the new reconstructed dijet mass is closer to the Monte Carlo produced Higgs mass. Figure 5.3, shows the effect of the NN Jet Corrections on the Higgs sample dijet mass. It has been estimated that each 1% of improvement in dijet mass improves the sensitivity of a Higgs search the equivalent of an additional 10% integrated luminosity [30]. This is true for searches that use the dijet mass to discriminate the Higgs boson signal from backgrounds.

This function was also tested on background events to ensure that background distributions are not sculpted to look more like a Higgs boson signal. As a figure of merit, a 2σ window around the ZH dijet mass peak before and after the jet correction functions was applied to verify an improvement in the signal-to-background

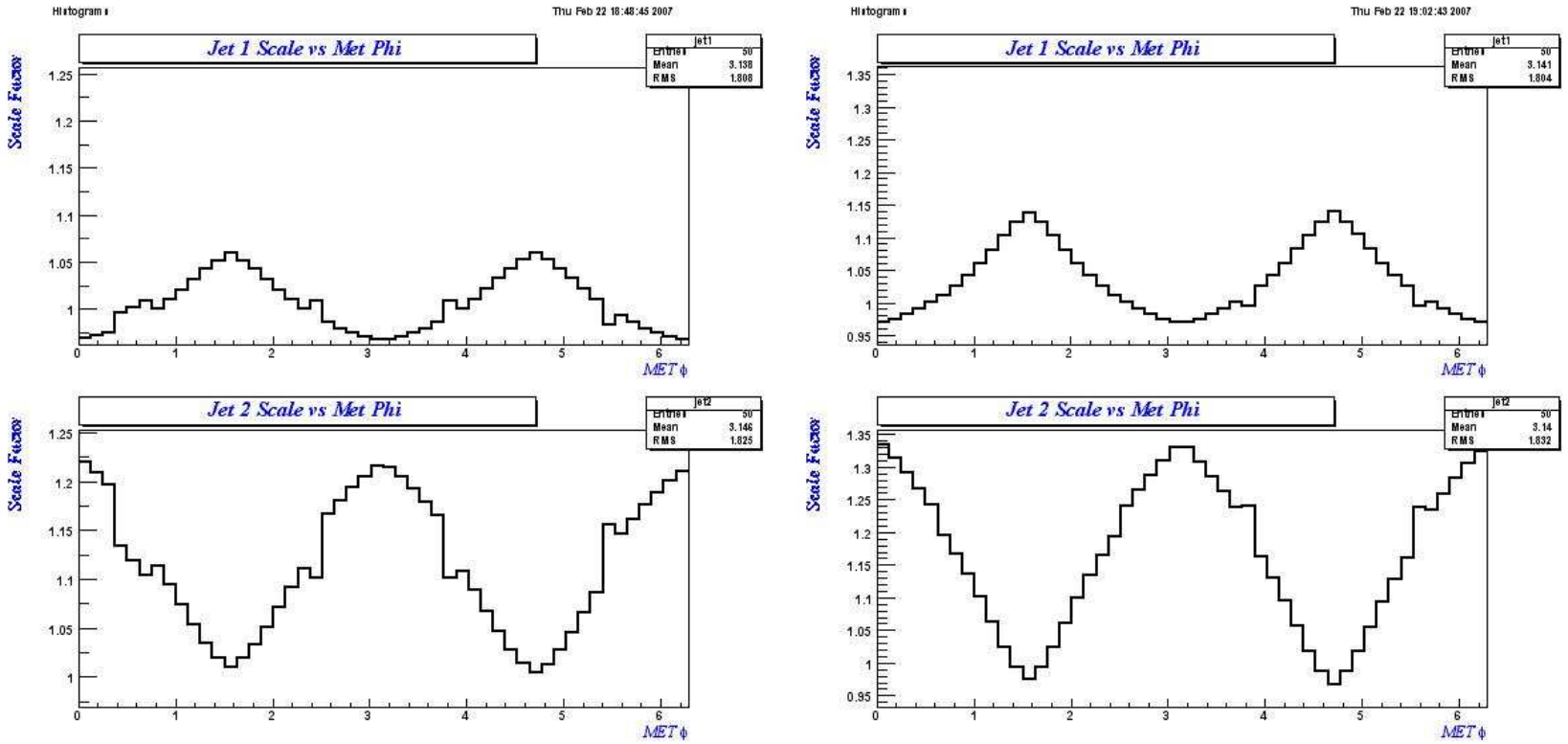

Figure 5.2: Thought experiment of NN jet energy correction. Scale factors NN jet energy correction dependent on the direction of $\not\!\!E_T$. The first jet (top plot) has an E_T of 85 GeV, $\eta = +1$, $\phi = \pi/2$. The second jet (bottom plots) has an E_T of 45 GeV, $\eta = -1$, $\phi = \pi$. The $\not\!\!E_T$ is measured to be 10 GeV on the right plots and 20 GeV on the left plots The ϕ of the $\not\!\!E_T$ is then swept around the detector and the correction factor is plotted on the y-axis.

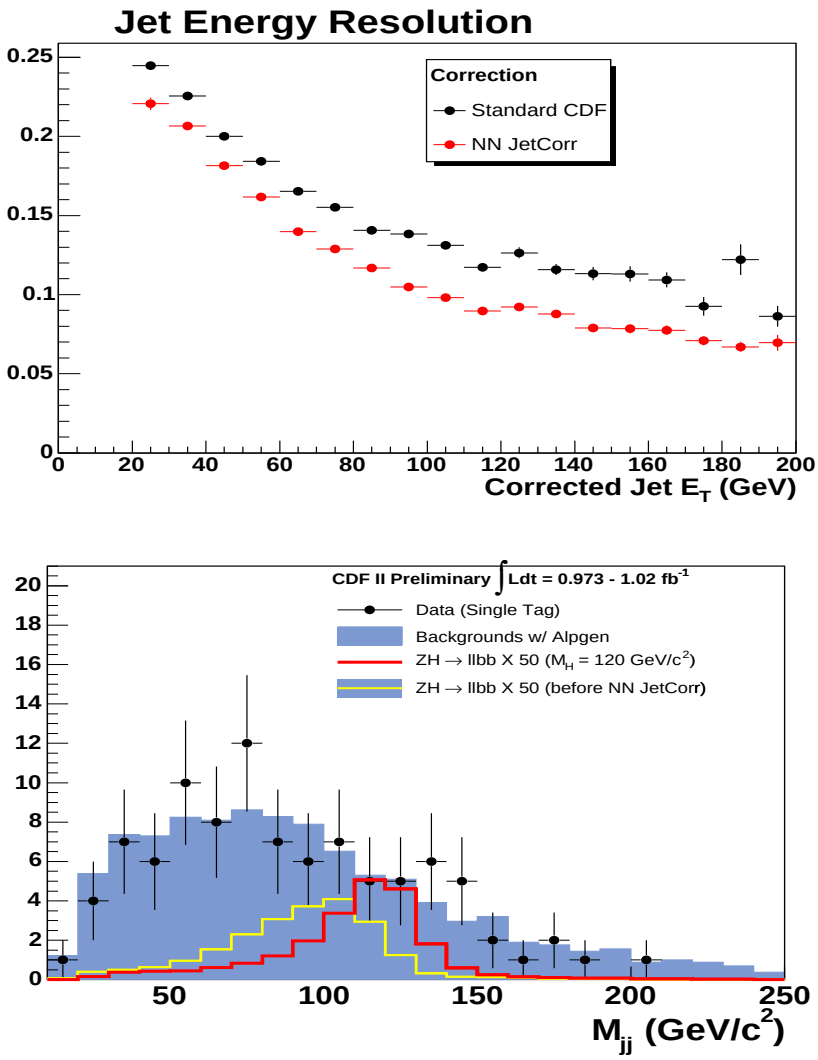

Figure 5.3: (top) Effect of the jet energy correction neural network. The improvement of jet energy resolution as a function of measured jet energy. The NN corrections dramatically improves the measured energies for a wide swath of energies. (bottom) The precorrected ZH ($M_H = 120\ GeV/c^2$) is plotted simultaneously the post corrected Higgs mass drawn 50 times the SM expectation. In addition the postcorrected total background is plotted. By using the correction, the dijet resolution of the ZH sample improves and shifts towards the production value of the Higgs mass. Also, the signal is under a smaller section of tail of the background.

discrimination. The backgrounds considered for this study were Z + jets, and dilepton $t\bar{t}$. $S/\sqrt{B}$ improved in the case of both backgrounds, and the shape of the backgrounds showed no sign of distortion. A linearity test of the NN function was performed on independent Monte Carlo Higgs boson samples using masses from 60 to 180 GeV/c^2 as well as diboson samples. No significant bias was observed.

5.3 Classification Artificial Neural Network

To further improve signal-to-background discrimination after event selection, a separate artificial neural network was trained on a variety of kinematic variables to distinguish ZH from backgrounds. This network is referred to as the classification artificial neural network (CANN). The CANN was used to search for the Higgs boson and eventually set a limit on the ZH cross section.

5.3.1 Training and Structure of the Neural Network

Many different styles of neural networks were tested before arriving at a final structure. At first, a 1-dimensional NN was trained between ZH and Z + jets. While this was very successful at separating the two processes, the shape of the NN output for $t\bar{t}$ peaked in the signal region, reducing the signal sensitivity. Another attempt used two NNs in series. The first distinguished $t\bar{t}$ against ZH and a cut was made to remove $t\bar{t}$. The second NN separated Z + jets from ZH for which the shape of the NN distribution was to be used as a discriminant. The $t\bar{t}$ NN rejected 82% of $t\bar{t}$ while only removing 5% of signal, However, the 18% remaining $t\bar{t}$ peaked very strongly in the ZH signal region in the subsequent Z + jets versus ZH NN, leading to weakened signal sensitivity. The solution was a 2-D NN, trained to discriminate $t\bar{t}$ vs ZH on one axis, and Z+jets vs ZH on the other axis.

The selection of the neural inputs was optimized using an iterative process. The OSU RootJetnet interface to the Jetnet neural network program [63] was the tool used to develop the network. First, variables that discriminated between ZH and the backgrounds were identified. The inclusive set of variables are :

- Z mass[1]
- $\not\!\!E_T$ projected on jet 1 ($\equiv \not\!\!E_T \cdot \cos\Delta\phi_{Jet\ 1, \not\!\!E_T}$)
- $\not\!\!E_T$ projected on jet 2
- $\not\!\!E_T$ projected on the vector sum of all jets
- Z projected on the vector sum of all jets
- P_T of Z
- E_T of jet 1
- E_T of jet 2
- η of Z
- η of jet 1
- η of jet 2
- Corrected $\not\!\!E_T$
- H_T : sum of $\not\!\!E_T$ the first two jet E_T's, and the two lepton E_T's
- $\Delta E_T \equiv E_T$ of jet 1 - E_T of jet 2
- jetP_T: P_T of the vector sum of the two leading jets
- dijet mass: Dijet invariant mass
- ΔRj1j2: ΔR between jet 1 and jet 2
- ΔRj1Z: ΔR between Z and jet 1
- ΔRj2Z: ΔR between Z and jet 2
- ΔRjetsZ: ΔR between Z and combined jet 4-vector

[1]The object constructed from the two leptons is referred to as the Z, although due to fake leptons and $t\bar{t}$ this is not strictly true for all events.

- aplanarity - a description of the entire event's shape
- sphericity - a description of the entire event's shape
- Total Mass : Mass of all objects in event
- Mass of Z and dijet combined

This optimization is done by first determining the best one-variable NN of all the above variables. The figure of merit is the error of the NN based on Equation 5.3. Next, the best variable is kept and another loop starts over all other the variables to determine the best two-variable NN. The procedure then is repeated until the best N-variable network is finally selected once the N+1-variable network shows less than a 0.5% improvement in the NN error. Once the best N-variable NN is chosen, the number of hidden layers is optimized.

The final neural network configuration had 8 input variables, 17 hidden nodes, and 2 output nodes. The signal was targeted to $(1, 0)$, the $t\bar{t}$ background at $(1, 1)$ and the other backgrounds at $(0, 0)$. The optimization of the variables is shown in Figure 5.5 and the list, in order of importance are:

- H_T : sum of $\not\!\!E_T$ first two jet E_Ts, and lepton E_Ts
- Corrected $\not\!\!E_T$
- dijet mass: Dijet invariant mass
- ΔRj1Z: ΔR between Z and jet 1
- ΔRj2Z: ΔR between Z and jet 2
- ΔRj1j2: ΔR between jet 1 and jet 2
- sphericity
- Jet 2 η
- Not used: the next best variable would be the $\not\!\!E_T$ projected on the first jet.

Figure 5.4 shows the three samples used for training in the CANN output, each individually normalized 1. The outputs all peak in the desired region.

The neural network output distributions are shown for all the backgrounds in Figures 5.6 and 5.7 for the single-tagged sample. These templates are used in all subsequent studies.

5.3.2 Validation of Kinematic Input Variables

It is crucial to test whether the input variables of the neural network are modeled well by the simulation. An excellent control sample to understand this modeling is the pretag sample, i.e. the basic event selection before requiring a b tag. The comparison to data was done with Z + jets being modeled by both Alpgen+Herwig and Pythia samples. They are overlaid against the data for the kinematic inputs of the CANN and others of interest in Figures 5.8 and 5.9.

The data are generally well modeled by the simulation. At low H_T and low jet E_T, values the Alpgen+Herwig simulation underestimates the data, while the Pythia overestimates. It is seen that Pythia generally gives a poorer description of the data, particularly at high H_T and high dijet mass. However, it agrees well at low values of H_T and jet E_T. The Alpgen+Herwig sample is used as the nominal shape for Z + jets distributions while the Pythia shape is accounted for in the systematic uncertainty.

Finally the data and the simulation are compared in the b-tagged samples. Figures 5.10 and 5.11 show comparisons of data and Monte Carlo for many kinematic properties of the events single tagged events. Figure 5.12 and 5.13 show the same for the double tagged events. The data agree well with the Standard Model backgrounds within the current statistical uncertainties.

5.3.3 Test of Neural Network output

The most critical check of the validity of the neural network was the comparison of the neural net distribution itself with the pretag sample. Figure 5.14 shows the pretag data output of the CANN. It looks very similar to our Z + jets expectation. This is not surprising since the pretag selection consists of 95% Z + jets. To compare the data to the background model, the CANN output is projected onto both of its axes. The 1-dimensional projections onto the x and y-axes are shown in Figure 5.15. The x-axis is used to discriminate between Z+jets and ZH, the y-axis is used to discriminate between $t\bar{t}$ and ZH. The figure contains a background model with the Alpgen+Herwig and Pythia predictions of Z + jets.

To compare the data and Monte Carlo further, specific regions of the 2-D NN are selected. As a test of Z + jets background, the $t\bar{t}$ background is suppressed by selecting events with $y_{NN} < 0.25$. Testing the $t\bar{t}$ requires selecting events with $x_{NN} > 0.75$ to suppress the Z + jets background. Figure 5.16 shows the projections for these selected regions. Again, it is observed that the Alpgen+Herwig sample is in good agreement with the data.

5.4 Summary

Two different neural networks were developed for this analysis. One uses the $\not\!\!E_T$ to improve the jet energy resolution. Another artificial neural network separates the signal from backgrounds in a two dimensional output. The output of this classification artificial neural network is the discriminant used to search for the Higgs boson. Data to backgrounds comparisons of the input variables, and output variables of the neural

network showed the integrity of the classification artificial neural network. In the next chapter, I discuss the systematics errors for the kinematics of the CANN.

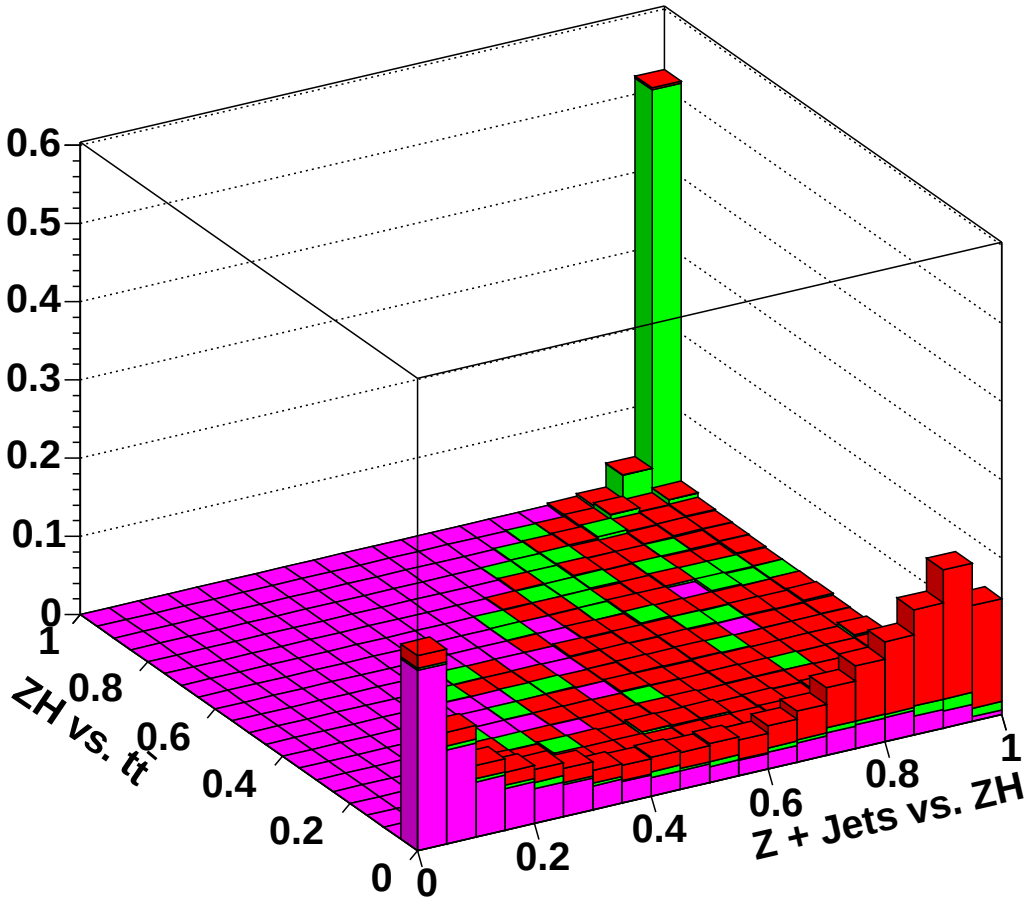

Figure 5.4: CANN output of the training samples. All the training samples are plotted together and normalized to 1 in 2-D to show relative output. ZH(M_H=120GeV/c^2) is plotted in red and is targeted in (1,0). $t\bar{t}$ is plotted in green and is targeted towards (1,1). $Z + b\bar{b}$ is plotted in magenta and is targeted towards (0,0).

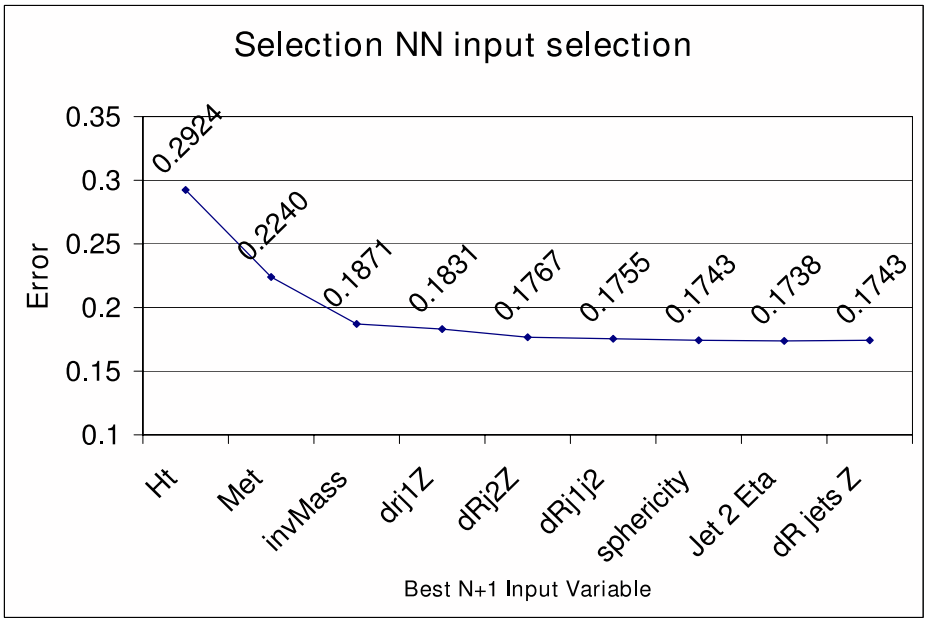

Figure 5.5: Optimization of the classification artificial neural network. The top plot shows the testing error, where the x-axis is the number of variables in the best N-variable NN. Adding in the best 9th variable does not show improvement.

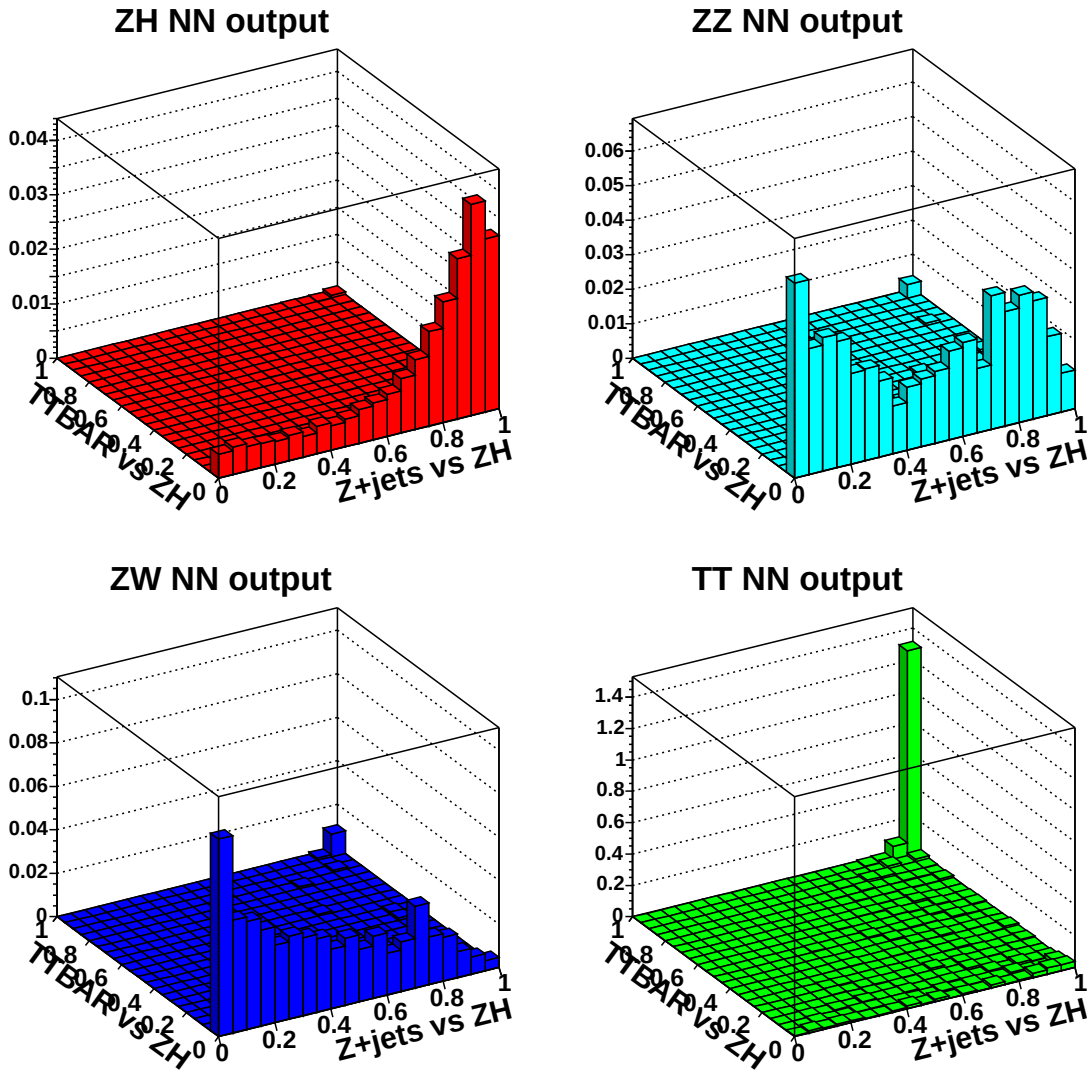

Figure 5.6: First set of CANN shapes. The NN distribution templates for ZH (red, upper left), ZZ (cyan, upper right), ZW (blue, lower left), $t\bar{t}$ (green, lower right).

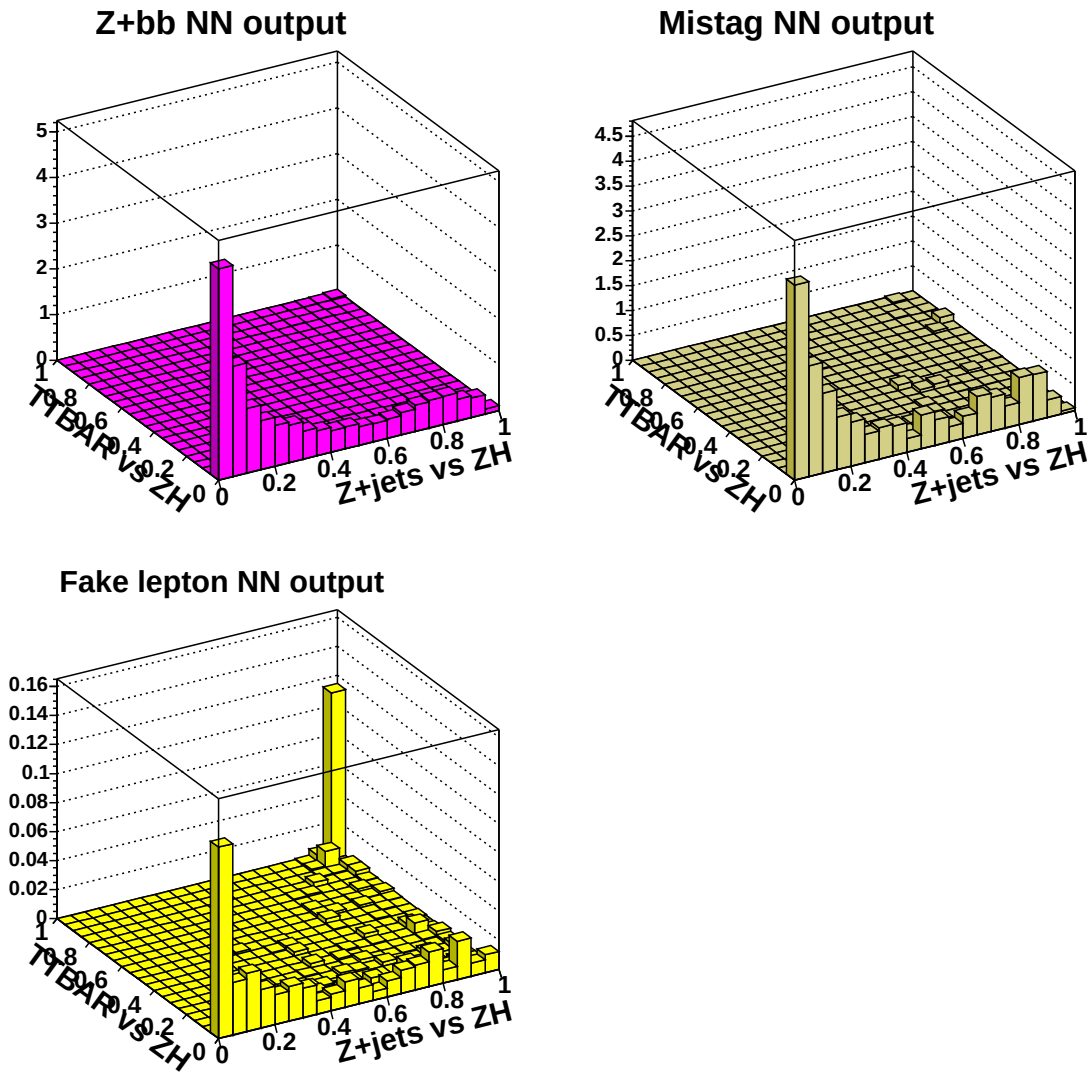

Figure 5.7: Second set of CANN shapes. The NN distribution templates for $Z + b\bar{b}$ (pink, upper left), fakes (yellow, lower left), mistags (drab, upper right).

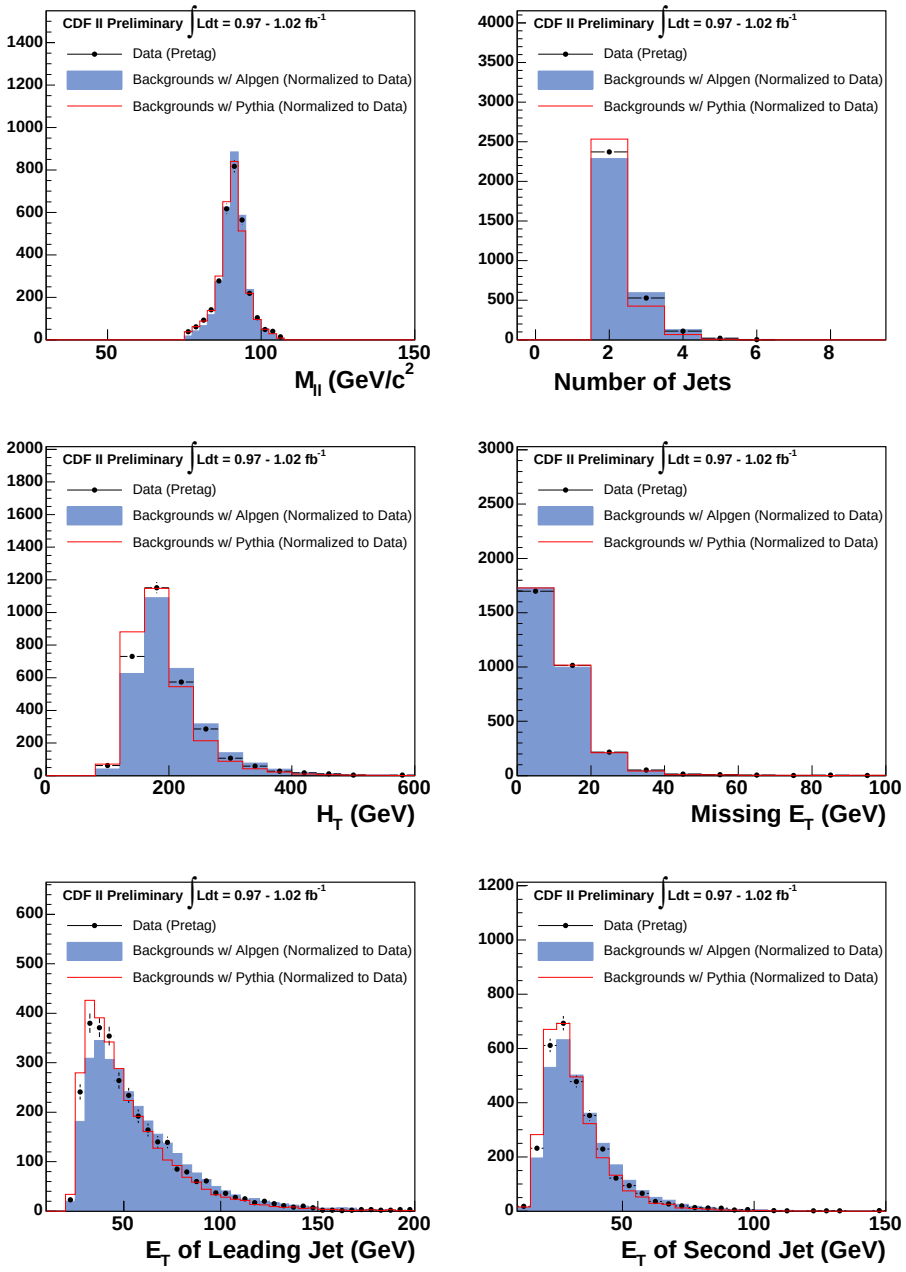

Figure 5.8: Pretag kinematic distributions 1. Pretagged data compared to Monte Carlo expectations. The model which uses the Alpgen+Herwig Z + jets Monte Carlo simulations are in blue, those that use Pythia Z + jets is represented with the red line: invariant dilepton mass (upper left), number of jets (upper right), H_T (middle left), missing E_T (middle right), E_T of leading (lower left) and subleading (lower right) Jets.

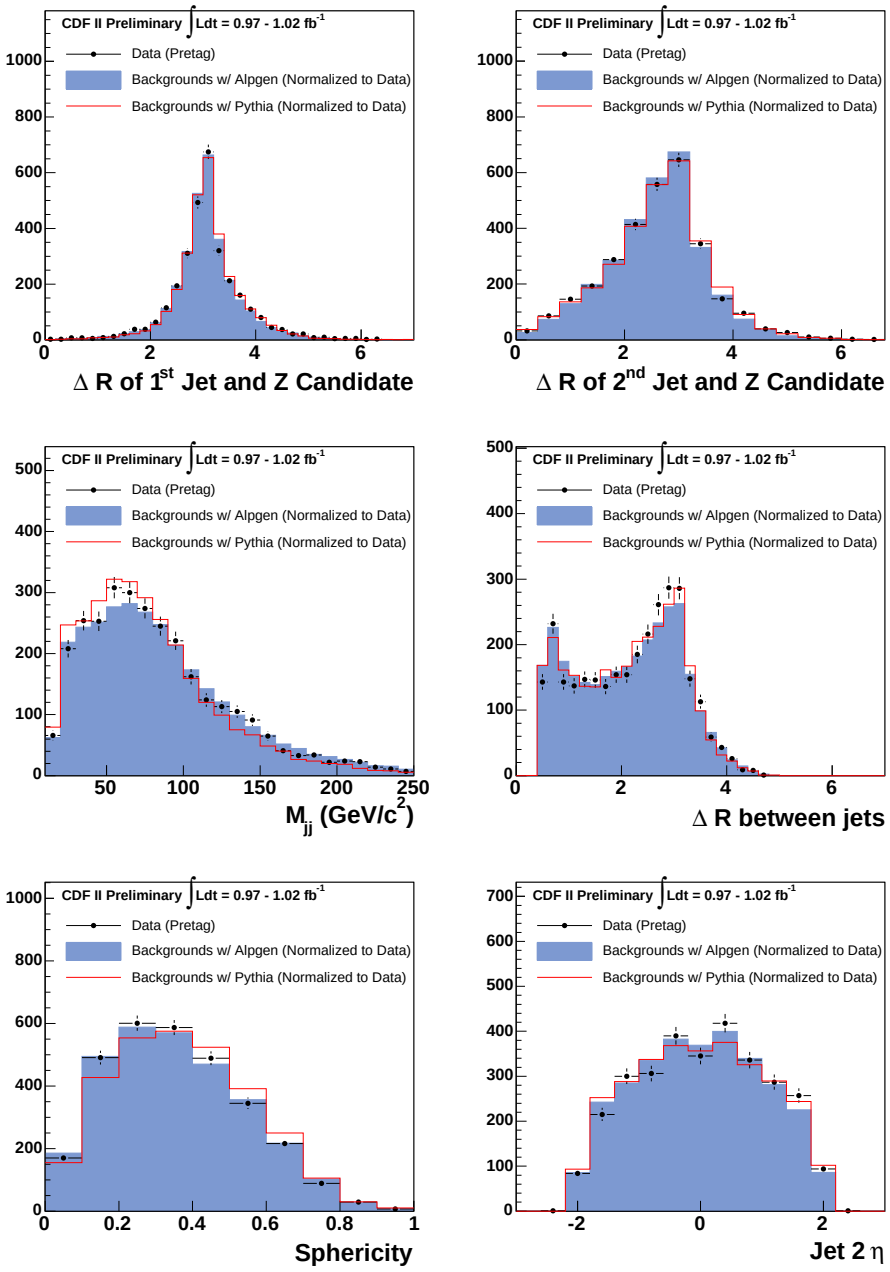

Figure 5.9: Pretag kinematic distributions 2. Pretagged data compared to Monte Carlo expectations. The model which uses the Alpgen+Herwig Z + jets Monte Carlo simulations are in blue, those that use Pythia Z + jets is represented with the red line: ΔR of leading jet and Z (upper left), ΔR of second jet and Z (upper right), invariant mass of two leading jets (middle left), ΔR of leading and second jets (middle right), sphericity of 4 relevant objects (bottom left), η of second jet (bottom right.)

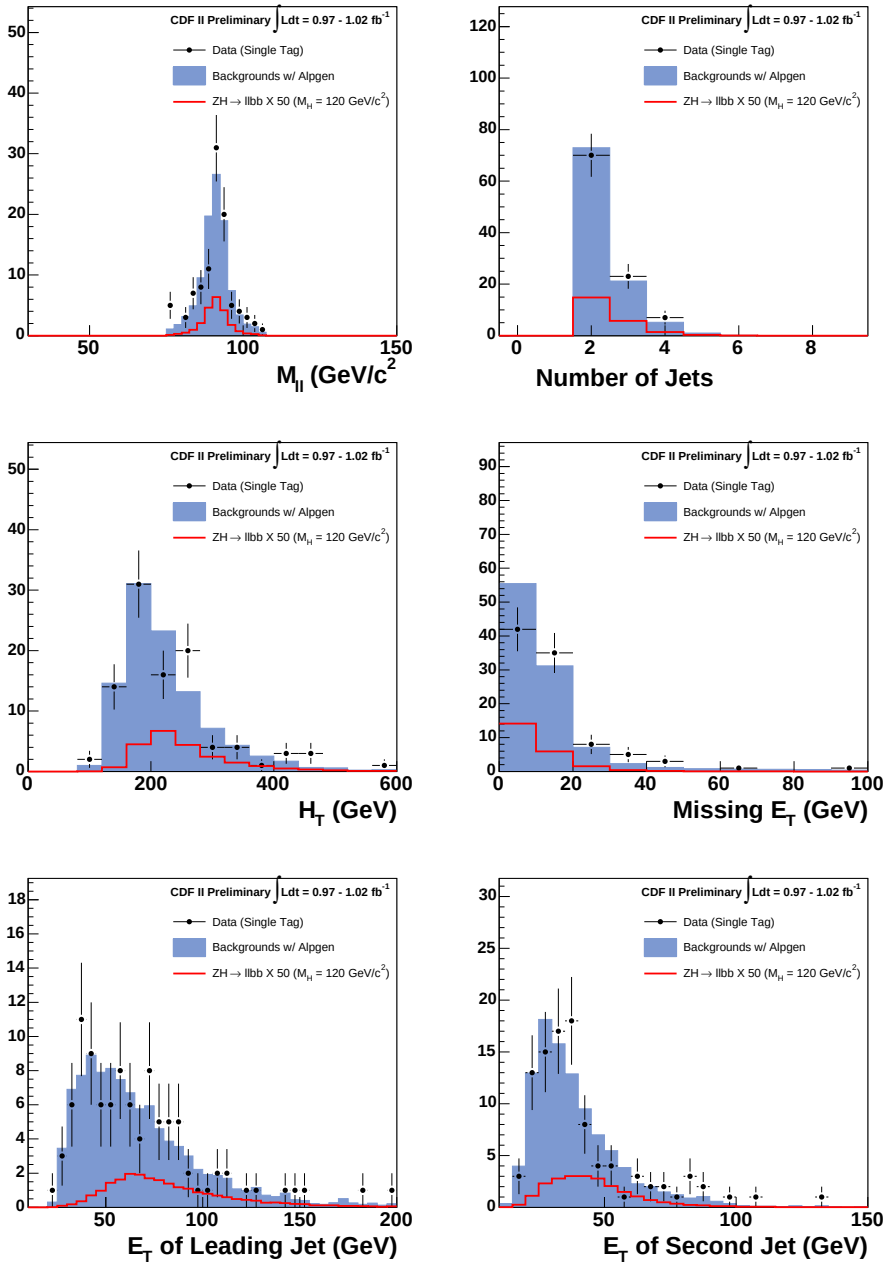

Figure 5.10: Single tagged kinematic distributions 1. Single tagged data compared to Monte Carlo expectations. The background expectation are in blue, ZH (M_H = 120 GeV/c^2) is represented with a red line and scaled to 50 times the expected value: invariant dilepton mass (upper left), number of jets (upper right), H_T (middle left), missing E_T (middle right), E_T of leading (lower left) and subleading (lower right) Jets.

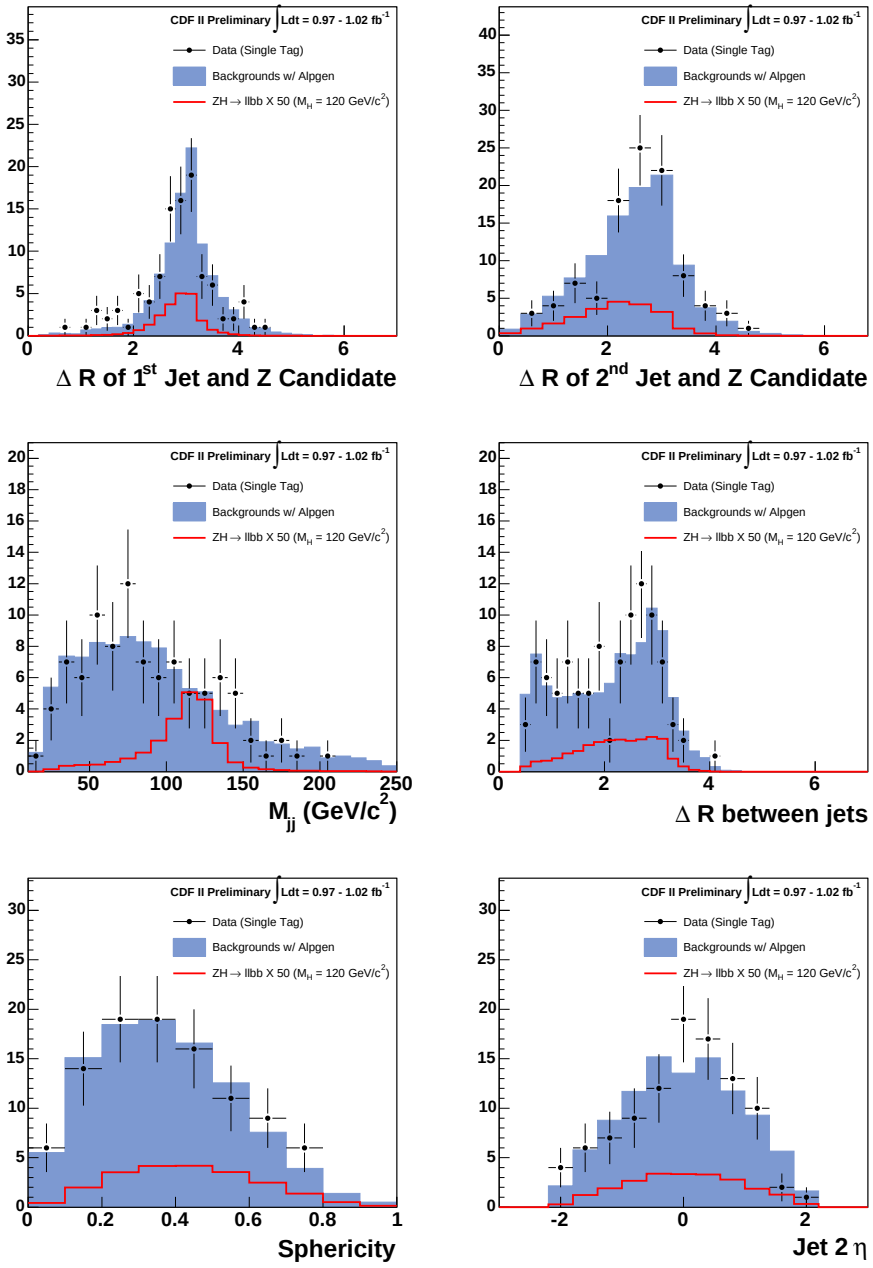

Figure 5.11: Single tagged kinematic distributions 2. Single tagged data compared to Monte Carlo expectations. The background expectation is in blue, ZH ($M_H = 120$ GeV/c^2) is represented with a red line and scaled to 50 times the expected value: ΔR of leading jet and Z (upper left), ΔR of second jet and Z (upper right), invariant mass of two leading jets (middle left), ΔR of leading and second jets (middle right), sphericity of 4 relevant objects (bottom left), η of second jet (bottom right.)

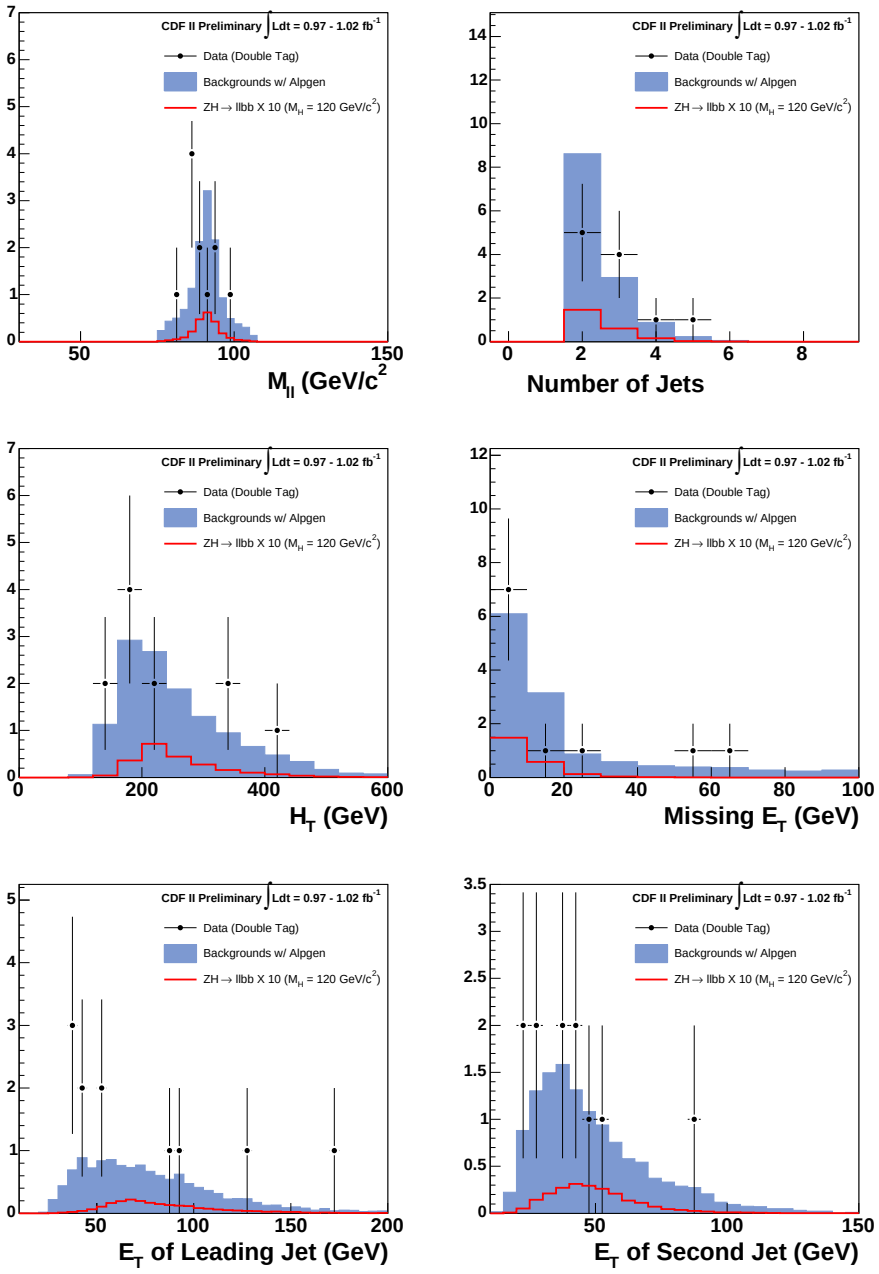

Figure 5.12: Double tagged kinematic distributions 2. Double tagged data compared to Monte Carlo expectations. The background expectations are in blue, ZH ($M_H = 120$ GeV/c^2) is represented with a red line and scaled to 10 times the expected value: invariant dilepton mass (upper left), number of jets (upper right), H_T (middle left), missing E_T (middle right), E_T of leading (lower left) and subleading (lower right) Jets.

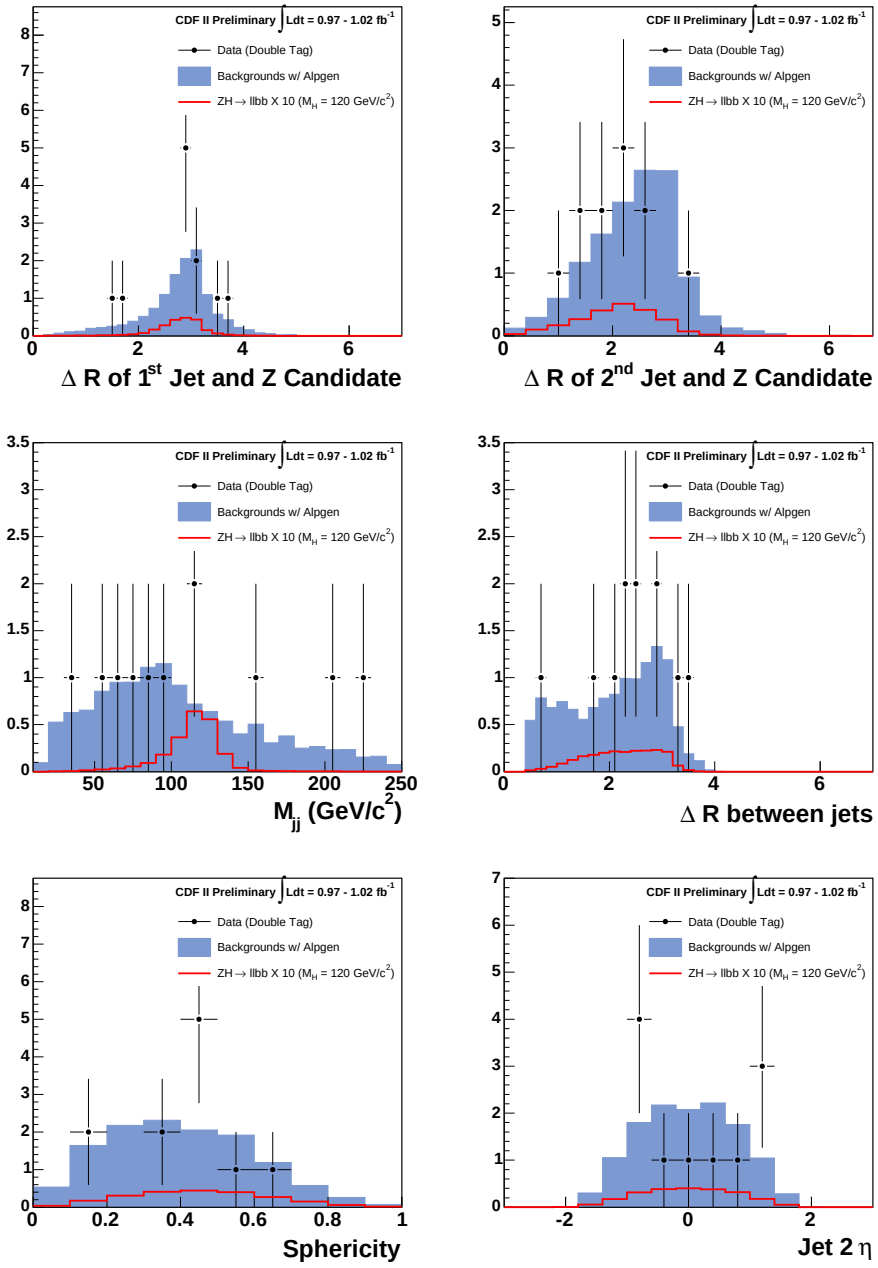

Figure 5.13: Double tagged kinematic distributions 2. Double tagged data compared to Monte Carlo expectations. The background expectations are in blue, ZH ($M_H = 120$ GeV/c^2) is represented with a red line and scaled to 10 times th3 expected value: ΔR of leading jet and Z (upper left), ΔR of second jet and Z (upper right), invariant mass of two leading jets (middle left), ΔR of leading and second jets (middle right), sphericity of 4 relevant objects (bottom left), η of second jet (bottom right.)

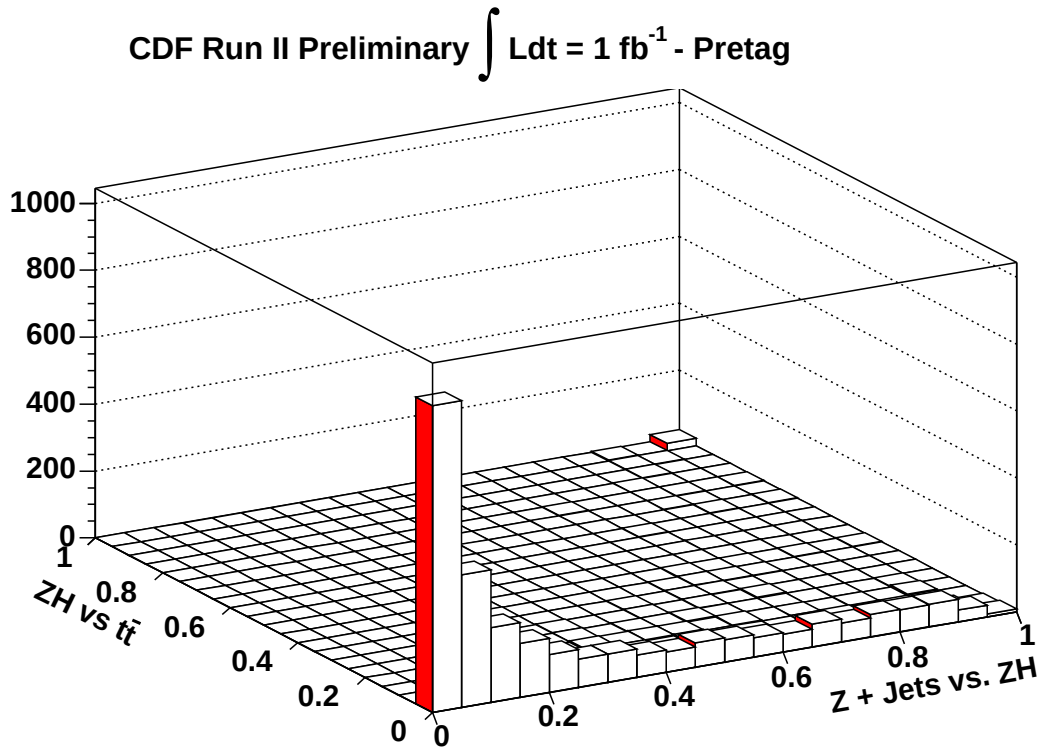

Figure 5.14: CANN pretagged in data. Pretagged data CANN in 1 fb^{-1} of CDF data.

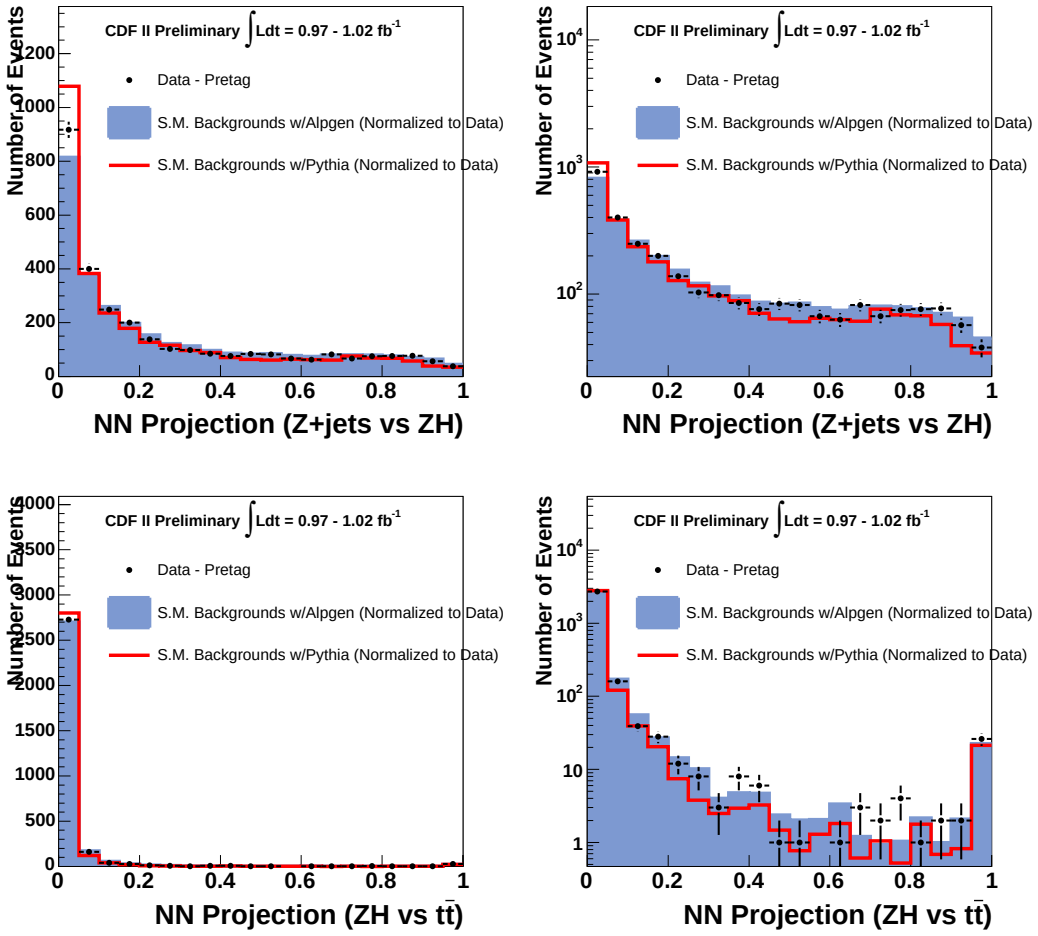

Figure 5.15: Pretagged CANN data compared to Monte Carlo expectations. Shown are the projections of the CANN onto the x-axis (upper plots in linear and logarithmic scale) and y-axis (lower plots) The Monte Carlo which uses the Alpgen+Herwig Monte Carlo simulations are in blue, Pythia is represented with the red line.

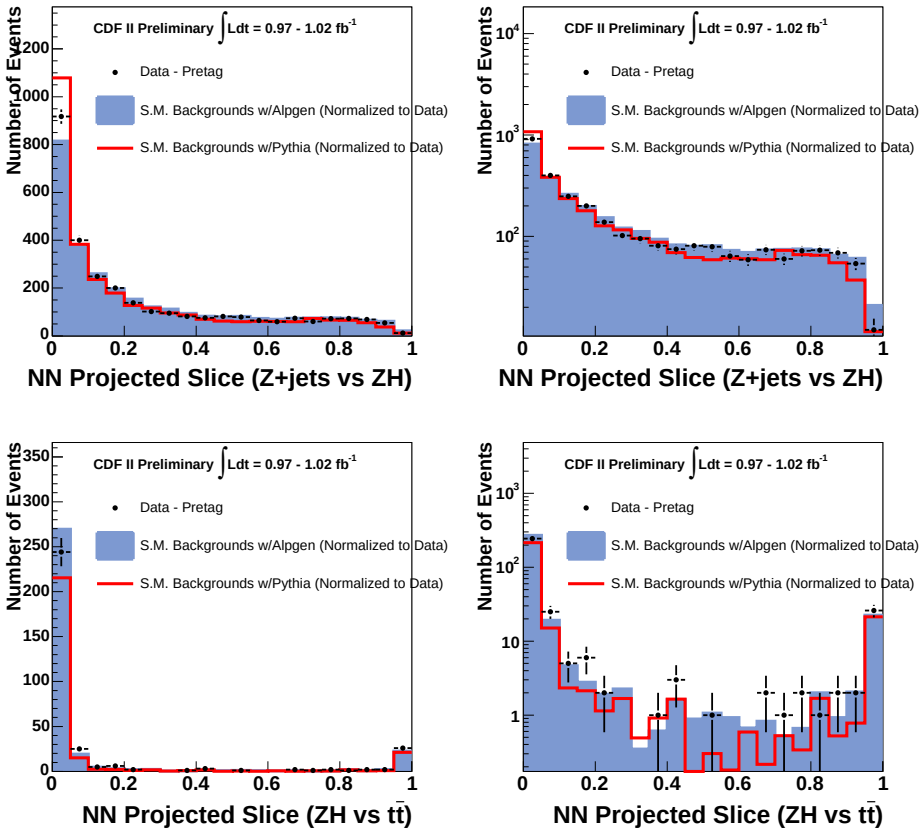

Figure 5.16: Pretagged CANN data compared to Monte Carlo expectations. Shown are the projections of the NN onto the x-axis (upper plots in linear and logarithmic scale) and y-axis (lower plots) after selecting events with $x_{NN} > 0.75$ (top plots) and $y_{NN} < 0.25$ (bottom plots). The Monte Carlo which uses the Alpgen+Herwig Monte Carlo simulations are in blue, Pythia is represented with the red line.

CHAPTER 6

SYSTEMATIC ERRORS

When searching for a small signal in a large background, a systematic error can weaken the strength of the search. Therefore, it is vital to account for these uncertainties and attempt to minimize their impact. In this chapter, I detail the systematic errors taken into account for this analysis. Two types of uncertainties affect the search. The first type impacts the number of predicted events, and is called a normalization uncertainty. The second type impacts the shape of kinematic distributions.

6.1 Normalization Uncertainties

The number of expected signal events presented in Chapter 4 was based on previous measurements and theoretical observations as well as measurements of the efficiency of the CDF detector. All of these measurements are subject to uncertainty. Errors in the assumed cross section are handled in our fitter on a case-by-case basis. However the errors found in the CDF detector are correlated amongst all relevant signal and background samples and must be handled carefully.

6.1.1 Correlated Uncertainties

Several of the uncertainties impact the different samples in a correlated fashion. These impact the ZH signal and the backgrounds modeled with Monte Carlo, such as $Z + b\bar{b}$, $Z + c\bar{c}$, $t\bar{t}$, and dibosons.

The B tagging efficiency has the following uncertainties [49, 64, 65]: an 8% uncertainty on the SecVtx tagging efficiency for b jets and a 16% uncertainty on the SecVtx tagging efficiency for c jets. The efficiency of the SecVtx algorithm is measured in a relatively pure sample of B dijets. A requirement was made for one jet to have a SecVtx tag and another jet to have a lepton present as part of the weak decay of a B jet. The efficiency for SecVtx was then measured in the lepton jet. The sources of uncertainty in this measurement are:

- uncertainty in the heavy flavor fraction of the sample,
- mistag uncertainties,
- differences between B hadrons that decay hadronically versus leptonically.
- statistical errors.

For double tagged jets in our search sample, it was assumed that the tagging efficiency errors are correlated, increasing the uncertainty on double tagged B events to 16%.

Another correlated uncertainty is a 6% uncertainty in the integrated luminosity [66]. This affects all the Monte Carlo samples. The systematic error of the luminosity is dominated by the uncertainties of the $p\bar{p}$ cross section, the CLC acceptance, and the non-linearity of the CLC acceptance.

Finally, there are separate 1% uncertainties on the trigger efficiencies and lepton identification efficiencies. They are correlated between the ZH signal, and the $Z+b\bar{b}$, $Z+c\bar{c}$, $t\bar{t}$, ZW and ZZ backgrounds [47].

6.1.2 Z + heavy flavor Normalization

An uncertainty of 40% was assigned to the normalization of the $Z+b\bar{b}$ and $Z+c\bar{c}$ backgrounds due to the uncertainty in the NLO cross section. This uncertainty is based on the error found in a Z + b jet analysis [57]. This analysis determined the cross section of the Z + b jet cross section by selecting events with both a Z and a SecVtx tagged jet. The mass of the secondary vertex derived from SVX tracks was fit with templates for b flavored jets, c flavored jets and light flavored jets. The measured cross section of the Z + b jets had an uncertainty of 33%. This number was rounded up to include other errors, such as parton distribution function (PDF) errors. It should be noted that the published uncertainty is largely statistically based and should be reduced with more data collected at the Tevatron. This is also consistent with the uncertainty on the W+heavy flavor backgrounds in the WH analysis [67].

6.1.3 Other Monte Carlo Normalizations

An uncertainty of 20% was assigned to the $t\bar{t}$ normalization. This uncertainty takes into account the uncertainty of the $t\bar{t}$ cross section and the uncertainty of the top quark mass. The $t\bar{t}$ cross section has been measured to greater precision, but this number reflects the Monte Carlo samples used for this analysis [68, 69].

An uncertainty of 20% was assigned to the ZW and ZZ normalization. This uncertainty includes the cross section uncertainty. The cross sections of the ZW and

ZZ backgrounds have been recently measured [70, 71], but are statistically limited. The theoretical cross section is used instead [72].

The uncertainty from parton distribution functions (PDF) is estimated using signal samples in which the events are weighted according to their probability to occur using different sets of PDF eigenvectors. The systematic uncertainty is computed by considering differences between the CTEQ5L [73] and MREST72[74] PDFs parameterizations, different QCD values, and the sum in quadrature of half the difference between the $\pm 1\sigma$ shift of the 20 CTEQ6M uncertainties.

6.1.4 Mistag background

The uncertainties on the mistags are allowed to vary both in the shape and the number of events expected. There are many components that contribute to these uncertainties. We calculate each individually and use them simultaneously to calculate our total mistag uncertainty. First, a 6.1% (5.2%) uncertainty is given to the normalization of the tight (loose) negative tag prediction. This uncertainty is due to potential biases in the creation of the mistag matrix stemming from the sample used to create the matrix. In addition, there is a statistical uncertainty in the measurement associated with the negative rates for each "bin" in the mistag matrix. These errors differ bin-by-bin and are treated as uncorrelated errors. A final uncertainty is due to the determination of the asymmetry factor between negative tags and mistags. These errors depend on jet E_T. They stem from uncertainties in the fitting to create the asymmetry factors as well as possible sculpting of data in the creation of the asymmetry. A total uncertainty is found to be 17% for the single tag events and 24%

for the double tag events. The normalization and shape of the mistag background is allowed to fluctuate based on the uncertainties.

6.1.5 Fake Lepton background

A 50% uncertainty was assigned to the fake Z background. This error was selected because it covered all discrepancies in the data used to make the fake electron rates in the jet data as seen in Figure 4.6. Although this uncertainty is large, the absolute size of this background is small. Therefore, the final result is not sensitive to this uncertainty.

6.2 Shape Systematics

Shape systematics differ from the systematics discussed above. These systematics change the NN inputs and output the distributions for our signal and background samples. The number of events is constant but the fraction of events in the signal region can increase or decrease.

The jet energy scale (JES) was first discussed in Section 3.3.3. A systematic error is assigned to address the difference between jet modeling in Monte Carlo and data [46]. The error is assessed by fluctuating the error up and down by 1 σ of their systematic errors. For high energy jets with an $E_T > 60\ GeV/c$, the largest contribution to the systematic error is the absolute jet energy scale. This systematic error is limited by the uncertainty of the calorimeter response to charged hadrons. For low E_T jets, the largest systematic error is the out-of-cone energy corrections. This systematic error can be lowered by studying differences in generators and generally improving them. These errors change both the event acceptance and kinematic distributions of the processes simulated with Monte Carlo. Figure 6.1 shows how both the ZH signal

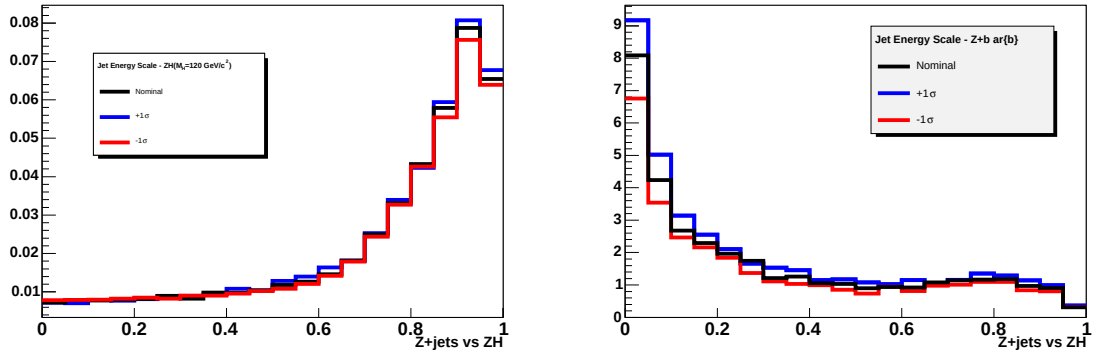

Figure 6.1: The Jet Energy Scale systematic affects on the kinematic shape of the signal (left) and Z+$b\bar{b}$background

and $Z + bb$ respond to changing the JES by 1 σ. All errors are correlated across the different Monte Carlo samples when fitting the data with the systematic errors.

The difference of modeling the $Z+jets$ background using Alpgen versus Pythia was considered. While Alpgen is in good agreement with the data for jet multiplicity, it tends to overestimate the E_T of the jets and several other energy related distributions. Pythia, on the other hand, underestimates the energy of these distributions. This is visible in both the H_T and NN output distribution in the pretag sample shown in Figures 5.8 and 5.15. Since Alpgen does a better job of modeling the NN Output distribution, but the data span the difference between Pythia and Alpgen for the input kinematics, a shape systematic is assigned to account for the difference in generator modeling of the $Z + jets$ background.

For the signal, systematic uncertainties are considered due to initial and final state QCD radiation. The initial and final state radiation systematics are determined by comparing nominal signal Monte Carlo using the "more or less" prescription of Pythia generation parameters [75].

Contribution	Signal	$Z + b\bar{b}$	$Z + c\bar{c}$	mistags	Top	ZZ	ZW	Fakes
Luminosity	6%	6%	6%	0	6%	6%	6%	0
Z+h.f. $\delta\sigma$	0	40%	40%	0	0	0	0	0
Mistags	0	0	0	13% S	0	0	0	0
$t\bar{t}$ $\delta\sigma$	0	0	0	0	20%	0	0	0
Diboson $\delta\sigma$	0	0	0	0	0	20%	20%	0
B-Tag	8%	8%	16%	0	0	8%	16%	0
JES	$^{+2.3\%}_{-2.5\%}$S	$^{+13\%}_{-12\%}$S	$^{+11\%}_{-10\%}$S	0	$^{+1.3\%}_{-2.6\%}$S	$^{+4.1\%}_{-4.4\%}$S	$^{+1.9\%}_{-4.4\%}$S	0
Generator	0	S	S	0	0	0	0	0
Fakes	0	0	0	0	0	0	0	50%
$\mathrm{ISR}^{more}_{less}$	$^{+1.1\%}_{+0.4\%}$S	0	0	0	0	0	0	0
$\mathrm{FSR}^{more}_{less}$	$^{-0.7\%}_{-1.4\%}$S	0	0	0	0	0	0	0
PDF	2%	0	0	0	0	0	0	0
Trigger	1%	1%	1%	0	1%	1%	1%	0
Lepton	1%	1%	1%	0	1%	1%	1%	0

Table 6.1: Systematic uncertainties for single tag channel summary. Listed is the percent errors of each systematic to each sample. Those with shape systematics are listed with an 'S'.

In addition to the overall uncertainty in the number of mistags, there is a shape systematic. Because the weighting of pretagged events grows as a function of their E_T, uncertainties in the mistag matrix could affect the signal region differently than the background region. The new mistag shapes are determined by fluctuating the mistag matrix weights applied to jets systematically up or down by their uncertainty.

6.3 Summary

A list of all the errors considered in this analysis are listed in Table 6.1 for the single tags and Table 6.2 for the double tag channel. Included is the listed percentage change by each systematic error plus an indication of uncertainties that are treated as shape systematics.

Contribution	Signal	$Z + bb$	$Z + c\bar{c}$	mistags	Top	ZZ	ZW	Fakes
Luminosity	6%	6%	6%	0	6%	6%	6%	0
Z+h.f. $\delta\sigma$	0	40%	40%	0	0	0	0	0
Mistags	0	0	0	24% S	0	0	0	0
$t\bar{t}$ $\delta\sigma$	0	0	0	0	20%	0	0	0
Diboson $\delta\sigma$	0	0	0	0	0	20%	20%	0
B-Tag	16%	16%	32%	0	0	16%	32%	0
JES	$^{+0.3\%}_{-1.2\%}$S	$^{+3.1\%}_{-7.8\%}$S	$^{+8.7\%}_{-8.0\%}$S	0	$^{+0.1\%}_{-0.1\%}$S	$^{+0.5\%}_{-3.0\%}$S	$^{+0\%}_{-0\%}$S	0
Generator	0	S	S	0	0	0	0	0
Fakes	0	0	0	0	0	0	0	50%
$\mathrm{ISR}^{more}_{less}$	$^{+4.6\%}_{+0.6\%}$S	0	0	0	0	0	0	0
FSR $^{more}_{less}$	$^{+5.3\%}_{+3.7\%}$S	0	0	0	0	0	0	0
PDF	2%	0	0	0	0	0	0	0
Trigger	1%	1%	1%	0	1%	1%	1%	0
Lepton	1%	1%	1%	0	1%	1%	1%	0

Table 6.2: Systematic uncertainties for double tag channel summary. Listed is the percent errors of each systematic to each sample. Those with shape systematics are listed with an 'S'.

CHAPTER 7

RESULTS

To determine whether there is evidence for signal events in the data, a fit of the 2-D classification NN was performed to a combination of the signal and background templates. Because there is no evidence of a Higgs signal, the fit and associated systematic uncertainties were used to extract a 95% confidence level upper limit on the Standard Model cross section for ZH.

7.1 CANN Output

The NN output of the final data samples is shown in Figure 7.1. The CDF data verifies the expected neural network structure: a peak at $(1,1)$ due mostly to $t\bar{t}$, events at $(0,0)$ mostly due to Z+jets and a region to search for the signal which is expected near $(1,0)$.

The 1-dimensional projections along the x- and y-axes are shown in Figures 7.2 and 7.3 for single tagged and double tagged, respectively. The data agree well with the background predictions. In particular, at the low and high values of the NN output the data confirm the $t\bar{t}$ and $Z+$ jets background estimates.

Also shown in these figures are the NN projections after applying a cut on the other axes, i.e. for the x-axis projection a cut on $y_{NN} < 0.25$ is applied and for

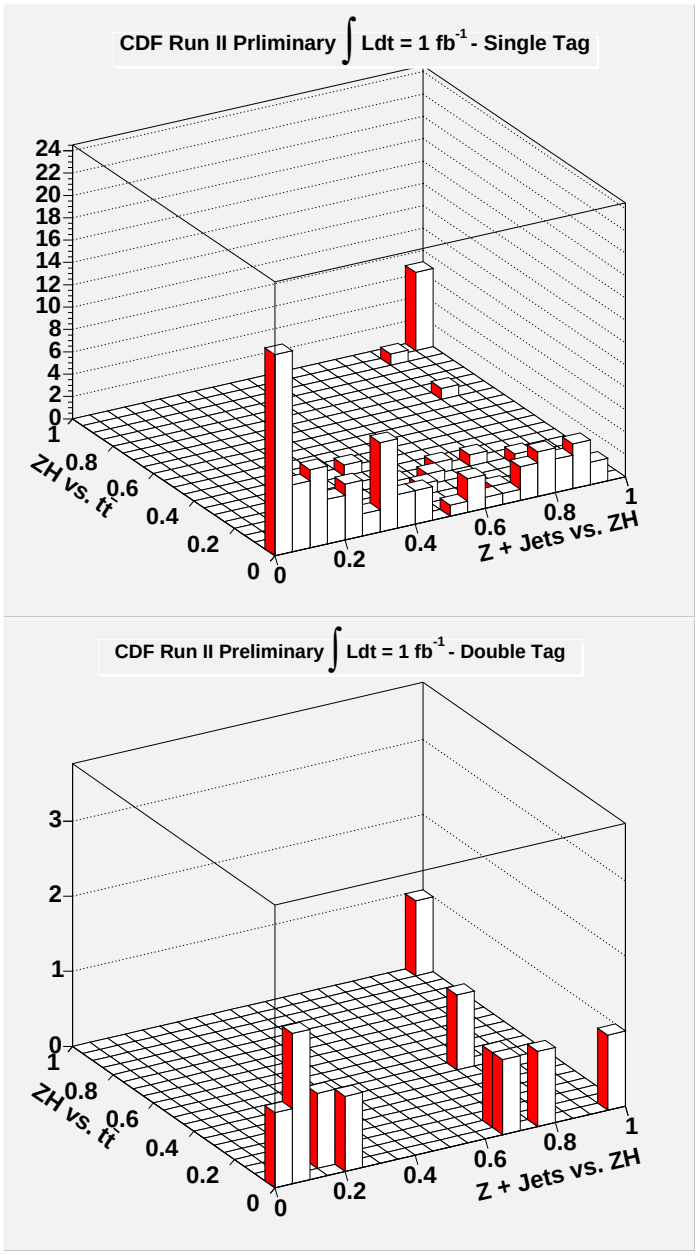

Figure 7.1: The NN output distribution for the electron and muon data combined. Above single tags, below double tags. The $t\bar{t}$ background is expected in the upper right corner, the $Z+$ jets in the lower left and the ZH signal in the lower right.

the y-axis projection a cut on $x_{NN} > 0.75$ is applied to clearly show how the data compare in the region most sensitive to ZH production. Good agreement is observed between the data and the Standard Model prediction.

7.2 Shape Fitting

To search for possible Higgs events, we fitted the entire output of our classification artificial neural network. The program used for this fit is called mcLimit [76]. It functions by making a test statistic, Q, which discriminates a sample with a signal and background from a background only sample. A common test statistic is the likelihood ratio.

To calculate these test statistics, the data are fitted with a background only template and then a signal plus background hypothesis. The shapes that are fit, shown in Figures 5.6 and 5.7, are added together based on the expected contributions. For these fits, we use MINUIT [77] to maximize the Poisson probability of observing the background in the background hypothesis. This procedure takes advantage of the "side bands" of the data, regions with little expected signal, to constrain the number of possible events.

To compute the probability of observing the data for a given channel i, the background in each bin is given by

$$b_{ij}^{b} = \sum_{k=1}^{n_i^{bsources}} F_{ik}^{b} B_{ijk}, \tag{7.1}$$

where $n_i^{bsources}$ is the number of different background sources contributing for channel i, F_{ik}^{b} is the floating scale factor on the k^{th} source of background in channel i, and B_{ijk} is the background shape for the k^{th} background source in bin j of channel i.

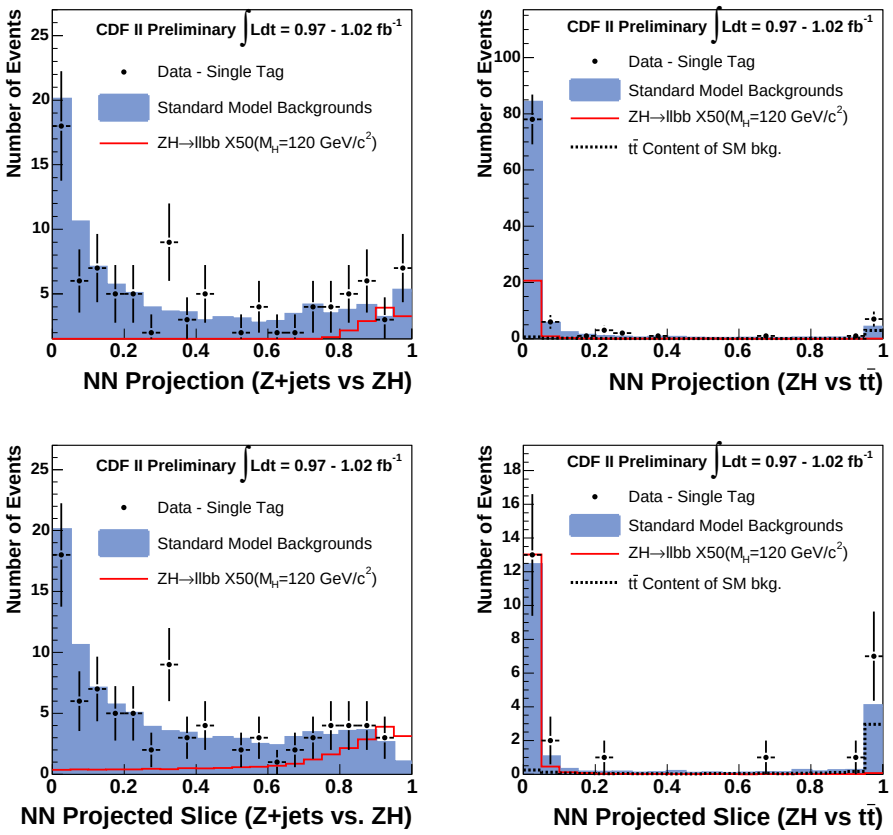

Figure 7.2: Single tagged data compared to Monte Carlo expectations. Shown are the projections of the NN onto the x-axis (upper left) and y-axis (Upper right). Projections of the slice are displayed along the x-axis (bottom left) and y-axis (lower right). The cuts in these plots are $y \leq 0.25$ and $x \geq 0.75$, respectively. The Monte Carlo which uses the Alpgen+Herwig Monte Carlo simulations are in blue, ZH (M_H=120 GeV/c^2) is represented with the red line drawn 50 times the SM expectation.

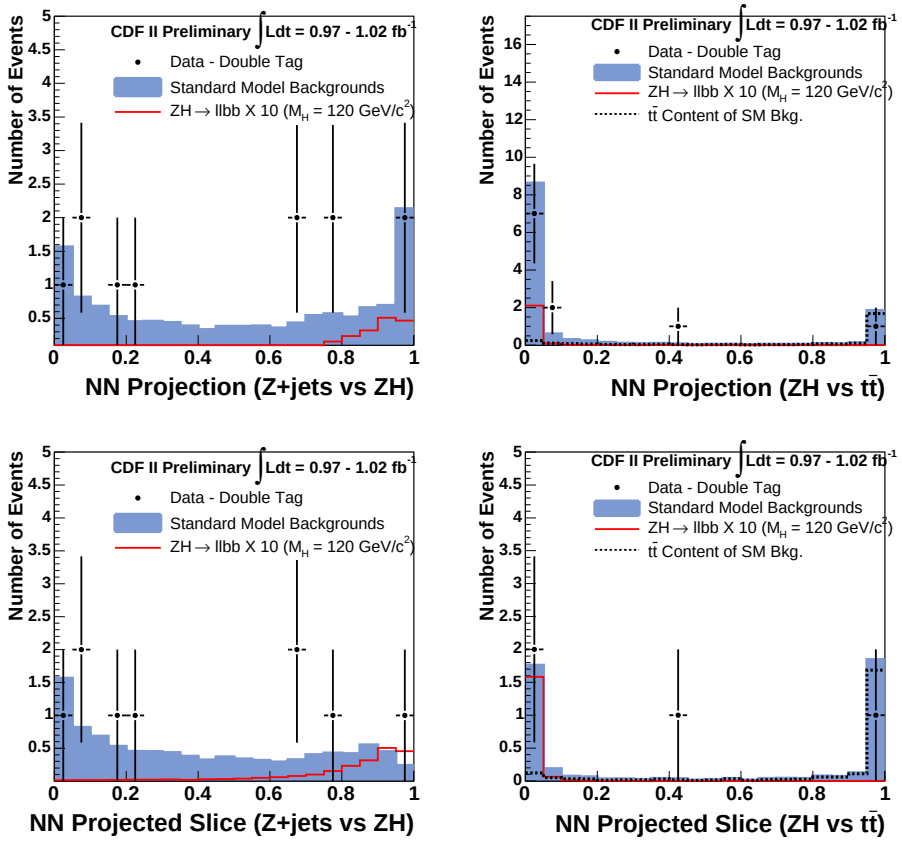

Figure 7.3: Double tagged data compared to Monte Carlo expectations. Shown are the projections of the NN onto the x-axis (upper plots in linear and logarithmic scale) and y-axis (lower plots). Projections of the slice are displayed along the x-axis (bottom left) and y-axis (lower right). The cuts in these plots are $y \leq 0.25$ and $x \geq 0.75$, respectively. The Monte Carlo which uses the Alpgen+Herwig Monte Carlo simulations are in blue ZH (M_H=120 GeV/c^2) is represented with the red line drawn 10 times the SM expectation.

Instead of having freely floating background rates in the fit, the absolute normalization is constrained. The function to be minimized is

$$\mathcal{L}_b = -ln\left[\prod_{j=1}^{n_i^{bins}} \frac{e^{-b_{ij}^b}(b_{ij}^b)^{d_{ij}}}{d_{ij}} \cdot \prod_{k=1}^{n_i^{bsources}} \frac{1}{\sqrt{2\pi\sigma_{ik}}} e^{\frac{-(F_{ik}^b-1)^2}{2\sigma_{ik}^{b\ 2}}}\right] \tag{7.2}$$

where σ_{ik}^b is the uncertainty in the background from source k in channel i and d_{ij} is the observed candidate in channel i. For correlated systematic errors, the scale factors F_{ik}^b are handled together across different backgrounds.

When fitting the background rates in the signal+background hypothesis, the fit function includes the signal rates.

$$\mathcal{L}_{s+b} = -ln\left[\prod_{j=1}^{n_i^{bins}} \frac{e^{-(s_{ij}+b_{ij}^b}(s_{ij}+b_{ij}^s)^{d_{ij}}}{d_{ij}} \cdot \prod_{k=1}^{n_i^{bsources}} \frac{1}{\sqrt{2\pi\sigma_{ik}}} e^{\frac{-(F_{ik}^s-1)^2}{2\sigma_{ik}^{b\ 2}}}\right] \tag{7.3}$$

where

$$b_{ij}^s = \sum_{k=1}^{n_i^{bsources}} F_{ik}^s B_{ijk}, \tag{7.4}$$

gives the background rates in terms of floating parameters in the signal hypothesis.

To set a limit, the log likelihood ratio is formed:

$$Q = \mathcal{L}_{s+b}/\mathcal{L}_b \tag{7.5}$$

This test statistic is then compared to many pseudo-experiments of the data templates. The confidence level of excluding the signal and background hypothesis is defined as

$$CL_{s+b} = P_{s+b}(Q \leq Q_{obs}) \tag{7.6}$$

where P_{s+b} is the probability of finding a pseudo-experiment with a value of Q less than Q observed. In high energy experimental physics, the common value cited is 5% (95% exclusion).

Mass	1-tag Limit		2-tag Limit		Combined Limit	
(GeV/c^2)	Observed	Expected	Observed	Expected	Observed	Expected
100	3.2 pb	3.2 pb	2.1 pb	2.3 pb	1.7 pb	1.8 pb
110	2.3 pb	2.2 pb	1.8 pb	1.8 pb	1.3 pb	1.3 pb
115	2.2 pb	2.2 pb	1.8 pb	1.8 pb	1.3 pb	1.3 pb
120	1.8 pb	1.9 pb	1.7 pb	1.6 pb	1.1 pb	1.1 pb
130	1.8 pb	1.8 pb	1.6 pb	1.5 pb	1.1 pb	1.0 pb
140	2.1 pb	1.8 pb	1.6 pb	1.4 pb	1.2 pb	1.0 pb
150	1.9 pb	1.9 pb	1.6 pb	1.5 pb	1.2 pb	1.0 pb

Table 7.1: Expected and observed limits for $\sigma(ZH) \cdot BR(H \to b\bar{b})$(95% CL). Single-tag and double-tag samples are shown separate and combined.

7.3 Limit on Higgs Production

After fitting the data against the templates, with full systematics, a limit on $\sigma(ZH) \cdot BR(H \to b\bar{b})$ was obtained. Including the systematic uncertainties made the limit 14% worse. The most significant systematic was the b-tagging efficiency which taken by itself made the limit 12% worse.

For a Higgs boson of 115 GeV/c^2 the expected limit was 1.3 pb and the observed limit was 1.3 pb. This limit is 16 times the SM cross section. The final expected and observed limits are shown in Table 7.1 as $\sigma(ZH) \cdot BR(H \to b\bar{b})$. Figure 7.4 shows the limits as a ratio to the SM expected cross section.

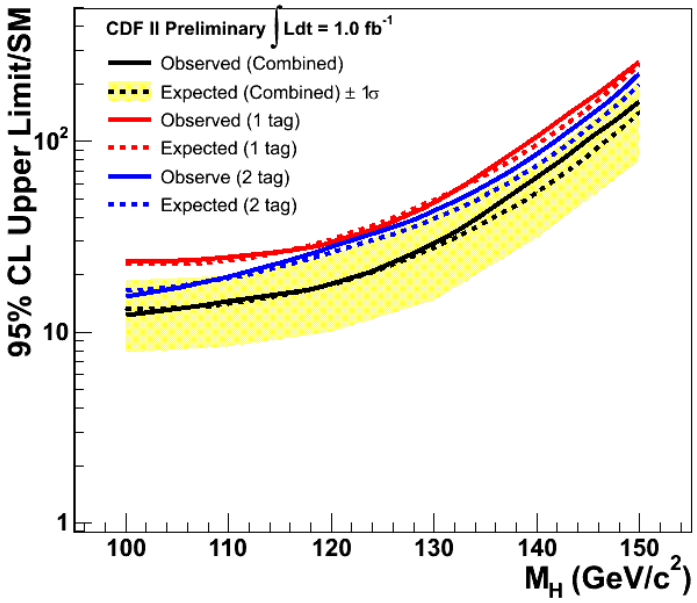

Figure 7.4: Expected and observed limits from the data as a ratio compared to expected Standard Model cross sections (95% CL XSec / SM). Single-tag and double-tag samples are shown separate and combined.

7.4 Description of the most Higgs-like Event

In the double tagged channel, one event is observed in the corner of the Higgs region. It is a dimuon event with a Z mass of 97 GeV/c^2. The dijet mass of the object is 120 GeV/c^2. It has a CANN value of 0.96 in the ZH vs. Z+jets axis and 0.005 in the ZH vs $t\bar{t}$ axis. Displays of the event can be seen in Figure 7.5. The calculated signal to background of this bin of the classification artificial neural network is 1/4.2. The total expected background in this bin is 0.18 events. The SM signal expectation is 0.042 events. The largest background in this one bin is $Z + b\bar{b}$ with 0.11 expected events. The other backgrounds for this bin are 0.019 $t\bar{t}$ events, 0.017 $Z + c\bar{c}$ events, 0.016 ZZ events, and 0.010 mistags events.

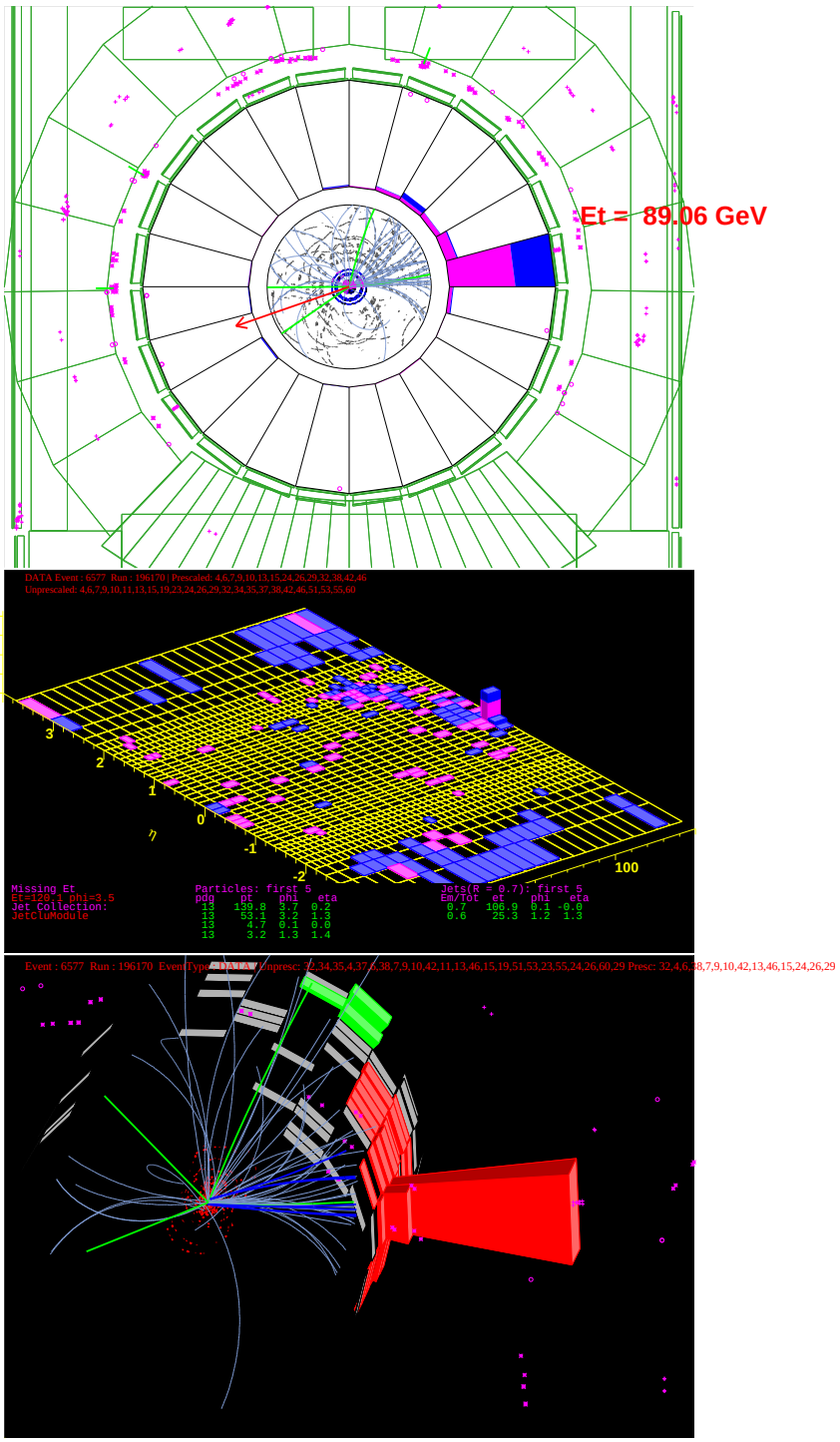

Figure 7.5: Various event displays of event in the Higgs corner in the double tagged channel. Higgs corner in the double tagged channel. It is a dimuon event with a Z mass of 97.3 GeV/c^2 and a dijet mass of 120 GeV/c^2.

CHAPTER 8

CONCLUSIONS

I conclude by putting this search within the context of the other Higgs searches at the Tevatron. Included is a discussion on how this analysis can be improved over time, including the effect of additional data.

8.1 Combination with Other Tevatron Higgs Searches

To strengthen the search capability for the discovery of the Higgs at the Tevatron, great care is taken to combine results across various channels. Results for CDF Run II have been published in the $WH \to \ell\nu b\overline{b}$ [67] and the $H \to W^+W^- \to \ell^+\nu\ell^-\nu$ [78] channels. In addition, results have been presented and publications are in preparation for $ZH \to \nu\nu b\overline{b}$ [79] and for this analysis [80]. All the analyses can be combined to search for the Higgs simultaneously using the technique described in Section 7.2. In places where the systematic errors are the same or similar, such as the b-tagging efficiency and the Z + heavy flavor cross section, the errors are correlated. At a Higgs mass of 115 GeV/c^2, the expected 95% CL upper limit is 8 times the SM expectation. The observed limit is 11 times the SM expectation. This analysis, despite having the least number of events produced (see Figure 2.10) has a similar level of sensitivity as

other analyses. Figure 8.1 shows the expected and observed limits for all the 1 fb^{-1} SM Higgs searches. It also shows the combined limit of all CDF searches.

This combination can be taken a step further and all Tevatron searches can be done simultaneously. DØ has published results for the $ZH \to \nu\nu b\overline{b}$ [81], $H \to W^+W^- \to \ell^+\nu\ell^-\nu$ [82], and $WH \to \ell\nu b\overline{b}$ [83] channels and their $ZH \to \ell^+\ell^- b\overline{b}$ result has been accepted for publication [84]. All results were combined in the summer of 2007[85]. The Tevatron observed limit is 7.8 times the SM for a 115 GeV/c^2 Higgs mass. The expected limit was 4.3 times the SM. It should also be noted that for a Higgs mass of 160 GeV/c^2, the observed limit is 1.4 times the SM. The expected limit for this mass was 2.5 times the SM. The Tevatron results are summarized in Figure 8.2

8.2 Outlook for Full Tevatron Run

This analysis will continue with a larger dataset and with improvements to the technique. With more data, a more sensitive search can be made as shown in Table 8.1. If we presume that CDF can collect the full 8 fb^{-1} of data that is expected, the limit on a Higgs boson with a mass of 120 GeV/c^2 should be reduced from 18 to 5.2 times the Standard Model.

Further improvements can make this analysis even more sensitive to a Higgs discovery. With more data it can be presumed that the systematic errors that are derived from statistical uncertainties in other measurements should be reduced. Prime examples of these are the B tagging efficiency and the Z + heavy flavor cross section.

Also, a wider net can be cast in collecting more Higgs boson events. This can include using different triggers to compliment the current triggers. Examples include a trigger for electrons that do not include a XFT track, but instead searches for two

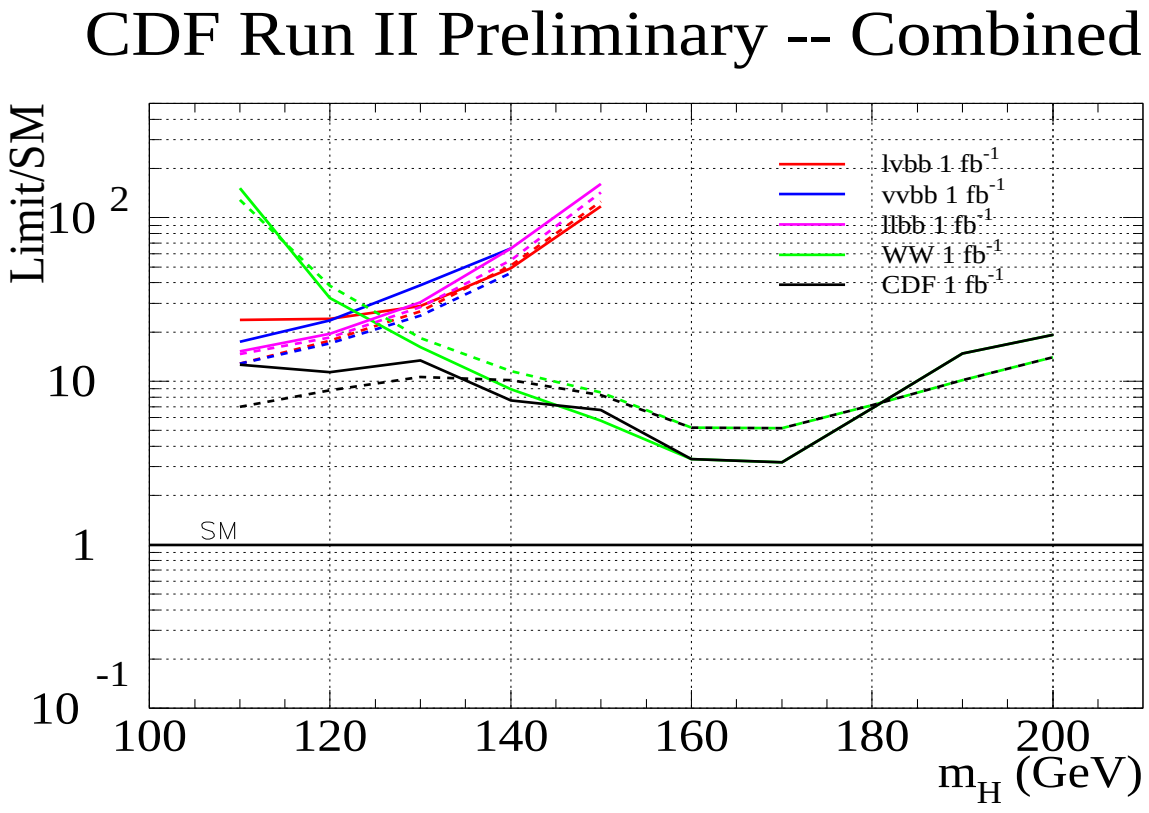

Figure 8.1: The combination of all CDF Higgs searches showing the expected and observed 95% CL limit/SM.

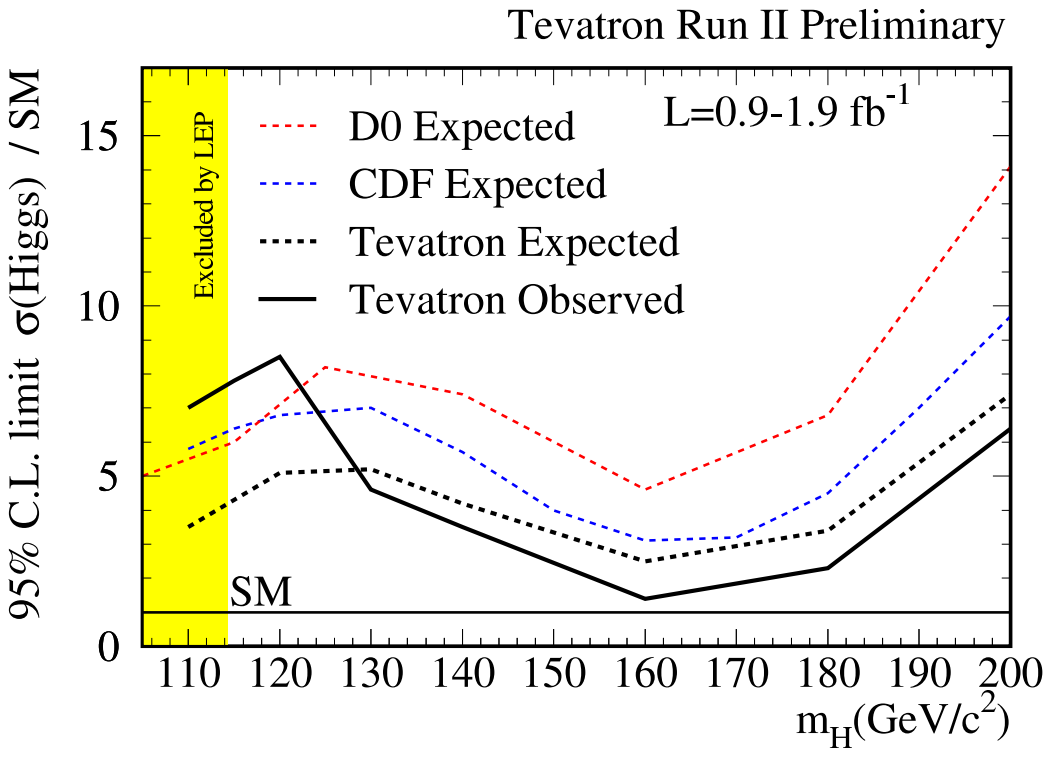

Figure 8.2: The combined limit for all the Tevatron results with 0.9-1.9 fb^{-1}.

Integrated Luminosity ($fb^{-}1$)	Expected Limit (95% CL/SM)
1	18
1.5	14
2	11.8
3	9.0
4	7.6
5	6.0
8	5.2

Table 8.1: How the expected limit is reduced with more luminosity added to the data set. This assumes no improvements in the search, such as better signal efficiency or smaller systematic errors.

calorimeter trigger electrons. This would provide an estimated 20% improvement in signal efficiency.

CDF is preparing b-taggers that are more efficient than the SecVtx algorithm. One such tagger uses a neural network to separate B hadrons from C hadrons and other lighter flavor jets. It is estimated that this would improve the "Tight" SecVtx tagger by 20% (relative) while maintaining the same fake rate.

Further techniques to separate signal and backgrounds can be incorporated in this analysis to strengthen the search for the Higgs boson. One example is using a matrix elements analysis [86] as part of the discriminant. This approach has been used to perform very powerful searches in other analyses [87]. These improvements would strengthen the search for $ZH \rightarrow \ell^+\ell^- b\bar{b}$. Other Higgs analyses can perform similar refinements to their searches. With this aggressive program, a discovery of the Higgs boson at the Tevatron is still a possibility.

APPENDIX A

CLASSIFICATION ARTIFICIAL NEURAL NETWORK CORRELATIONS

One of the strengths of an artificial neural network is that it can exploit correlations between inputs that are not obvious. The following defines an event-by-event correlation between two generic variables x and y:

$$corr(x, y) = \frac{(x - \overline{x}) \cdot (y - \overline{y})}{(\Delta x \cdot \Delta y)^{1/2}}, \tag{A.1}$$

where $\overline{x}$ is the average and $\Delta x = \overline{(x - \overline{x})^2}$ for the distribution in the x variable. For total samples, this number can be averaged to identify patterns in the data. In Table A.1, the correlations of the training signals and backgrounds are shown. In Table A.2 and A.3, the correlations of the input variables to both output dimensions are shown in the same signal and background samples.

A further validation of background modeling can be done by plotting correlation function in data and seeing if they are well modeled by our background. Comparisons between a simulated model and tagged data in the $Z+ \geq 2$ jets events (electrons only) are presented in Figure A.1. The model used is a combination background according to Table 4.12. The most important variables to the neural network, determined through the optimization procedure described in Section 5.3, are H_T, $\not\!\!E_T$, and M_{jj}.

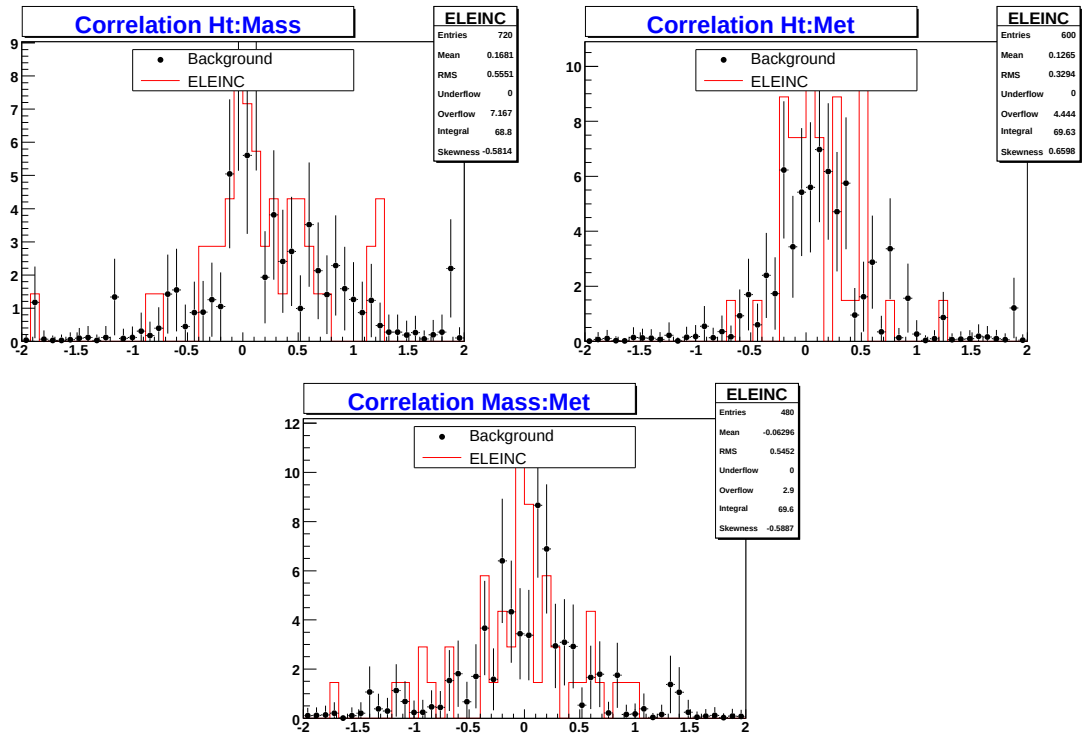

Figure A.1: Distribution of the correlation coefficients in single tight tagged electron data compared to the appropriate mix of background events. Histograms are normalized to equal area.

For a quantitative evaluation of the compatibility between the two shapes, the KS test has been calculated for the 3 distributions shown, with the results of 0.98 for H_T:M_{jj}, 0.76 for H_T:$\not\!\!E_T$, and 0.40 for M_{jj}:$\not\!\!E_T$. There is reasonably good agreement for this subsample of variables.

Correlation	ZH	$t\bar{t}$	$Z + bb$	$Z + c\bar{c}$	ZZ
Mass – Ht	0.236	0.285	0.427	0.421	0.365
Mass – Met	0.0105	0.0154	0.126	0.0507	0.119
Mass – Drj1j2	0.381	0.74	0.707	0.718	0.371
Mass – Drj1Z	-0.0564	-0.235	-0.14	-0.15	-0.0736
Mass – Drj2Z	-0.177	-0.237	-0.298	-0.353	-0.163
Mass – Sph	0.0868	-0.0141	0.0222	0.0348	-0.0134
Mass – Jet2Eta	-0.00735	0.01	-0.00265	-0.0222	-0.0389
Ht – Met	0.082	0.458	0.236	0.223	0.258
Ht – Drj1j2	-0.597	-0.127	-0.0988	-0.0952	-0.497
Ht – Drj1Z	0.113	-0.343	-0.0728	-0.0664	-0.053
Ht – Drj2Z	0.178	-0.0724	-0.105	-0.139	0.0601
Ht – Sph	-0.176	-0.148	-0.0571	-0.0624	-0.128
Ht – Jet2Eta	-0.00378	-0.0386	-0.0181	-0.00457	-0.0259
Met – Drj1j2	0.0757	-0.128	0.0457	-0.051	-0.032
Met – Drj1Z	-0.026	-0.16	-0.0378	-0.00493	-0.0829
Met – Drj2Z	-0.07	0.194	-0.0423	0.00167	0.0532
Met – Sph	-0.102	-0.00288	-0.0657	-0.0411	-0.0843
Met – Jet2Eta	0.00413	-0.0241	-0.00626	0.00413	0.0159
Drj1j2 – Drj1Z	-0.073	-0.155	-0.092	-0.107	0.000374
Drj1j2 – Drj2Z	-0.489	-0.265	-0.392	-0.424	-0.33
Drj1j2 – Sph	0.0923	-0.0774	0.0348	0.0873	0.0842
Drj1j2 – Jet2Eta	-0.000673	0.0141	0.00778	-0.0269	0.0137
Drj1Z – Drj2Z	-0.0839	-0.125	0.127	0.165	0.107
Drj1Z – Sph	-0.236	0.0135	-0.29	-0.331	-0.225
Drj1Z – Jet2Eta	0.000466	-0.00422	0.0322	-0.0177	-0.000403
Drj2Z – Sph	0.00832	0.0685	-0.103	-0.148	-0.0762
Drj2Z – Jet2Eta	-0.0122	-0.00566	0.00601	0.0119	-0.0299
Sph – Jet2Eta	0.121	0.243	0.0453	0.0632	0.0262

Table A.1: List of correlations between input variables of the classification artificial neural network for the signal (ZH) and the various backgrounds. ZH ($M_H = 120$ GeV/c^2) is targeted during training of the $CANN$ to corner (1,0). $Z+b\bar{b}$ and $Z+c\bar{c}$ are targeted during training of the $CANN$ to corner (0,0). $t\bar{t}$ is targeted during training of the $CANN$ to corner (1,1). ZZ is also shown for a reference of a background that is similar to ZH.

Input Variable	ZH	$t\bar{t}$	$Z + bb$	$Z + c\bar{c}$	ZZ
Mass	0.529	0.112	0.532	0.571	0.459
Ht	0.437	0.475	0.484	0.505	0.539
Met	-0.0195	0.603	0.167	0.149	0.18
dRj1j2	-0.0706	-0.192	0.273	0.299	-0.137
dRj1Z	-0.217	-0.347	-0.329	-0.326	-0.341
dRj2Z	-0.223	-0.0225	-0.377	-0.375	-0.314
sph	0.201	0.0634	0.188	0.173	0.142
Jet2Eta	-0.000294	0.0331	-0.0355	-0.000194	0.00531

Table A.2: List of correlations between input variables and the discriminant of Z+jets and ZH (x-axis of CANN). The classification artificial neural network for the signal (ZH) and the various backgrounds. ZH ($M_H = 120$ GeV/c^2) is targeted during training of the $CANN$ to corner (1,0). $Z + b\bar{b}$ and $Z + c\bar{c}$ are targeted during training of the $CANN$ to corner (0,0); $t\bar{t}$ is targeted during training of the $CANN$ to corner (1,1). ZZ is also shown for a reference of a background that is similar to ZH.

Input Variable	ZH	$t\bar{t}$	$Z + bb$	$Z + c\bar{c}$	ZZ
Mass	0.275	0.244	0.463	0.468	0.33
Ht	0.0626	0.618	0.303	0.278	0.324
Met	0.589	0.85	0.561	0.47	0.699
dRj1j2	0.114	-0.117	0.234	0.23	0.0177
dRj1Z	-0.196	-0.322	-0.221	-0.219	-0.22
dRj2Z	-0.0184	0.083	-0.108	-0.109	0.03
sph	0.02	-0.0149	0.00215	0.0161	-0.0313
Jet2Eta	-0.00679	-0.0198	-0.00765	-0.000533	0.0197

Table A.3: List of correlations between input variables and the discriminant of $t\bar{t}$ and ZH (y-axis of CANN). The selected artificial neural network for the signal (ZH) and the various backgrounds. ZH ($M_H = 120$ GeV/c^2) is targeted during training of the $CANN$ to corner (1,0). $Z + b\bar{b}$ and $Z + c\bar{c}$ are targeted during training of the $CANN$ to corner (0,0); $t\bar{t}$ is targeted during training of the $CANN$ to corner (1,1). ZZ is also shown for a reference of a background that is similar to ZH.

BIBLIOGRAPHY

[1] I. Newton, *The Principia : Mathematical Principles of Natural Philosophy*. University of California Press, October, 1999.

[2] **Particle Data Group** Collaboration, W. M. Yao *et. al.*, *Review of particle physics*, *J. Phys.* **G33** (2006) 1–1232.

[3] **CDF** Collaboration, F. Abe *et. al.*, *Observation of top quark production in $\bar{p}p$ collisions*, *Phys. Rev. Lett.* **74** (1995) 2626–2631 [hep-ex/9503002].

[4] **D0** Collaboration, S. Abachi *et. al.*, *Observation of the top quark*, *Phys. Rev. Lett.* **74** (1995) 2632–2637 [hep-ex/9503003].

[5] **CDF - Run II** Collaboration, A. Abulencia *et. al.*, *Measurement of the B_s^0 - $\bar{B}_s^0$ oscillation frequency*, *Phys. Rev. Lett.* **97** (2006) 062003 [hep-ex/0606027].

[6] **CDF** Collaboration, A. Abulencia *et. al.*, *Observation of B_s^0 - $\bar{B}_s^0$ oscillations*, *Phys. Rev. Lett.* **97** (2006) 242003 [hep-ex/0609040].

[7] **D0** Collaboration, V. M. Abazov *et. al.*, *First direct two-sided bound on the B_s^0 oscillation frequency*, *Phys. Rev. Lett.* **97** (2006) 021802 [hep-ex/0603029].

[8] S. Weinberg, *A model of leptons*, *Phys. Rev. Lett.* **19** (1967) 1264–1266.

[9] A. Salam, *Elementary Paticle Tehory: Relativistic Groups and Analyticity (Nobel Symposium No. 8)*, p. 367. Almqvist and Wiksell, 1968.

[10] S. L. Glashow, *Partial symmetries of weak interactions*, *Nucl. Phys.* **22** (1961) 579–588.

[11] A. Djouadi, *The anatomy of electro-weak symmetry breaking. I: The Higgs boson in the standard model*, hep-ph/0503172.

[12] **UA1** Collaboration, G. Arnison *et. al.*, *Experimental observation of lepton pairs of invariant mass around 95 GeV/c^2 at the CERN SPS collider*, *Phys. Lett.* **B126** (1983) 398–410.

[13] **UA2** Collaboration, P. Bagnaia *et. al.*, *Evidence for $Z^0 \to e^+e^-$ at the CERN $p\bar{p}$ collider*, *Phys. Lett.* **B129** (1983) 130–140.

[14] **ALEPH** Collaboration, J. Alcaraz *et. al.*, *A combination of preliminary electroweak measurements and constraints on the Standard Model*, `hep-ex/0612034`.

[15] P. J. Sutton, A. D. Martin, R. G. Roberts and W. J. Stirling, *Parton distributions for the pion extracted from Drell-Yan and prompt photon experiments*, *Phys. Rev.* **D45** (1992) 2349–2359.

[16] P. J. Rijken and W. L. van Neerven, *Order alpha-s**2 contributions to the Drell-Yan cross section at fixed target energies*, *Phys. Rev.* **D51** (1995) 44–63 [`hep-ph/9408366`].

[17] R. Hamberg, W. L. van Neerven and T. Matsuura, *A complete calculation of the order alpha-s**2 correction to the Drell-Yan K factor*, *Nucl. Phys.* **B359** (1991) 343–405.

[18] R. V. Harlander and W. B. Kilgore, *Next-to-next-to-leading order Higgs production at hadron colliders*, *Phys. Rev. Lett.* **88** (2002) 201801 [`hep-ph/0201206`].

[19] A. D. Martin, R. G. Roberts, W. J. Stirling and R. S. Thorne, *Uncertainties of predictions from parton distributions. II: Theoretical errors*, *Eur. Phys. J.* **C35** (2004) 325–348 [`hep-ph/0308087`].

[20] J. Han, A. Bodek, W. Sakumoto and Y.Chung, *$d\sigma/dy$ distribution of Drell-Yan dielectron pairs*, . CDF Public Note 8315.

[21] J. Goldstone, A. Salam and S. Weinberg, *Broken symmetries*, *Phys. Rev.* **127** (1962) 965–970.

[22] P. W. Higgs, *Broken symmetries, massless particles and gauge fields*, *Phys. Lett.* **12** (1964) 132–133.

[23] G. S. Guralnik, C. R. Hagen and T. W. B. Kibble, *Global conservation laws and massless particles*, *Phys. Rev. Lett.* **13** (1964) 585–587.

[24] F. Englert and R. Brout, *Broken symmetry and the mass of gauge vector mesons*, *Phys. Rev. Lett.* **13** (1964) 321–322.

[25] T. W. B. Kibble, *Symmetry breaking in non-abelian gauge theories*, *Phys. Rev.* **155** (1967) 1554–1561.

[26] **Higgs Working Group** Collaboration, M. Carena *et. al.*, *Report of the Tevatron Higgs working group*, hep-ph/0010338.

[27] T. Hambye and K. Riesselmann, *Matching conditions and Higgs mass upper bounds revisited*, *Phys. Rev.* **D55** (1997) 7255–7262 [hep-ph/9610272].

[28] P. C. Bhat, H. Prosper and S. S. Snyder, *Top quark physics at the Tevatron*, *Int. J. Mod. Phys.* **A13** (1998) 5113–5218 [hep-ex/9809011].

[29] **LEP Working Group for Higgs boson searches** Collaboration, R. Barate *et. al.*, *Search for the standard model Higgs boson at lep*, *Phys. Lett.* **B565** (2003) 61–75 [hep-ex/0306033].

[30] **CDF and D0 Working Group Members** Collaboration, L. Babukhadia *et. al.*, *Results of the Tevatron Higgs sensitivity study*, . FERMILAB-PUB-03-320-E.

[31] H. P. Nilles, *Supersymmetry, supergravity and particle physics*, *Phys. Rept.* **110** (1984) 1.

[32] H. E. Haber and G. L. Kane, *The search for supersymmetry: Probing physics beyond the standard model*, *Phys. Rept.* **117** (1985) 75–263.

[33] L. Roszkowski, R. R. de Austri and R. Trotta, *On the detectability of the cMSSM light Higgs boson at the Tevatron*, hep-ph/0611173.

[34] J. Foster, K.-i. Okumura and L. Roszkowski, *New constraints on SUSY flavour mixing in light of recent measurements at the Tevatron*, *Phys. Lett.* **B641** (2006) 452–460 [hep-ph/0604121].

[35] **Fermilab Beams Division** Collaboration, *Tevatron Run 2 handbook*, 1998.

[36] **CDF** Collaboration, F. Abe *et. al.*, *The CDF detector: an overview*, *Nucl. Instr. Meth.* **A271** (1988) 387–403.

[37] **CDF** Collaboration, D. Acosta *et. al.*, *Measurement of the j/ψ meson and $b-$hadron production cross sections in $p\bar{p}$ collisions at $\sqrt{s} = 1960$ gev*, *Phys. Rev.* **D71** (2005) 032001 [hep-ex/0412071].

[38] **CDF** Collaboration, A. Sill, *CDF run II silicon tracking projects*, *Nucl. Instrum. Meth.* **A447** (2000) 1–8.

[39] **CDF** Collaboration, A. A. Affolder *et. al.*, *Intermediate silicon layers detector for the CDF experiment*, *Nucl. Instrum. Meth.* **A453** (2000) 84–88.

[40] **CDF** Collaboration, A. A. Affolder *et. al.*, *CDF central outer tracker*, *Nucl. Instrum. Meth.* **A526** (2004) 249–299.

[41] **CDF** Collaboration, L. Balka *et. al.*, *The CDF central electromagnetic calorimeter*, *Nucl. Instrum. Meth.* **A267** (1988) 272.

[42] **CDF** Collaboration, S. Bertolucci *et. al.*, *The CDF central and endwall hadron calorimeter*, *Nucl. Instrum. Meth.* **A267** (1988) 301.

[43] **CDF** Collaboration, M. G. Albrow *et. al.*, *The CDF plug upgrade electromagnetic calorimeter: Test beam results*, *Nucl. Instrum. Meth.* **A480** (2002) 524–546.

[44] E. J. Thomson *et. al.*, *Online track processor for the CDF upgrade*, *IEEE Trans. Nucl. Sci.* **49** (2002) 1063–1070.

[45] **CDF** Collaboration, F. Abe *et. al.*, *The topology of three jet events in $\bar{p}p$ collisions at $\sqrt{s} = 1.8$ TeV*, *Phys. Rev.* **D45** (1992) 1448–1458.

[46] A. Bhatti *et. al.*, *Determination of the jet energy scale at the collider detector at Fermilab*, *Nucl. Instrum. Meth.* **A566** (2006) 375–412 [hep-ex/0510047].

[47] **CDF II** Collaboration, D. Acosta *et. al.*, *First measurements of inclusive W and Z cross sections from run II of the Tevatron collider*, *Phys. Rev. Lett.* **94** (2005) 091803 [hep-ex/0406078].

[48] **CDF** Collaboration, D. Acosta *et. al.*, *Measurement of the $t\bar{t}$ production cross section in $p\bar{p}$ collisions at $\sqrt{s} = 1.96$ tev using dilepton events*, *Phys. Rev. Lett.* **93** (2004) 142001 [hep-ex/0404036].

[49] **CDF** Collaboration, D. Acosta *et. al.*, *Measurement of the $t\bar{t}$ production cross section in $p\bar{p}$ collisions at $\sqrt{s} = 1.96$ TeV using lepton + jets events with secondary vertex b−tagging*, *Phys. Rev.* **D71** (2005) 052003 [hep-ex/0410041].

[50] T. Sjostrand, L. Lonnblad and S. Mrenna, *PYTHIA 6.2: Physics and manual*, hep-ph/0108264.

[51] R. Brun *et. al.*, *Geant steps into the future*, 1994. Prepared for Computing in High-energy Physics (CHEP 94), San Francisco, CA, 21-27 Apr 1994.

[52] A. Djouadi, J. Kalinowski and M. Spira, *Hdecay: A program for Higgs boson decays in the standard model and its supersymmetric extension*, *Comput. Phys. Commun.* **108** (1998) 56–74 [hep-ph/9704448].

[53] T. Han and S. Willenbrock, *QCD correction to the $p\bar{p}\rightarrow$ WH and ZH total cross- sections*, *Phys. Lett.* **B273** (1991) 167–172.

[54] B. Heinemann, *Summary of most commnly used scale factors for the 2006 summer conferences*, . CDF Internal Note 8312.

[55] M. L. Mangano, M. Moretti, F. Piccinini, R. Pittau and A. D. Polosa, *ALPGEN, a generator for hard multiparton processes in hadronic collisions*, *JHEP* **07** (2003) 001 [hep-ph/0206293].

[56] G. Corcella *et. al.*, *HERWIG 6.5 release note*, hep-ph/0210213.

[57] **CDF** Collaboration, A. Abulencia *et. al.*, *Measurement of the b jet cross section in events with a Z boson in $p\bar{p}$ collisions at $\sqrt{s}$ = 1.96-TeV*, *Phys. Rev.* **D74** (2006) 032008 [hep-ex/0605099].

[58] E. R. Kandel, J. Schwartz and T. M. Jessell, *Principles of Neural Science*. Mc Graw Hill, 2000.

[59] T. H. Abraham, *(physio)logical circuits: The intellectual origins of the mcculloch-pitts neural networks*, *Journal of the History of the Behavioral Sciences* **38** (2002), no. 1 3–25.

[60] G. Cybenko, *Approximation by superpositions of a sigmoidal function*, tech. rep., inst-tufts-cs, October, 1988.

[61] **CDF** Collaboration, D. Acosta *et. al.*, *Measurement of the cross section for $t\bar{t}$ production in $p\bar{p}$ collisions using the kinematics of lepton + jets events*, *Phys. Rev.* **D72** (2005) 052003 [hep-ex/0504053].

[62] J. Schwindling, *MLPfit: A tool for designing and using multi-layer perceptrons*, .

[63] C. Peterson, T. Rognvaldsson and L. Lonnblad, *JETNET 3.0: A versatile artificial neural network package*, *Comput. Phys. Commun.* **81** (1994) 185–220. We use a ROOT-based version of JETNET called Root_Jetnet which can be found online.

[64] S. R. Andrew Foland, Jao Guimaraes da Costa, *Secvtx tag rate matrix for 5.3.3nt*, . CDF Public Note 7326.

[65] **CDF** Collaboration, C. Neu, *CDF b-tagging: Measuring efficiency and false positive rate*, . Presented at TOP 2006: International Workshop on Top Quark Physics, Coimbra, Portugal, 12-15 Jan 2006.

[66] D. Acosta *et. al.*, *The performance of the CDF luminosity monitor*, *Nucl. Instrum. Meth.* **A494** (2002) 57–62.

[67] **CDF** Collaboration, A. Abulencia *et. al.*, *Search for h to b anti-b produced in association with w bosons in $p\bar{p}$ collisions at $\sqrt{s}$ = 1.96-TeV*, *Phys. Rev. Lett.* **96** (2006) 081803 [hep-ex/0512051].

[68] N. Kidonakis and R. Vogt, *Next-to-next-to-leading order soft-gluon corrections in top quark hadroproduction*, *Phys. Rev.* **D68** (2003) 114014 [hep-ph/0308222].

[69] M. Cacciari, S. Frixione, M. L. Mangano, P. Nason and G. Ridolfi, *The t anti-t cross-section at 1.8-TeV and 1.96-TeV: A study of the systematics due to parton densities and scale dependence*, *JHEP* **04** (2004) 068 [hep-ph/0303085].

[70] **CDF** Collaboration, A. Abulencia *et. al.*, *Observation of WZ production*, *Phys. Rev. Lett.* **98** (2007) 161801 [hep-ex/0702027].

[71] **CDF** Collaboration, *Evidence of zz in $p\bar{p}$ at $\sqrt{s} = 1.96tev$*, . CDF Public Note 8775.

[72] J. M. Campbell and R. K. Ellis, *An update on vector boson pair production at hadron colliders*, *Phys. Rev.* **D60** (1999) 113006 [hep-ph/9905386].

[73] S. Kretzer, H. L. Lai, F. I. Olness and W. K. Tung, *CTEQ6 parton distributions with heavy quark mass effects*, *Phys. Rev.* **D69** (2004) 114005 [hep-ph/0307022].

[74] A. D. Martin, R. G. Roberts, W. J. Stirling and R. S. Thorne, *Parton distributions incorporating QED contributions*, *Eur. Phys. J.* **C39** (2005) 155–161 [hep-ph/0411040].

[75] **CDF** Collaboration, A. Abulencia *et. al.*, *Top quark mass measurement using the template method in the lepton + jets channel at CDF II*, *Phys. Rev.* **D73** (2006) 032003 [hep-ex/0510048].

[76] T. Junk, *Confidence level computation for combining searches with small statistics*, *Nucl. Instrum. Meth.* **A434** (1999) 435–443 [hep-ex/9902006].

[77] F. James and M. Roos, *Minuit: A system for function minimization and analysis of the parameter errors and correlations*, *Comput. Phys. Commun.* **10** (1975) 343–367.

[78] **CDF** Collaboration, A. Abulencia *et. al.*, *Search for a neutral Higgs boson decaying to a W boson pair in $p\bar{p}$ collisions at $\sqrt{s}$ = 1.96 TeV*, *Phys. Rev. Lett.* **97** (2006) 081802 [hep-ex/0605124].

[79] **CDF** Collaboration, B. Kilminster, *Search for low mass Higgs at the Tevatron*, hep-ex/0611001.

[80] **CDF** Collaboration, B. Kilminster, *Standard model Higgs boson searches at the Tevatron*, arXiv:0705.3513 [hep-ex].

[81] **D0** Collaboration, V. Abazov, *Search for the standard model Higgs boson in the $p\bar{p} \to ZH \to \nu\nu b\bar{b}b$ channel*, *Phys. Rev. Lett.* **97** (2006) 161803 [hep-ex/0607022].

[82] **D0** Collaboration, V. M. Abazov *et. al.*, *Search for the Higgs boson in H→ WW* decays in p anti-p collisions at s**(1/2) = 1.96-TeV*, *Phys. Rev. Lett.* **96** (2006) 011801 [hep-ex/0508054].

[83] **D0** Collaboration, V. M. Abazov *et. al.*, *A search for $Wb\bar{b}$ and WH production in $p\bar{p}$ collisions at $\sqrt{s} = 1.96$ TeV*, *Phys. Rev. Lett.* **94** (2005) 091802 [hep-ex/0410062].

[84] **D0** Collaboration, V. M. Abazov *et. al.*, *Search for a Higgs boson produced in association with a Z boson in p anti-p collisions*, arXiv:0704.2000 [hep-ex].

[85] T. working group, C. Collaboration and D. Collaboration, *Combined D0 and CDF upper limits on standard-model Higgs-boson production*, 2006.

[86] K. Kondo, *Dynamical likelihood method for reconstruction of events with missing momentum. 1: Method and toy models*, *J. Phys. Soc. Jap.* **57** (1988) 4126–4140.

[87] **CDF - Run II** Collaboration, A. Abulencia *et. al.*, *Precision measurement of the top quark mass from dilepton events at CDF II*, hep-ex/0612060.